Technische Universität München
Physik Department E21 (Lehrstuhl für Experimentalphysik III)

Spin Transfer Torques and Spin Fluctuations in Helimagnets

Dipl.-Phys. Univ. Florian Jonietz

Vollständiger Abdruck der von der Fakultät für Physik der Technischen Universität München zur Erlangung des akademischen Grades eines

Doktors der Naturwissenschaften (Dr. rer. nat.)

genehmigten Dissertation.

Vorsitzender: Univ.-Prof. Dr. Harald Friedrich

Prüfer der Dissertation: 1. Univ.-Prof. Dr. Peter Böni
2. Univ.-Prof. Dr. Rudolf Gross

Die Dissertation wurde am 16.11.2011 an der Technischen Universität München eingereicht und durch die Fakultät für Physik am 08.03.2012 angenommen.

Abstract

This work treats two different aspects of the cubic helimagnets MnSi and $\mathrm{Mn}_{1-x}\mathrm{Fe}_x\mathrm{Si}$. In the first part of this thesis, spin transfer torque effects in MnSi are examined. In the second part, the spin fluctuations in pure MnSi and in $\mathrm{Mn}_{1-x}\mathrm{Fe}_x\mathrm{Si}$ are studied.

Spin transfer torque effects are interesting for applications in the area of spintronics, which is a further development of common electronics, where in addition to the charge, the spin degree of freedom of the electron is utilized. The spin transfer torque is exerted between the spin of the conduction electron and the magnetic structure passed by the electric current. In this way, a magnetic structure can be directly influenced by an electric current, which could pave the way for novel magnetic storage systems. Typically, spin transfer torque effects are examined in ferromagnetic thin film systems, in which, e.g., the ferromagnetic domain walls (Bloch walls) can be displaced by current. So far, current densities larger than $10^{11}\,\mathrm{Am}^{-2}$ had to be applied for measurable spin transfer torque effects, which constitutes a considerable obstacle for practical applications.

In this thesis, the influence of an unpolarized electric current on the helimagnetic structure of MnSi was examined. Preliminary theoretical work indicated that in helimagnetic structures already much smaller current densities could be sufficient for measurable spin transfer torque effects.

The experimental method used for examining the magnetic structure was magnetic small angle neutron scattering, which allows for analyzing the microscopic nature of a structure. In the course of these measurements, an important new aspect of the magnetic phase diagram of MnSi was discovered. By the observation of a hexagonal scattering pattern, an already known magnetic phase (called the A-phase) near the magnetic transition temperature was identified as a so-called skyrmion lattice [1]. Such a lattice had been proposed as a possible magnetic structure in preliminary theoretical studies [2] [3] inspired by experimental works on the pressure dependence of MnSi. But for the A-phase of MnSi, a skyrmion lattice was not predicted. It could be shown that this skyrmion phase is stabilized by thermal fluctuations [1]. The hexagonal alignment of the magnetic vortices the skyrmion lattice is composed of is reminiscent of the vortices in type II superconductors (Shubnikov phase). Only in this skyrmion phase were current-induced effects measured. If a current flows through the sample in the presence of a temperature gradient, a rotation of the hexagonal scattering patterns could be observed. The rotational sense is dependent on the direction of the current, the direction of the applied magnetic field, and the direction of the temperature gradient. We were able to explain this rotational behavior by a very efficient coupling of the spin current to the magnetic vortices and a varying magnetization within the sample, caused by the temperature gradient [4].

The current densities necessary to observe this effect were 5 to 6 orders of magnitude smaller than the current densities typically applied in studies of spin transfer torque effects. This thesis could thus make a contribution to the development of practical applications of the spin transfer torque effect.

The second part of this thesis treats the spin fluctuations in helimagnets. As pointed

out above, fluctuations can explain the stabilization of the skyrmion phase in MnSi [1]. The experimental method used was inelastic neutron scattering on a triple axis spectrometer. The quasi-elastic scattering, which is a Lorentzian function in energy centered at $E = 0$ convoluted with the instrument resolution, was analyzed

Pure MnSi was examined because data on this material was already existent [5] [6] [7] [8] [9]. It had been possible to interpret this data in the framework of the self-consistent renormalization theory developed by Moriya and Kawabata [5] [6]. The primary goal of our measurements was to confirm the previous experimental works and to demonstrate that our measurement method agrees with these works. We were able to confirm the consistence of our data with the previous measurements. However, we also found discrepancies of the data to the theory, which treats the material as an isotropic itinerant ferromagnet. This is a strong indication that a new theory is needed in order to account for the chiral interactions in the helimagnet MnSi.

Next, the spin fluctuations in $Mn_{1-x}Fe_xSi$ with a Fe concentration of $x = 0.12$ were examined in the same way. For this material, only few data existed prior to our experiments [9]. $Mn_{1-x}Fe_xSi$ has attracted interest because it is suspected to have a quantum critical point at a Fe concentration of $x = 0.2$ (i.e. not far from the Fe concentration of our sample). Moreover, with increasing Fe concentration an intermediate regime already existent in pure MnSi is enlarged, in which complex spin structures (e.g. skyrmion textures) might play an important role. Our measurements indicate that also for $Mn_{1-x}Fe_xSi$ a new theory has to be developed in which the chiral interactions have to be taken into consideration.

Contents

Chapter 1

State of the art and motivation

The experiments presented in this PhD thesis were carried out on pure MnSi and on $\text{Mn}_{1-x}\text{Fe}_x\text{Si}$ (doping of MnSi with Fe). Two different aspects of these helimagnets were examined. One part was measuring spin transfer torque effects in pure MnSi and the other part was measuring spin fluctuations in pure MnSi and in $\text{Mn}_{1-x}\text{Fe}_x\text{Si}$. In this chapter, we will give an introduction to these materials and a motivation for our experiments.

1.1 The helimagnet MnSi

MnSi is an itinerant weak magnetic 3d transition metal compound with the cubic B20 structure (space group $P2_13$) [10] [11]. The lattice constant is $a = 4.558\,\text{Å}$. The magnetic properties of MnSi are the result of three hierarchical interactions [12] [13] [14] [15].

- Ferromagnetic interaction [16] [17] [18] [15] favors the parallel orientation of the magnetic moments beneath the magnetic ordering temperature $T_c = 29.5\,\text{K}$. The spontaneous magnetic moment per Mn atom in the ferromagnetic phase is $\mu_s = 0.4\,\mu_B$. The ferromagnetic interaction is the strongest interaction on the energy scale.

- The missing inversion symmetry of the B20 structure results in the so-called Dzyaloshinsky Moriya interaction [19] [20]. This interaction is caused by the dominant spin orbit coupling in the case of missing inversion symmetry. It favors an orthogonal alignment between the magnetic moments. Together with the stronger ferromagnetic coupling, this results in MnSi in a helical magnetic order [21] [22] with the periodicity length $\lambda_H = 180\,\text{Å}$ [23] [24] (see figure 1.1). The magnetic moments are oriented perpendicular to the propagation direction of the helix. This periodicity length is much larger than the lattice constant, because the Dzyaloshinsky Moriya interaction is much weaker than the ferromagnetic interaction.

- Crystal field interactions represent the weakest energy scale. They lock the

propagation direction of the helix in one of the four crystallographic ⟨111⟩ directions [21], [23] [25] (when there is no external magnetic field).
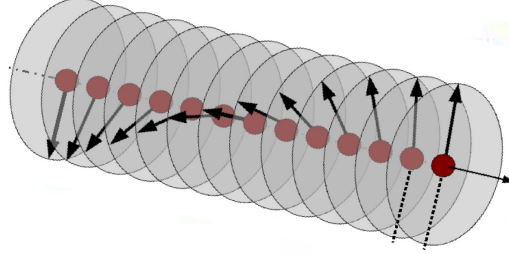
Figure 1.1: Illustration of a helical magnetic structure. The magnetic moments are ordered in the form of a spiral where the moments are oriented perpendicular to the propagation direction.

Figure 1.2 shows the $B-T$ phase diagram of MnSi [14] [26]. The phase boundary at $T_c \approx 29.5 \, \mathrm{K}$ separates the paramagnetic region from the helimagnetic region. In the helically ordered phase, the propagation directions are oriented along the crystalline ⟨111⟩ directions. At $H_{c1} = 0.1 \, \mathrm{T}$, the helical propagation directions reorient into the direction of the applied external magnetic field. With increasing field, the magnetic moments reorient into the field direction [23] [27], until above $\approx 0.6 \, \mathrm{T}$ the magnetic moments are aligned in field direction [14]. This phase of reorienting spins is called the conical phase.

Slightly beneath T_c (at approximately between $27 \, \mathrm{K}$ and $29.5 \, \mathrm{K}$) and between approximately $0.1 \, \mathrm{T}$ and $0.3 \, \mathrm{T}$, the so-called A-phase is encountered [28] [14], where it was originally (before the measurements of this PhD thesis) believed that the helical propagation directions are oriented perpendicular to the direction of the applied magnetic field [29] [30]. But in the course of our experiments, we were able to determine the real nature of this A-phase, which is in fact a complex magnetic vortex structure with a non trivial topology called skyrmion lattice [1]. This structure is described below.
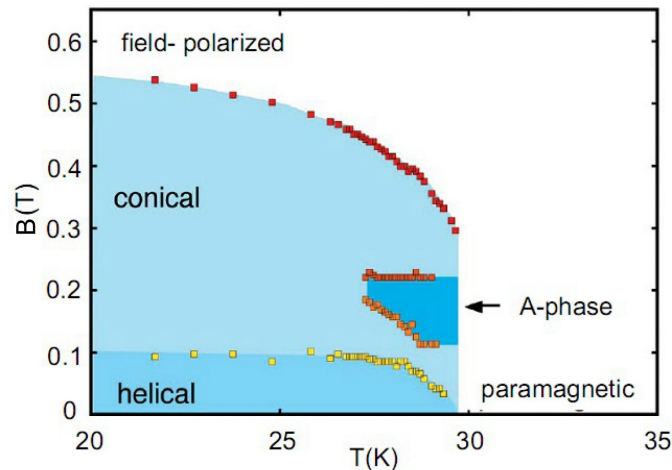
Figure 1.2: Phase diagram of MnSi from [14] with helical phase, conical phase, phase of field induced ferromagnetism (field-polarized), paramagnetic phase and A-phase.

At temperatures above T_c, one observes Curie Weiss behavior of the paramagnetic susceptibility [10]:

$$\chi \propto \frac{\mu_{eff}^2}{T - T_c}, \tag{1.1}$$

where μ_{eff} is the Curie Weiss moment. μ_{eff} is about $2.2\,\mu_B$ for MnSi and therefore it is much bigger than the spontaneous magnetic moment $\mu_s = 0.4\,\mu_B$ in the phase region of the helimagnetic order [18] [15]. The value of μ_s in the helimagnetic state can be determined consistently by neutron scattering, μ-SR and NMR or it can be extrapolated from the magnetization for $H > H_{c2}$ [10].

An intermediate phase at T_c between helimagnetic and paramagnetic phase with a temperature width of less than $1\,\mathrm{K}$ was detected in MnSi. The first observations of this intermediate phase [3] [31] [32] were made by measurements of the specific heat. The existence of this phase in MnSi was also verified in neutron scattering experiments, where at temperatures around T_c scattering patterns in the form of a ring were seen [33] [34] [35] [36] [37], which means that the scattering intensity lies on a sphere in reciprocal space. Currently, it is under debate whether this intermediate phase with the ring shaped diffraction pattern is just due to isotropically distributed helices unpinning from the crystalline directions or whether this is due to some kind of skyrmion phase described below or even to a two-phase region.

1.2 MnSi under pressure and skyrmion stuctures

We briefly introduce the behavior of MnSi under pressure, where MnSi shows non-Fermi liquid behavior and unusual features that could only be described by complex spin structures with non-trivial topology. This gave rise to the theoretical works that finally led to the discovery of skyrmion structures in MnSi [1]. The outline of the following is taken in large parts from [38].

Figure 1.3(i) shows the pressure-temperature phase diagram of MnSi. The pressure is hydrostatic. The transition temperature T_c that separates the helimagnetic phase from the paramagnetic phase was determined by measurements of the susceptibility and the resistivity. It decreases at first linearly as a function of the pressure. At a critical pressure of $p_c = 14.6\,\mathrm{kbar}$, the transition temperature is completely suppressed ($T_c = 0$). But already above a pressure $p^* \approx 12\,\mathrm{kbar}$, the phase transition changes from a second order transition to a first order transition. The phase area where this first order transition occurs is distinguished from the "normal" helimagnetic phase (shown in light blue) by a darker blue. Most recent studies of the susceptibility even suggest that under ambient pressure the phase transition is of weak first order [39].

Below p_c, the measurements of the resistivity are consistent with the behavior of a Fermi liquid (FL). Above p_c and beneath a temperature of $T \approx 12\,\mathrm{K}$, non-Fermi liquid behavior is observed in a broad range of temperature, pressure and magnetic field. The temperature dependence of the resistivity does not show the behavior typical for Fermi liquids, which would be an increase with T^2. Instead, the temperature dependence is proportional to $T^{3/2}$. This non-Fermi liquid behavior is not

expected at a quantum phase transition of first order [40] [32]. In figure 1.3(i), the phase region with non-Fermi liquid behavior (NFL) is shown in green.

In figure 1.3(i), we see in the green non-Fermi liquid phase area at low temperatures a region colored in dark green. Together with the dark blue area above p^*, this is a phase region where partial magnetic order (PO) was observed in neutron scattering by the observation of new scattering patterns [41]. The sharp diffraction peaks in the helimagnetic phase pointing into the crystalline $\langle 111 \rangle$ directions can be observed up to p^*. In the newly observed partial ordered phase, the sharp peaks are replaced by very broad scattering maxima in the $\langle 110 \rangle$ directions. The pressure range of this phase is $p^* < p < p_0 \approx 20$ kbar (see the dark colored area in figure 1.3(i)). Figure 1.3(ii) shows the intensity distributions in the helical phase (left) and in the partial ordered phase (right) on a sphere in reciprocal space. The latter is reminiscent of the behavior of liquid crystals and therefore it is called partial magnetic order. These diffraction patterns cannot be produced by simple helices pinned into the $\langle 110 \rangle$ directions, because the energy of the crystal field has only a saddle point in those directions. Energy minima are only possible theoretically in the $\langle 111 \rangle$ and the $\langle 100 \rangle$ directions [21].
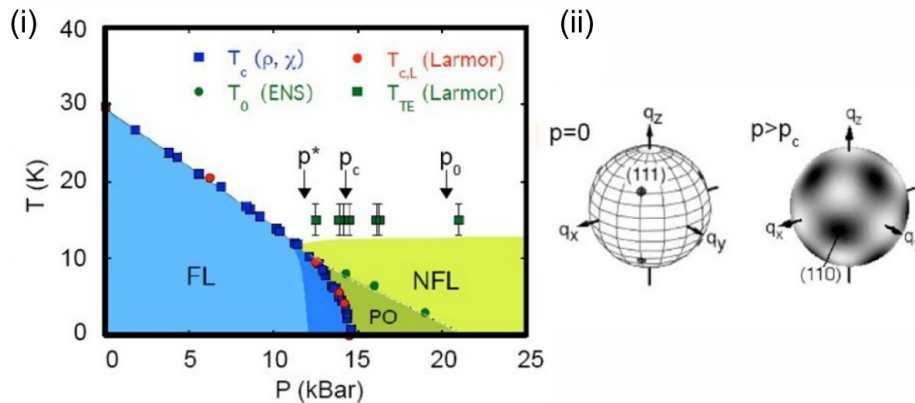
Figure 1.3: (i) Pressure temperature phase diagram of MnSi [13]. The transition temperature T_c drops as a function of pressure. At a critical pressure of $p_c = 14.6$ kbar, the transition temperature is completely suppressed. Below p_c, typical Fermi liquid behavior is observed (FL, in blue color), above p_c, the behavior of a non-Fermi liquid is seen (NFL, in green). In the dark coloured region between a pressure $p^* \approx 12$ kbar and $p_0 \approx 20$ kbar, a partial magnetic order is observed in small angle neutron scattering. (ii) Distribution of the diffraction intensity in the helical phase (left) and in the partial ordered phase (right) displayed on a sphere in reciprocal space. In the helical phase, sharp maxima point into the eight $\langle 111 \rangle$ directions, in the partial ordered phase, broad maxima point into the $\langle 110 \rangle$ directions.

The discovery of the partial magnetic order led to a series of theoretical attempts to explain the unusual scattering patterns with new complex spin structures with non trivial topology. For example, it was tried to explain the partial order as a superposition of spin spirals with different lengths of the spiral modulation [42]. In this model, the spin texture is expected to condense into crystalline structures of spin vortices, resulting, e.g., in a bcc ordered spin crystal, which could explain the observed partial order. A similar approach was to propose spin structures reminiscent

of ordered phases in liquid crystals [43] [44].

Another very important work was done by Rößler *et al.* [3]. They introduced the vortex-like skyrmion structure as a possible candidate for the partial order in MnSi at high pressures and tried to minimize the energy of this structure. The skyrmion structure is a spin crystal where the lattice points consist of the skyrmions, which are cylinder-like objects of spins.

These studies were done before the magnetic skyrmion structure of the A-phase in MnSi was unveiled [1]. They were very important for developing the background for the theoretical works that finally described the skyrmion structure of the A-phase.

1.3 A-phase as a skyrmion lattice

The discovery of hexagonal neutron diffraction patterns in the A-phase of MnSi in the course of our spin torque experiments led to the interpretation of the A-phase as a skyrmion lattice [1]. The diffraction patterns (one is shown in figure 1.4 (ii)) are always oriented perpendicular to the applied magnetic field, independent of crystal orientation.

The hexagonal magnetic structure in the A-phase is described by a triple q structure with q vectors separated by an angle of $120°$, which are oriented perpendicular to the applied external magnetic field. The spin structure is illustrated in figure 1.4 (i). It displays a cut through a plane perpendicular to the applied magnetic field $\mathbf{H}$. Three vectors, $\mathbf{q}_1$, $\mathbf{q}_2$ and $\mathbf{q}_3$, represent the triple q structure perpendicular to the field $\mathbf{H}$. In the direction of the magnetic field, the structure is translation invariant. It is a hexagonal lattice of vortex lines, the so-called skyrmion lattice.

The Ginzburg Landau free energy as a function of the magnetization can be written as (see [1])

$$F[\mathbf{M}] = \int d^3 r (r_0 \mathbf{M}^2 + J(\nabla \mathbf{M})^2 + 2D\mathbf{M} \cdot (\nabla \times \mathbf{M}) + U\mathbf{M}^4 - \mathbf{B} \cdot \mathbf{M}). \qquad (1.2)$$

The quartic term in $\mathbf{M}$ leads to (see [1])

$$\sum_{\mathbf{q}_1, \mathbf{q}_2, \mathbf{q}_3} (\mathbf{M}_f \cdot \mathbf{m}_{\mathbf{q}_1})(\mathbf{m}_{\mathbf{q}_2} \cdot \mathbf{m}_{\mathbf{q}_3}) \delta(\mathbf{q}_1 + \mathbf{q}_2 + \mathbf{q}_3), \qquad (1.3)$$

where $\mathbf{M}_f$ is a uniform component of the magnetization and $\mathbf{m}_\mathbf{q}$ is the Fourier transform of $\mathbf{M}(\mathbf{r})$. This term leads to a local minimum in the free energy when three q vectors add up to zero, like in the skyrmion lattice shown in 1.4. It was found that this energy minimum is only slightly higher than the free energy of the conical structure, making the skyrmion lattice a metastable state. But when small thermal fluctuations beneath T_c were taken into account, it was shown that the skyrmion lattice becomes the ground state (see [1]) .

Already in 1989, such structures were predicted in chiral magnets [2]. But the structure was only predicted to be stable in anisotropic magnetic systems. For cubic

compounds like MnSi, the skyrmion lattice was only predicted as a metastable state.
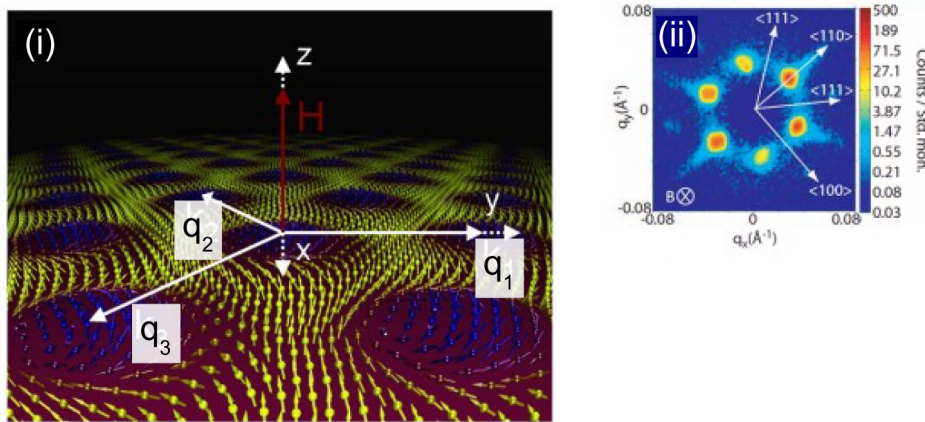
Figure 1.4: (i) Schematic view of the spin texture by a cut perpendicular to the applied magnetic field **H**. The structure can be seen as a superposition of three helices with propagation vectors q_1, q_2 and q_3, which are separated by an angle of 120°. (ii) Resulting hexagonal diffraction pattern of this structure measured in MnSi.

1.4   Doping of MnSi

Substitutional doping in MnSi is the replacement of manganese atoms by neighbouring transition metal atoms. The lattice spacings of $4.48\,\text{Å}$ in FeSi and $4.45\,\text{Å}$ in CoSi are only slightly smaller than in MnSi (where it is $4.58\,\text{Å}$). Therefore, doping with Fe and Co can be interpreted as chemical pressure and, indeed, it has an effect similar to hydrostatic pressure, which was discussed above. For example, the transition temperature is suppressed under doping. However, not only the lattice spacing is changed, but also the electronic structure, like the density of states at the Fermi level.

The two doped MnSi compounds $Mn_{1-x}Fe_xSi$ and $Mn_{1-x}Co_xSi$ had been studied in previous works [45] [46] [47] [38]. Like MnSi, they show helical magnetic ordering. It was known that in $Mn_{1-x}Fe_xSi$ and $Mn_{1-x}Co_xSi$ the transition temperature T_c decreases as a function of the doping concentration x. The bulk properties (specific heat, magnetization, magneto resistance) [47] and also data measured by small angle neutron scattering [38] provide strong evidence of a quantum critical point (where T_c is zero) with $x_c \approx 0.1$ and 0.2 for Co and Fe doping, respectively.

Figure 1.5 presents the magnetic phase diagram for $Mn_{1-x}Fe_xSi$ with a Fe concentration of 4%. The phase diagram was obtained from data taken from bulk measurements (see [47]). Later, neutron scattering measurements confirmed the data [38]. Like in MnSi, a helical phase exists at low fields. The conical phase at higher fields as well as the A-phase is present. The latter shows up like in MnSi as hexagonal diffraction patterns. Furthermore, there is a phase of field-induced ferromagnetism

(FM) above 0.6 T at low temperatures, like in pure MnSi. At higher temperatures, the system is in the paramagnetic phase (PM), like in pure MnSi. The green arrow indicates the transition temperature T_c. Around this transition temperature, a phase which we will call the intermediate phase (IM) shows up, where ring-shaped intensity patterns are observed. It has been said above that in pure MnSi an intermediate phase also exists at ambient pressure around T_c. But it had a temperature range of less than 1 K. Here, in contrast to pure MnSi, the intermediate phase has a large temperature range of nearly 5 K. It was said above that this intermediate phase is suspected to be some sort of skyrmion liquid.

Another difference to pure MnSi is a pronounced hysteresis in $Mn_{1-x}Fe_xSi$ due to the disorder produced by the doping. For example, at a concentration of 4 % Fe, the A-phase shows up as a hexagonal diffraction pattern only if the A-phase is entered after field cooling. When the A-phase is entered zero-field cooled, then the diffraction pattern appears as a homogeneous ring. Generally, the width of the diffraction peaks increases with doping, and finally the diffraction pattern becomes ring-like at high doping [38].
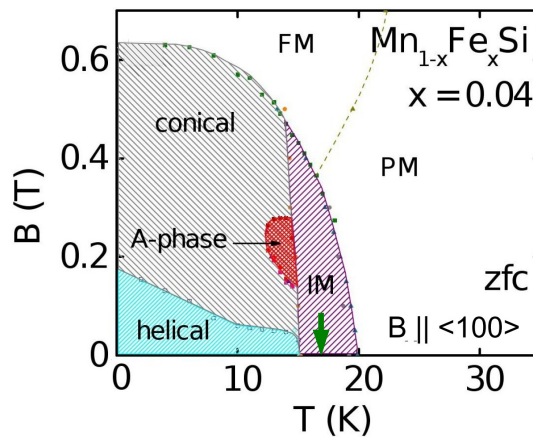
Figure 1.5: Magnetic phase diagram for 4% Fe doping determined from bulk measurements after zero-field cooling (zfc) with magnetic field oriented in $\langle 100 \rangle$ direction [47] [38]. Like in MnSi, a helical phase exists at low fields, a conical phase at higher fields and an A-phase with hexagonal diffraction patterns. At high fields and low temperatures, field-induced ferromagnetism (FM) shows up and at high temperatures paramagnetism (PM). The transition temperature is indicated by a green arrow. Around this transition temperature, there is an intermediate phase (IM), where ring shaped intensity patterns are observed.

The magnetic phase diagram for $x = 0.12$ is presented in figure 1.6. A sample with this Fe concentration was used in this PhD thesis for examining the spin fluctuations. The phase diagram was obtained from the data taken in the bulk measurements [47]. When comparing it to the phase diagram at $x = 0.04$, it is obvious that the transition temperature has been further suppressed by the doping. Still, a helical phase exists at low fields and temperatures below 4 K. Also, the conical phase at higher fields is present. The bulk measurement data suggest the existence of an A-phase, which is extrapolated to $T = 0$ here (shown by the magenta shading). Furthermore, a phase of field-induced ferromagnetism (FM) exists above 0.6 T at low temperatures. The transition temperature is again indicated by a green arrow. Around T_c, an

intermediate phase (IM) is detected. It now dominates the phase diagram. All other aspects are similar to $x = 0.04$.

The diffraction patterns for $x = 0.12$ taken with neutron scattering were ring shaped throughout the whole phase diagram, which means that the scattering intensity lies on a sphere in reciprocal space. No further distinguishing of phases was possible, as the scattering intensity was very weak [38].
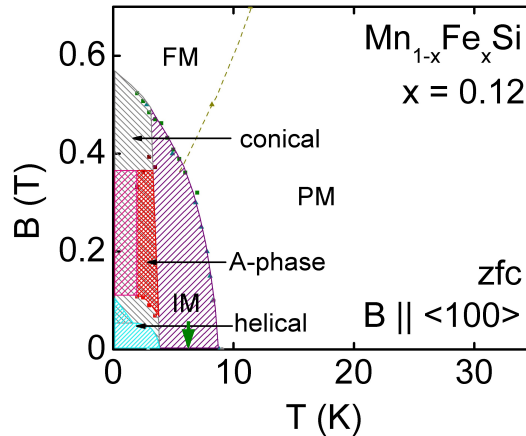
Figure 1.6: Magnetic phase diagram for 12% Fe doping [47] [38] with helical phase at low fields, conical phase at higher fields and A-phase (extrapolated to $T = 0$). At high fields and low temperatures, field-induced ferromagnetism (FM) shows up and at high temperatures, paramagnetism (PM). The transition temperature is indicated by a green arrow. Around this transition temperature, an intermediate phase (IM) is detected, where ring-shaped intensity patterns are observed. The intermediate phase now dominates the phase diagram. The phase diagram was determined from bulk measurements [47] after zero field cooling (zfc) with magnetic field oriented in ⟨100⟩ direction.

It has been demonstrated that the intermediate phase observed in MnSi, where it is very narrow (temperature range of less than $1\,\mathrm{K}$), grows under Fe doping, until it finally dominates the phase diagram at high doping concentrations. This intermediate phase is a strong candidate for a complicated non-trivial topological spin structure (for example, a skyrmion texture) and therefore very interesting. Furthermore, it was mentioned that the data suggest a quantum critical point for a critical Fe concentration of $x_c \approx 20\%$. Thus, the study of spin fluctuations in $\mathrm{Mn}_{1-x}\mathrm{Fe}_x\mathrm{Si}$ with a Fe concentration of 12%, which is quite near the critical concentration x_c, allows us to explore the nature of these fluctuations near quantum criticality in the presence of skyrmion textures. This information will also be essential for an understanding of the non-Fermi liquid phase and the partial order in pure MnSi under pressure. Generally, the linewidth of magnetic fluctuations reveals information on the development and stabilization of the structures.

1.5 Spin transfer torques

A brief introduction to spin transfer torque effects will be given here. It describes on a general level the research conducted in this field and mentions some existent applications and devices that already use spin transfer torque effects. Then, a motivation is given why spin transfer torque effects are interesting in helimagnets, especially in MnSi.

Spintronics is a further development of the electronics used today. In electronics, only the charge of the conduction electron e is used, whereas in spintronics also the spin degree of freedom of the electron is used. Therefore, through the interaction of the conduction electron spin with magnetically ordered structures, new ways of data storage and new logical components might be possible [48] [49] [50].

The possibility of controlling electric current by magnetism has already lead to a number of important applications, for example the GMR effect (giant magneto resistance) (Nobel price 2007 for Peter Grünberg) [51] [52], the TMR-effect (tunnel magneto resistance) [53] and the AMR effect (anisotropic magneto resistivity) [54]. These belong to the group of the magneto resistive effects, sometimes referred to as XMR. In fact, the discovery of the giant magneto resistance effect now used commercially in the hard disk drive industry is widely recognized as the starting point of the field of spintronics. It represents the first example of electric currents controlled efficiently by spin structures.

An interesting question is whether the complementary process of controlling and manipulating magnetic structures and textures by electric currents is feasible [55] [56] [57] [58] [59]. This is currently intensively examined, because in this way important applications in magnetic data storage might become possible [60] [61] [62] [63] [64] [65]. The underlying physical process is the spin transfer torque: the spins of the conduction electrons exert a torque on the magnetic structure of the material, the so-called spin transfer torque. The spins of the conduction electrons are turned into the direction of the magnetic moments of the material. In this process, the spin of the conduction electrons exerts a torque on the magnetic moments of the material. Spin pumping is the reverse process, where the magnetic structure can influence the spin directions of the conduction electrons of an electric current through the material. These processes appear to be even more promising for applications than the already used magneto resistive effects.

Examinations of this spin transfer torque were done on various different material systems. All these systems have a ferromagnetic (or antiferromagnetic) or another magnetically ordered structure, which is influenced by the spins of the conduction electrons of the electric current.

There have been examinations where the magnetization of ferromagnetic thin films is manipulated by electric currents, allowing the switching of magnetic domains in multilayer devices [66] [67]. Here it was achieved in so-called magnetic tunnel junctions (mtj) to imitate a few characteristics of semiconductor diodes [68]. In other experiments on spin transfer torque, strong current pulses allowed the induction of microwave oscillations in nanomagnets [60] or the switching of ferromagnetic

semiconductor structures [69].

Another field of research is the question what influence the current has on magnetic domain walls [70] [71] [72]. The rotation of the magnetic moments caused by spin transfer torque interaction is seen in a displacement of the domain walls. Figure 1.7 shows a ring made of permalloy, in which ferromagnetic ring structures can be created, i.e. the direction of the magnetic moment circulates along the ring. Here, domain walls of different types can be localized at narrow points of the ring (realized by notches). Displacements of the domain walls by spin transfer torque effects can be generated by pulsed currents with current densities of $10^{12}\,\mathrm{A/m^2}$ [73].
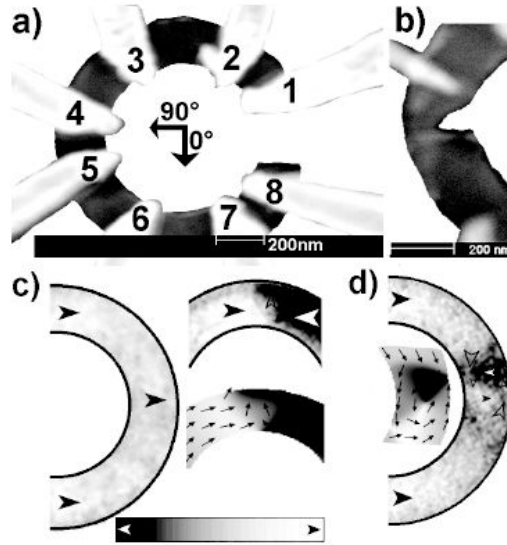
Figure 1.7: Current induced displacement of ferromagnetic domains in ferromagnetic ring structures made of permalloy [73]. (a) Permalloy ring with 8 contacts. The location of the domain wall is determined by the measurement of the magneto resistivity between two contacts. (b) Narrow point (notch) for localizing a domain wall. (c) Transversal domain wall (the gray scale shows the direction of the magnetization). (d) vortex-like domain wall.

As the typical current densities required to create observable spin transfer torques in present-day studies exceed $10^{11}\,\mathrm{Am^{-2}}$, which implies extreme Ohmic heating, it was generally believed that spin transfer torque effects can be studied exclusively in nanostructures.

Another interesting question is how spin transfer torque effects show up in helical magnetic materials like FeGe or MnSi [55]. The helimagnetic structure can be seen as a domain wall (Bloch wall) that is infinitely extended through the whole material (figure 1.1).

The experiments on spin transfer torque in helimagnets in this PhD thesis were inspired by theoretical predictions [74] which indicated the possibility of observing spin transfer torques in such helimagnetic materials at current densities that are orders of magnitude smaller than those used typically in experimental studies on current driven magnetization dynamics in ferromagnetic metals and semiconductors.

When working on my diploma thesis, which I also did in this group [75], first ex-

perimental examinations were made on this subject. The effects of an unpolarized electric current on the magnetic structure of MnSi were examined mainly by measurements of the magnetic susceptibility. We found strong indications that in MnSi spin transfer torque interactions lead to changes in the magnetic structure. The current densities required to observe these changes were a few $10^6 \frac{A}{m^2}$ and thus were about 5-6 orders of magnitude smaller than in comparable examinations in soft ferromagnets [70] [73].

1.6 Spin fluctuations

In weak itinerant ferromagnets (like MnSi), the conduction electrons determine the magnetic properties (itinerant magnetism). Therefore, a band theory must be applied in order to describe the magnetism in these materials. In contrast, in ferromagnets of insulating materials, the localized electrons are best described with the Heisenberg model (local moment magnetism). The outline of the following is taken in large parts from [36]. A band model of itinerant ferromagnetism was developed by Stoner [16], but it was not able to predict the properties at high temperatures (above T_C), e.g., the Curie Weiss (CW) magnetic susceptibility, due to the type of magnetic excitations assumed by this model. The thermal excitations of the Stoner band magnetism are only single electron spin flip excitations (Stoner excitation). Therefore, the magnetic properties at high temperature are not calculated correctly because the model neglects correlations.

Moriya and Kawabata developed a self-consistent renormalization theory (SCR). With this theory, the magnetic properties at high temperatures of the 3d ferromagnetic metals could be better described [15]. MnSi was the first material with weak itinerant ferromagnetism that could be described by the SCR theory. It is therefore a very important material in a historical sense.

The SCR treats the following excitations:

- Stoner excitations, already mentioned above. These are single electron spin flip excitations above the so-called Stoner boundary in the Stoner continuum. The Stoner excitations depend only weakly on temperature [26].

- Spin waves as collective excitations. They have the dispersion $\hbar\omega = Dq^2$. They exist in the field induced ferromagnetic phase below the Stoner boundary E_{SB}. They develop into critical scattering above $T_C \approx 29.5\,\mathrm{K}$ [26] [76] [77].

- Critical scattering in the paramagnetic phase. These are the critical spin fluctuations above T_C that were reinvestigated in this PhD thesis in MnSi and were measured in $Mn_{1-x}Fe_xSi$. The spectral shape of these fluctuations is a Lorentzian in energy centered at $\hbar\omega = 0$, given by the scattering cross section

$$S(\mathbf{q}, \omega) \propto \frac{\Gamma(\mathbf{q})}{(\hbar\omega)^2 + \Gamma(\mathbf{q})^2}.$$

(1.4)

The linewidth $\Gamma(q)$ has a distinct q dependence given by

$$\Gamma(q) \propto \frac{q}{\chi(q)} = \frac{q(\kappa(T)^2 + q^2)}{\chi_0}. \tag{1.5}$$

Here, $\kappa(T)^2 = \kappa_0^2(T - T_C)$ is the inverse magnetic correlation length. χ_0 is the non-interacting susceptibility. The q dependence of the linewidth in this model is different from the one of the Heisenberg model, which has a $q^{2.5}$ dependence.

These excitations were measured in MnSi by inelastic neutron scattering in the field induced ferromagnetic phase ($B > 0.6\,\mathrm{T}$) or in the paramagnetic phase above T_C by Ishikawa *et al.* [26] [5] [6].

But the SCR theory neglects the Dzyaloshinsky Moriya interaction. Therefore, it describes the properties of weak itinerant ferromagnets, but it cannot explain the helimagnetic properties in MnSi. In the helimagnetic regime, the Dzyaloshinsky Moriya interactions become important and must be considered in the calculations. The importance and relevance of the Dzyaloshinsky Moriya interactions was enforced by experiments with polarized neutron scattering that demonstrated that chiral magnetic correlations in the magnetic excitations of MnSi exist. This was seen in the (field-induced) ferromagnetic phase [78]. Additionally, chiral magnetic fluctuations (critical scattering) above T_C were observed [79].

Two theory groups derived the spin wave spectrum in the helical magnetic phase in MnSi (chiral excitations) by including the Dzyaloshinsky Moriya interactions. These excitations are called helimagnons. For details see [80] [81]. The existence of the helimagnons in MnSi was recently experimentally demonstrated by Janoschek *et al.* [36] [82].

A quantitatively very accurate model was developed by Lonzarich and Taillefer [18] [83] for the magnetic equation of state of ferromagnetic or nearly ferromagnetic metals. Additionally to SCR theory, it takes into consideration both longitudinal and transversal low energy spin fluctuations. The model's phenomenological parameters are taken from the neutron scattering experiments done by Ishikawa *et al.* [5] [6]. The dependence of the linewidth on q obtained in this model is similar to the one predicted by SCR theory. They are even identical expressions when the factors are renamed. It is given as

$$\Gamma(q) \propto q(\chi^{-1} + cq^2). \tag{1.6}$$

The parameter c is a phenomenological parameter representing the spin wave stiffness. χ^{-1} is the inverse magnetic susceptibility.

Chapter 2

Experimental methods

This chapter begins with an introduction to neutron scattering. Then, neutron diffraction at a helimagnetic structure will be explained and the neutron diffractometer MIRA will be presented, where we conducted the measurements on spin transfer torque. After that, inelastic neutron scattering on a triple axis spectrometer will be explained, as with this method we measured the spin fluctuations. In the end of this chapter, we will present the detailed experimental set-ups for the measurements on spin transfer torque and for the measurements of the spin fluctuations.

2.1 Introduction to neutron scattering

The most basic concepts of neutron scattering will be introduced; for a detailed introduction see [84], [85], [86], [87] [88] [89] [36].

With neutron scattering, both the static and dynamic microscopic properties of condensed matter systems can be examined. The advantages of neutron scattering versus other methods like for example X-ray scattering and electron scattering, are:

- The wave length of thermal neutrons (de Broglie wave length) is of the same order of magnitude as the lattice spacing of atoms in condensed matter or in liquids. Therefore, the resolution is sufficient to examine these structures.

- Energy and momentum of thermal neutrons are of the same order of magnitude as the elementary excitations in condensed matter. Inelastic neutron scattering is therefore ideally suited for the examination of dispersion relations of phonons and magnons.

- Neutrons do not carry electric charge. Therefore, they can penetrate deeply into the material, making it an important method to examine the entire bulk of the sample and not only the surface (as is done, e.g., with electron scattering).

- Neutrons interact with the nuclei of the sample by the strong interaction.

Because it has a very short range, it can be assumed to be point like. This
leads to a high and $\vec{q}$ independent form factor.

- Neutrons carry a spin, which interacts with magnetic structures of the sample
  via the magnetic dipole-dipole interaction. Hence, the neutrons are scattered
  by magnetic structures of the sample, enabling their examination.

During the scattering process, energy and momentum conservation have to be ful-
filled. This leads to the following relations, where $\vec{k}_i$ is the wave vector of the
incident neutron, $\vec{k}_f$ is the wave vector of the scattered neutron, $\vec{q}$ is the momentum
transferred between sample and neutron and $\hbar\omega$ is the energy transfer, which is the
energy lost or gained by the neutron during the scattering process:

$$\vec{q} = \vec{k}_i - \vec{k}_f \tag{2.1}$$

$$\hbar\omega = E_i - E_f = \frac{\hbar^2}{2m_n}\left(\vec{k}_i^2 - \vec{k}_f^2\right) \tag{2.2}$$

The probability that a neutron is scattered, that the momentum transferred between
sample and neutron is $\vec{q}$, and that the gain (or loss) of the neutron energy is $\hbar\omega$, is
given by the scattering function $S(\vec{q}, \omega)$, which is the Fourier transform of the space
and time dependent scattering potential. The double differential scattering cross
section is defined as:

$$\frac{d^2\sigma}{d\Omega_f dE_f} = \frac{\text{neutrons scattered into angle } d\Omega_f \text{ in the energy interval } dE_f}{\text{incident neutron flux } \Phi d\Omega_f dE_f} \tag{2.3}$$

The scattering cross section of the neutrons is the sum of the coherent and the
incoherent cross sections. The coherent part describes the scattering from collec-
tive phenomena like the periodicity of the nuclear scattering centers (nuclear Bragg
scattering) or scattering at phonons and magnons, which are collective excitations.
In turn, uncorrelated movements of the particles (diffusion, fluctuation, etc.) result
in the incoherent part of the cross section, which is independent of the scattering
vector $\vec{q}$.

While being scattered, a neutron can induce a transition between the quantum states
of the scattering partner. But the quantum states do not get altered. Therefore,
Fermi's golden rule can be applied for the calculation of the scattering cross section.
V is the interaction operator, λ_i is the quantum number of the sample before the
scattering process and λ_f is the quantum number after scattering, m_n is the mass
of the neutron. For the interaction cross section, this leads to

$$\left.\frac{d^2\sigma}{d\Omega_f dE_f}\right|_{\lambda_1 \Rightarrow \lambda_f} = \frac{k_f}{k_i}\left(\frac{m_n}{2\pi\hbar^2}\right)^2 |\langle \mathbf{k}_f\lambda_f|V|\mathbf{k}_i\lambda_i\rangle|^2 \delta(\hbar\omega + E_i - E_f). \tag{2.4}$$

Because the interaction due to the strong interaction between neutron and core is
weak and is of a small range (in the femtometer range) compared to the wave length
of the neutrons (in the range of Å), the scattering process can be described by the
Born Mayer approximation. Hence, the wave function of the neutron before and
after scattering can be described as a plain wave.

2.1.1 Neutron diffraction

For the very short range nuclear interaction potential of a single nuclear scattering center, a delta function can be assumed. This leads to elastic nuclear Bragg scattering

$$\frac{d\sigma}{d\Omega}\bigg|_{el} = N_n \frac{(2\pi)^3}{v_0} \sum_{\tau} \delta(q - \tau) \, |F_n(\tau)|^2 \,, \tag{2.5}$$

where N_n is the total number of the lattice points of the Bravais lattice, τ is a reciprocal lattice vector, v_0 is the volume of the unit cell, and $F_n(\tau)$ is the nuclear structure factor, which accounts for the distribution of atoms within the unit cell. From the cross section, we see that for q values with $\vec{q} = \vec{\tau}$ Bragg maxima will show up.

In magnetic scattering, two aspects are added. On the one hand, the interaction potential is now a dipole-dipole interaction and, hence, direction-dependent, on the other hand, the change of the spin state of the neutron before and after the scattering has to be considered. The neutron interacts with magnetic dipolar moments in the sample because it possesses a magnetic moment

$$\vec{\mu}_n = -\gamma \mu_n \vec{\sigma}, \tag{2.6}$$

where γ is the gyromagnetic ratio, μ_n is the nuclear magneton and $\vec{\sigma}$ is the spin operator. The interaction potential of the magnetic dipolar moment of the neutron with a magnetic field is

$$V_m = -\vec{\mu}_n \vec{B}. \tag{2.7}$$

The magnetic field created by the electrons of the sample consists of two parts, the spin part and the angular momentum part. The spin of one electron is $\vec{s} = \frac{1}{2}\vec{\sigma}$. The electron has a momentum $\vec{p}$. Due to the magnetic dipolar moment of the electron (which resides at the origin)

$$\vec{\mu}_e = -2\mu_B \vec{s}, \tag{2.8}$$

a magnetic field at the position $\vec{R}$

$$\vec{B}_s = \nabla \times \vec{A} \tag{2.9}$$

is produced, where

$$\vec{A} = \frac{\mu_0}{4\pi} \frac{\vec{\mu}_e \times \vec{R}}{R^3}. \tag{2.10}$$

On the other hand, the electron as a moving charge e produces a magnetic field at the position $\vec{R}$

$$\vec{B}_L = -\frac{\mu_0}{4\pi} \frac{2\mu_B}{\hbar} \frac{\vec{p} \times \vec{R}}{R^3}. \tag{2.11}$$

Then, the total magnetic interaction potential between neutron and electron is the sum of spin part and orbital part

$$V_m = -\frac{\mu_0}{4\pi} \gamma \mu_n 2\mu_B \vec{\sigma} (\vec{W}_s + \vec{W}_L), \tag{2.12}$$

with the spin part

$$\vec{W}_s = \nabla \times \left(\frac{\vec{s} \times \vec{R}}{R^3}\right) \tag{2.13}$$

and the orbital part

$$\vec{W}_L = \frac{1}{\hbar} \frac{\vec{p} \times \vec{R}}{R^3}. \tag{2.14}$$

The Fourier transform of this interaction potential

$$\int V_m \exp(i\vec{q}\vec{r}) d^3r \tag{2.15}$$

is a decisive part in the calculation of the interaction cross section. It is proportional to the magnetic interaction vector $\vec{\rho}_\perp$, which is considered as a scattering length. $\vec{M}(\vec{r})$ is the position-dependent magnetization within the sample. The magnetic interaction vector $\vec{\rho}_\perp$ is related with the Fourier transform of the position dependent magnetization within the sample (called the magnetic structure factor)

$$\vec{M}(\vec{q}) = \int \vec{M}(\vec{r}) \exp(i\vec{q}\vec{r}) d^3r \tag{2.16}$$

in the following way:

$$\vec{\rho}_\perp = -\frac{1}{2\mu_B} \hat{q} \times (\vec{M}(\vec{q}) \times \hat{q}), \tag{2.17}$$

where $\hat{q}$ is the unit vector in the direction of $\vec{q}$. From the last equation we see that only magnetic moments perpendicular to $\vec{q}$ contribute to scattering.

The helix in MnSi has a defined chirality [27] [30] and therefore can be mathematically described in the following way: $\vec{S}(\vec{r})$ represents the local spin density and the direction of the spins of the conduction electrons at the position $\vec{r}$ within the sample. The spin density is therefore equivalent to the position-dependent magnetization within the sample. It is given as

$$\vec{S}(\vec{r}) = \vec{\alpha}_{\vec{Q}} \cos(\vec{Q}\vec{r}) + \vec{\beta}_{\vec{Q}} \sin(\vec{Q}\vec{r}), \tag{2.18}$$

where $\vec{Q}$ is the propagation vector of the helical structure. It points into the winding direction of the helix and points perpendicular to the spins of the electrons. It has the dimension of a wave number, where the wave length is the periodicity length of the helix (about 180 Å). Therefore, $\vec{Q}$ has the value $\frac{2\pi}{180\text{Å}}$. Furthermore, the amplitudes of the magnetization behave as follows:

$$\left|\vec{\alpha}_{\vec{Q}}\right| = \left|\vec{\beta}_{\vec{Q}}\right|, \tag{2.19}$$

$$\vec{\alpha}_{\vec{Q}} \perp \vec{\beta}_{\vec{Q}} \tag{2.20}$$

and

$$\vec{\alpha}_{\vec{Q}} \times \vec{\beta}_{\vec{Q}} \| \vec{Q}. \tag{2.21}$$

The Fourier transform of the position dependent magnetization

$$\vec{S}(\vec{q}) = \int \vec{S}(\vec{r}) \exp(i\vec{q}\vec{r}) d^3r \tag{2.22}$$

is then proportional to

$$\vec{S}_{\vec{Q}} \frac{(2\pi)^3}{v_0} \sum_{\vec{\tau}} \delta^3(\vec{q} - \vec{Q} - \vec{\tau}) + \vec{S}_{\vec{Q}}^* \frac{(2\pi)^3}{v_0} \sum_{\vec{\tau}} \delta^3(\vec{q} + \vec{Q} - \vec{\tau}), \qquad (2.23)$$

with $\vec{S}_{\vec{Q}} = \vec{\alpha}_{\vec{Q}} + i\vec{\beta}_{\vec{Q}}$, where $\vec{\tau}$ represents any reciprocal lattice vector and $\frac{(2\pi)^3}{v_0}$ represents the volume of the unit cell of the reciprocal lattice. It becomes clear that the helical structure results in two maxima, one at $\vec{q} = \vec{\tau} + \vec{Q}$ and the other at $\vec{q} = \vec{\tau} - \vec{Q}$. Because they always appear around a nuclear Bragg peak at $\vec{q} = \vec{\tau}$, they are called satellites of the respective Bragg peak.

The elastic neutron scattering by the helical structure can be described as Bragg scattering where the distance of the Bragg planes d corresponds to the periodicity length of the helix 180 Å. The direction of $\vec{Q}$ is considered as the normal to the Bragg planes. The Bragg scattering at the helical modulation is illustrated in figure 2.1.
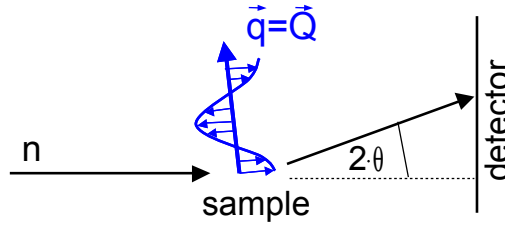

Figure 2.1: Bragg scattering of neutrons (n) at a helically modulated structure. The Bragg scattering angle θ is determined by the scattering vector $\vec{q}$, which is identical to the helical propagation vector $\vec{Q}$.

2.1.2 The diffractometer MIRA

The experiments on spin transfer torque were carried out by elastic neutron scattering on the diffractometer MIRA [90] at the Forschungsneutronenquelle Heinz Maier-Leibnitz (FRM II). Figure 2.3 shows MIRA with the experimental set-up used for the spin transfer torque experiment. A schematic depiction of the working principle of MIRA is given in figure 2.2.

The neutrons arriving from the neutron source have a broad velocity distribution (i.e. wave length distribution). At the multi-layer monochromator, neutrons with a defined momentum are scattered by Bragg reflection. The monochromator is shielded to stop unwanted neutrons and gamma rays. The monitor measures the neutron intensity. The measured signal is to be normalized by the monitor count. Two rectangular slits separated by a distance L1 are used in order to collimate the beam. Slit 1 is placed immediately after the monochromator, slit 2 is placed directly in front of the sample. The sample table, on which the sample with the entire sample environment (cryostat, magnet) is placed, can be rotated around a vertical axis by the angle ω. The scattered neutrons are measured by a position sensitive two dimensional ^{3}He wire chamber area detector (PSD), which is placed at a distance L2 from the sample.
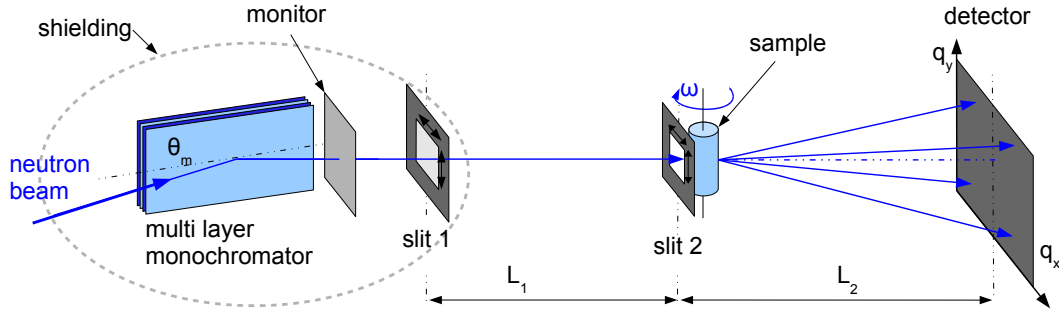
Figure 2.2: Schematic view of the diffractometer MIRA with monochromator, monitor, collimating slits, sample and area detector [38].


Figure 2.3: MIRA in the used set-up with cryostat (1), area detector (2) and monochromator shielding (3).

2.1.3   Inelastic neutron scattering with TAS

The spin fluctuations were measured with triple axis spectroscopy. In inelastic neutron scattering with a triple axis spectrometer (TAS), the scattering function $S(\vec{q}, \omega)$ is determined. The scattering function will be high (i.e. large signal) when it intersects the dispersion of an excitation.

The principal set-up is shown in figure 2.4. The neutrons arrive from the neutron source, and at the monochromator, neutrons with a defined momentum $\vec{k_i}$ are scattered by Bragg reflection. By using collimators or slits, the divergence of the neutron beam incident on the sample can be further reduced. A collimator is usually made of a number of thin neutron absorbing foils aligned parallel to each other and parallel to the neutron beam with a well-defined distance from each other. During the scattering process at the sample, a momentum transfer $\vec{q}$ and energy transfer ω occur (see equations 2.1 and 2.2). $\vec{k_f}$ is the wave vector after scattering. Afterward, the neutrons with wave vector $\vec{k_f}$ are selected by Bragg-reflection at the analyzer
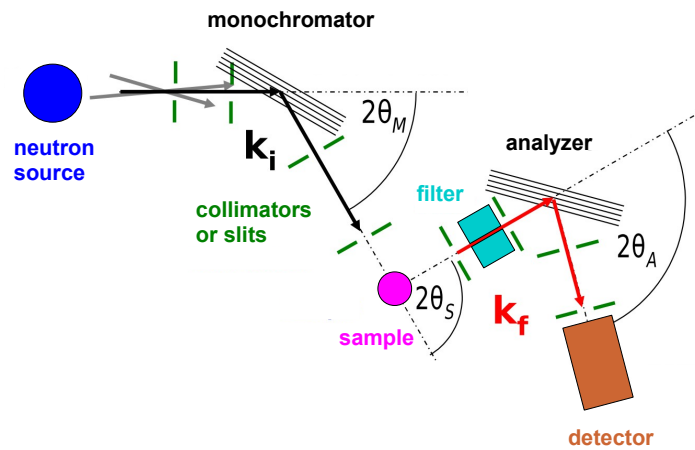
Figure 2.4: Principle of a triple axis spectrometer [36]. The neutrons from the neutron source are collimated by a collimator or by simple slits and are energy selected at the monochromator by Bragg scattering. The selected neutrons with wave vector k_i (also collimated by collimators or slits) impinge on the sample. The neutrons scattered at the sample with wave vector $\vec{k}_f$ are Bragg-scattered at the analyzer and pass onto the detector. Here, between sample and analyzer, a filter is inserted in the beam path in order to filter out neutrons scattered in higher order. The scattering angles at monochromator, sample and analyzer are indicated

crystal and pass onto the detector.

The monochromator and analyzer crystals are typically made of pyrolytic graphite crystals. The signal is always normalized to the monitor count. In order to exclude higher orders of the Bragg scattering from being detected, a filter is inserted in the beam path. The filter can be inserted between monochromator and sample or between sample and analyzer.

In figure 2.5, the triple axis spectrometer TASP at the Paul-Scherrer-Institut in Villigen/Switzerland is depicted. The beam path from source to detector through the instrument is indicated. The instrument is placed on a so-called "dance floor" made of granite in order to have a very smooth surface. All the components have air pads, making it very easy to move them. Then, a precise positioning of the components on the very smooth surface of the dance floor is possible by stepping motors.

Inelastic signals are usually weak. Their intensity can be raised by the following measures:

- The collimation can be reduced (meaning the distance between the layers of the collimator is enlarged) or the slits can be opened. This raises the beam divergence, so more neutrons from the source are used.

- Monochromator and analyzer crystals can have a mosaic. They consist of many individual crystals that are canted with respect to each other, thus generating an artificial crystal mosaicity. This leads to a larger beam divergence and to

the fact that a wave length band is selected from the neutron beam, in this
way using more neutrons from the source.

- The neutron beam can be focused onto the sample using a focusing monochro-
  mator or analyzer (or both of them focusing) so that they are oriented like
  a curved mirror pointing toward the sample. The curvature can be in the
  horizontal plane or it can be vertical or both.

  - Horizontal focusing raises the beam divergence but decreases the width of
    the selected energy band [91], i.e., the instrument resolution in momen-
    tum (q resolution) gets worse but the energy resolution is improved. More
    divergent neutrons from the source are used, thus raising the intensity.

  - Vertical focusing only makes the vertical q resolution worse. The vertical
    q resolution is decoupled from the q resolution in the horizontal plane and
    from the energy resolution. Therefore, more vertically divergent neutrons
    from the source are used without worsening the horizontal q resolution
    and the energy resolution.

All these measures lead to a relaxing of the instrumental resolution. This means
that not a point in the energy momentum space is investigated, but an area around
this point.
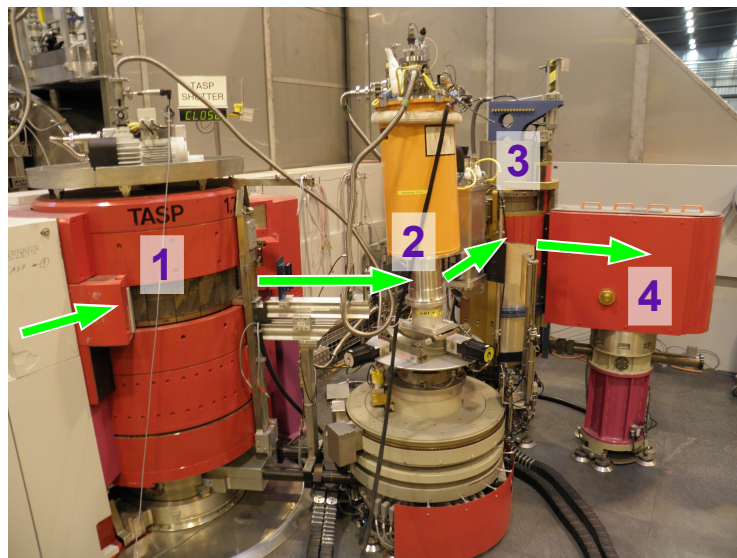
Figure 2.5: The triple axis spectrometer TASP at the Paul Scherrer Institut. The
neutrons from the source transported in a neutron guide are selected at the monochromator
(1). The shielding around the monochromator must be very thick to stop unwanted
neutrons and gamma rays. The selected neutrons impinge on the sample (here inserted
in an orange He flow cryostat with neutron transparent aluminum windows) (2). The
neutrons scattered at the sample are energy analyzed at the analyzer (3) and pass onto
the detector (4). Here, a nitrogen cooled Beryllium filter is placed in the beam path
between sample and analyzer. All the components have air pads in order to allow the
precise positioning by stepping motors.

2.1.4 Resolution with TAS

With a triple axis spectrometer, usually scans in the four-dimensional phase space spanned by $\mathbf{q}$ (which has the three coordinates q_x, q_y, q_z) and ω (only one dimension because it is a scalar) are carried out. A typical method is to fix the momentum at some value $\mathbf{q}_0$ and to scan the energy. This is called a constant q energy scan. Another typical scan is to fix the energy at one value ω_0 and to scan a direction of $\mathbf{q}$, e.g. the q_x direction, which can be identical with some crystalline axis of the sample. This is called a constant energy q scan.

In figure 2.6, a dispersion is shown and two energy scans, one at the steep part and the other one at the flat part of the dispersion. The finite spectrometer resolution is schematically shown as an ellipsoid in the (q_x, ω) plane. When the ellipsoid is scanned through the dispersion, then all points of the dispersion that fall into the ellipsoid contribute to the intensity. It is clear that due to the extended area of the resolution ellipsoid and due to its orientation in the plane, this can lead in one case (here at the flat part of the dispersion) to a sharp signal and in the other case to a very broad and weak signal.
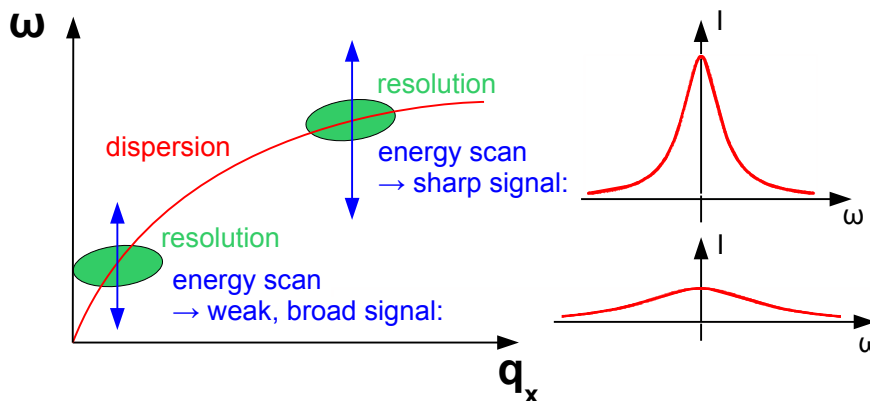
Figure 2.6: Measurement of a dispersion with energy scans. The q_x axis can be any crystalline orientation. Due to the extended resolution ellipsoid and its orientation in the (q_x, ω) plane, the scan at the flat part of the dispersion leads to a sharp signal and the scan at the steep part leads to a broad and weak signal.

The resolution function defines a four-dimensional ellipsoid in $(\mathbf{q}, \omega)$ space. It can be calculated for all the points of a scan (see [92], [93] and [94]) when the instrument parameters (e.g., collimations in all spectrometer arms, wave length of the neutrons etc.) are known. In practical use, the resolution function is calculated by computer programs. When additionally the parameterized scattering function is entered, then the resolution function is convoluted numerically in each fitting step with this parameterized scattering function.

## 2.2 Experimental set-up for spin transfer torque measurements

2.2.1 General set-up

The experiments on spin transfer torque were carried out on the diffractometer MIRA [90] at the Forschungsneutronenquelle Heinz Maier-Leibnitz (FRM II) described above.

For our experiments, neutrons with a wave length of $\lambda \approx 9.7\,\text{Å}$ were used. The neutron beam was collimated by a system of slits. The detector resolution of the measurements was $A_D = 2\,\text{mm} \times 2\,\text{mm}$, the radiated area on the sample was approximately $A_P = 4\,\text{mm} \times 2\,\text{mm}$, and the sample-detector distance was $L_2 = 124\,\text{cm}$.

According to the Bragg condition $\lambda = 2d \sin \theta$, the neutron wave length leads to a scattering angle of $\theta \approx 1.7°$ for the peaks of the helical structure. We measured around the direct beam.

When a $\langle 110 \rangle$ axis of the crystal points into the beam direction and all four domains of different helix orientations pointing into the different $\langle 111 \rangle$ axes are populated, one expects four different satellite maxima originating from the two helix domains in the plane perpendicular to the beam. This configuration is shown in figure 2.7. The azimuthal angular width of the diffraction peaks $\Delta \Phi$ is the angular distribution of the helimagnetic domains in the plane perpendicular to the beam. The mosaicity $\Delta \Psi$ is the angular distribution perpendicular to the detector plane. When current was sent through the sample, it was always applied in vertical direction.
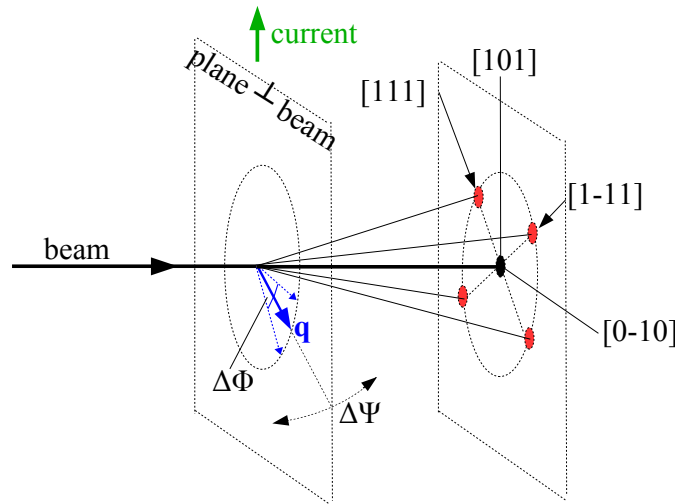
Figure 2.7: Diffraction at helical modulation in MnSi and definition of mosaicity ($\Delta \Phi$ and $\Delta \Psi$).

For measuring the A-phase (which needs a magnetic field), we used two different set-ups in our experiments. In the set-up mainly used (set-up I), the magnetic field was parallel to the neutron beam direction. It was the preferred set-up because the

modulated structure of the skyrmion lattice in the A-phase orients perpendicular to the field. This means that with this set-up, the full hexagonal diffraction pattern of the skyrmion lattice can be seen on the detector. Furthermore, only in set-up I were spin transfer torque effects observed. Set-up I is shown in figure 2.8(a). The set-up with magnetic field in vertical direction is shown in figure 2.8(b). In this configuration (set-up II) the modulated magnetic structure of the skyrmion lattice lies in the horizontal plane. Therefore, only two diffraction peaks of the hexagonal pattern can be made visible on the horizontal axis of the detector.
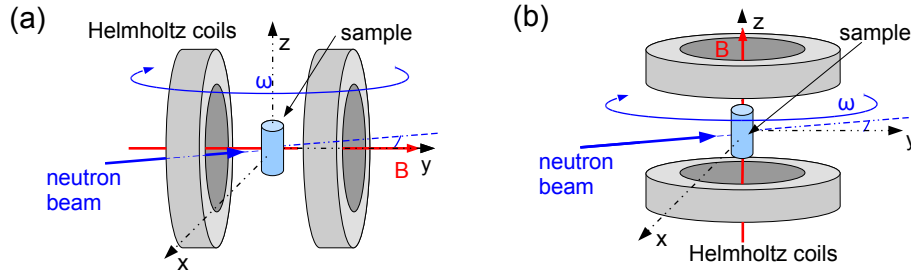
Figure 2.8: (a) Schematic view of set-up I. The magnetic field generated by the Helmholtz coils is oriented parallel to the beam. This set-up was mainly used throughout the experiments. (b) Schematic view of set-up II. The magnetic field of the Helmholtz coils is oriented in vertical direction.

2.2.2   Sample environment

The experiments on MIRA were carried out in a closed-cycled cryogen free pulse tube cooler (3.5 K - 300 K) and a water cooled magnet (0 - 0.5 T) comprising two copper coils in a Helmholtz configuration [87]. Figure 2.9 shows the cryostat and the magnet. A heater was used that allowed to heat the entire sample tube, thus minimizing temperature gradients. The cryostat (made of Al) has thin-walled windows at the lower part where the sample is located, in order to make the cryostat transparent for neutrons. The sample tube was filled with several hundred millibar He exchange-gas pressure.

An already existent sample stick was modified in order to allow for a current through the sample. The current is led down to the sample holder through cylindrical brass rods and through insulated wire.

In the measurements, a good electric contact of the sample to the current feeds and the elimination of parasitic temperature gradients in the sample turned out to be the main experimental challenges. Figure 2.10 and figure 2.11 show the front view and the back view of the bespoke sample holder.

Initially, it was aimed at minimizing any temperature gradient, allowing for a homogeneous temperature over the whole sample. For this purpose, the sample was thermally connected to a massive heat sink made of copper. This connection should have a large surface in order to enable the rapid removal of the ohmic heat created by the current in the sample, i.e. necks of the thermal conductivity had to be avoided.
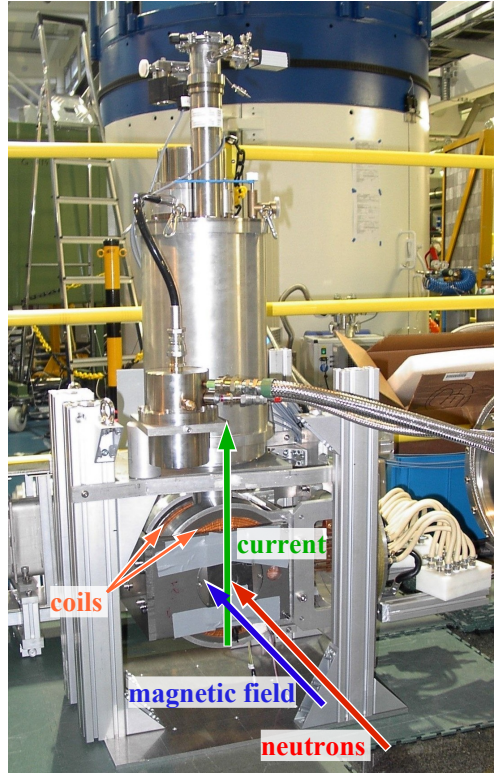
Figure 2.9: Cryostat (top) with Helmholtz magnet (bottom) in the set-up with magnetic field parallel to the neutron beam. Direction of current through the sample, direction of external magnetic field generated by the Helmholtz magnet and direction of neutron beam are indicated.

Furthermore, the heat sink should have a big mass leading to a large heat capacity. Therefore, copper was used for the heat sink.

However, the sample was not directly connected to the copper but was glued onto an aluminum window embedded in the heat sink, allowing for the neutrons to pass easily through the sample (aluminum is much more transparent for neutrons than copper). For an easier mounting, the sample was glued with GE varnish onto a small aluminum socket within the aluminum window. To insulate the sample electrically from the aluminum window (respectively the heat sink), we used cigarette paper and a thin layer of GE varnish.

The sample was soldered at both ends to thin bent copper bands, which served as springs pressed to the sample in order to maintain a good electric contact to the sample. These copper bands, in turn, where screwed onto thermal anchors with a cuboid shape, which, having a large contact surface with the heat sink, should provide a good thermal contact between the current leads and the heat sink. This helps to cool the current leads, which is not only important because of the ohmic heating generated by the current but also because of the heat flow due to the temperature gradient between the top and the bottom end of the sample stick. The thermal anchors (that are part of the current leads) were electrically insulated from the heat sink by capton foil.

The current leads were guided through holes into the sample area. Within these

holes, the electrical insulation against the heat sink was ensured by Stycast-Epoxy 2850 FT (the hardened glue keeps the current lead separated from the heat sink). At this place, there is an additional thermal coupling of the current lead to the heat sink through the Stycast-Epoxy, which is a good thermal conductor. The Stycast-Epoxy, which has a black color, can be seen in the picture of the sample holder figure 2.10 at the left hand side, where the current leads go through the heat sink.

The heat sink was equipped with two holes for two heaters to be inserted (one at the bottom end, the other at the top end). The heaters were only used for tests but not during data collection. Instead, a heater was utilized that allowed to heat the entire sample tube.

A resistive Pt 1000 temperature sensor was attached to the sample surface with GE varnish (the sensor did not generate any noticeable background signal in neutron scattering). The electrical insulation from the sample was achieved with cigarette paper. Additional temperature sensors (visible in figures 2.10 and 2.11) were applied to monitor the temperature difference between sample surface and heat sink (main body of the sample holder). One Pt 1000 thermometer was placed near the sample on the heat sink (visible in figure 2.10). At the back of the sample holder (see figure 2.11) a third Pt 1000 thermometer is mounted. It is inserted in an aluminum block screwed onto the sample holder. Next to it, the fourth thermometer, a cylindrical Cernox thermometer, is visible.

Finally, a cadmium mask was mounted at the back of the sample holder (see figure 2.11). As cadmium is nearly opaque for neutrons, a rectangular window in the mask should only expose the central part of the sample to the beam. It was intended to examine only a part of the sample (namely the central part) because it was assumed that the temperature over this selected tiny part of the sample would be rather homogeneous.

Finally, an aluminum tube was screwed over the sample holder. The thread holes in the sample holder are visible in figure 2.10 and figure 2.11. The aim was that the He exchange gas (with a pressure of several hundred millibar) combined with the good thermal coupling of the aluminum tube to the copper sample holder should homogenize the temperature over the sample holder, eliminating parasitic temperature gradients.
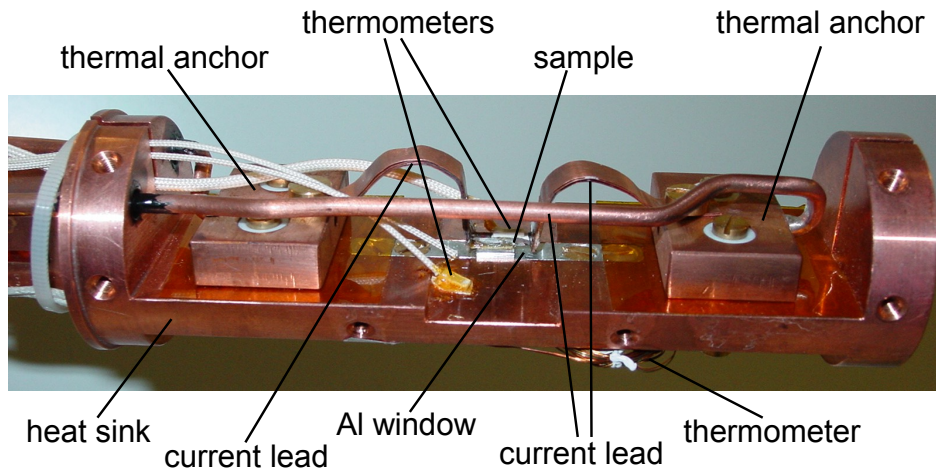
Figure 2.10: Sample holder. The sample is glued onto an aluminum window embedded in massive amounts of copper of the heat sink. Two Pt 1000 thermometers, one glued onto the sample, the other glued onto the heat sink next to the sample, are visible. A third thermometer (not entirely visible) which is fixed on the back of the sample holder is also indicated. The current leads are visible, which consist of copper bands directly connected to the sample, thermal anchors for thermal coupling to the heat sink and copper rods.
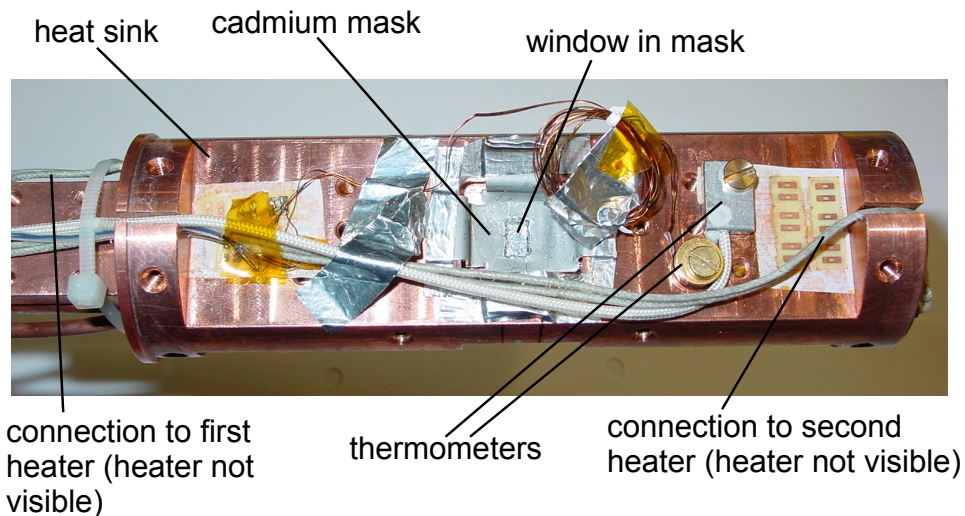
Figure 2.11: Back view of the sample holder. One can see the cadmium mask with a rectangular window in it for the neutrons to pass through the sample. Two additional thermometers are visible, one Pt 1000 inserted in an aluminum block screwed onto the heat sink and one cylindrical shaped Cernox thermometer. The thin wires are the thermometer connections, the thick wires are the connections for the heaters.

2.2.3   Samples

We studied six different samples. The samples were either prepared by Bridgman growth or optical float zoning. All samples were single crystals with high residual resistance ratios (RRR) around 100 and residual resistivity around $\rho_0 \approx 2\,\mu\Omega$cm.

An overview of all the samples that were examined by neutron scattering in the spin transfer torque measurements is presented in table 2.1. The length in vertical direction (which is identical to the direction of the current flow), the width in the direction perpendicular to the neutron beam and the thickness in the direction of the neutron beam are given. The crystalline orientations of the respective sample directions are also indicated. Sample (v) was not used in spin torque measurements, because it is not rectangular (which would mean a non uniform current density). It was measured in order to examine the skyrmion structure in a sample with a different shape and therefore different demagnetization effects, enabling to study the role of demagnetizing fields.

Table 2.1: Dimensions and crystalline orientations of the samples measured with neutron scattering on MIRA.

	length	thickness	width
sample (i)	$\sim 10\,\mathrm{mm}$ $[1\bar{1}0]$	$\sim 1.5\,\mathrm{mm}$ $[110]$	$\sim 1.8\,\mathrm{mm}$ $[001]$
sample (ii)	$\sim 10\,\mathrm{mm}$ $[1\bar{1}0]$	$\sim 1.7\,\mathrm{mm}$ $[110]$	$\sim 1.9\,\mathrm{mm}$ $[001]$
sample (iii)	$\sim 10\,\mathrm{mm}$ $[1\bar{1}0]$	$\sim 0.5\,\mathrm{mm}$ $[110]$	$\sim 4\,\mathrm{mm}$ $[001]$
sample (iv) not oriented single crystal	$\sim 12\,\mathrm{mm}$	$\sim 1.4\,\mathrm{mm}$	$\sim 1.95\,\mathrm{mm}$
sample (v)	$\sim 8\,\mathrm{mm}$ $[1\bar{1}0]$	$\sim 0.8\,\mathrm{mm}$ $[110]$	$\sim 15\,\mathrm{mm}$ $[001]$
sample (vi)	$\sim 5\,\mathrm{mm}$ $[1\bar{1}1]$	$\sim 1.5\,\mathrm{mm}$ $[1\bar{1}\bar{2}]$	$\sim 1.8\,\mathrm{mm}$ $[110]$

2.3 Experimental set-up for measurements of spin fluctuations

The measurements of the spin fluctuations were carried out at the triple axis spectrometers PANDA at the FRM II in Munich and TASP at the PSI in Villigen/Switzerland. Two different samples were examined: pure MnSi and $Mn_{1-x}Fe_xSi$. The pure MnSi sample was studied because the data already known from MnSi measurements by Ishikawa *et al.* [5] [6] were to be confirmed. MnSi was measured on PANDA, $Mn_{1-x}Fe_xSi$ was measured on PANDA and TASP (see table 2.2).

The MnSi sample is shown in figure 2.12 (a). The sample has an irregular shape. It is clamped into an aluminum holder, which is screwed onto an aluminum cylinder. Figure 2.12 (b) shows the $Mn_{1-x}Fe_xSi$ sample.

The samples were put into a closed cycle cryostat at PANDA and into a Helium flow cryostat at TASP. The instruments were always in the so-called W configuration. This is the set-up most often used when measuring with a triple axis spectrometer. Here, the scattering sense at the monochromator is the same as the scattering sense

(a)   (b)
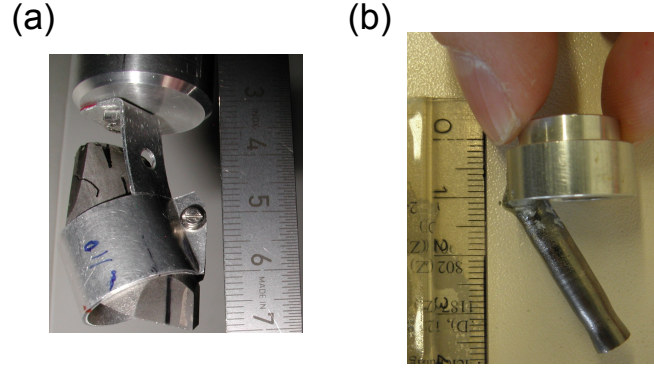
Figure 2.12: (a) The irregularly shaped MnSi sample is fixed in an aluminum holder, which is screwed onto an aluminum cylinder. (b) Cylinder-shaped $Mn_{1-x}Fe_xSi$ sample glued onto an aluminum socket.

at the analyzer. The scattering sense at the sample is opposed to both the scattering sense at the monochromator and the analyzer. Therefore, the spectrometer arms form a W. The filter (made of Beryllium) was placed after the monitor.

The samples were always oriented with a crystalline $\langle 110 \rangle$ axis pointing in the vertical direction. Therefore, the horizontal scattering plane is spanned by a $\langle 110 \rangle$ and a $\langle 100 \rangle$ axis.

After finding the nuclear Bragg peaks in the horizontal scattering plane, the alignment of the crystal had to be optimized so that the horizontal scattering plane coincides with the crystalline plane. This is achieved by tilt scans of the nuclear Bragg peaks. Furthermore, the lattice constant had to be determined, which was done by a $\theta - 2\theta$ scan. The resulting lattice constant for $Mn_{1-x}Fe_xSi$ was $4.56\,\text{Å}$ and $4.55\,\text{Å}$ for MnSi.

In all experiments, the magnetic signal around the nuclear Bragg peak (110) was measured, because it has high intensity (due to the structure factor). In MnSi, magnetic satellite peaks appear in the $\langle 111 \rangle$ directions with respect to the nuclear peak. In $Mn_{1-x}Fe_xSi$, the elastic magnetic scattering below T_c appears on a sphere in reciprocal space around the nuclear Bragg peak [38]. As a preliminary measurement, the transition temperature T_c of the sample used in the experiment was determined. This was done by temperature scans on the elastic signal of the magnetic satellite.

Table 2.2 gives an overview of the three experiments done on spin fluctuations, with the instrument used, the studied sample and the focusing conditions of monochromator and analyzer.

Table 2.2: Experimental details: Used instrument, studied sample and focusing conditions

instrument	sample	monochromator	analyzer
PANDA	MnSi	no focusing	no focusing
PANDA	$Mn_{1-x}Fe_xSi$	horizontal focusing	horizontal focusing
TASP	$Mn_{1-x}Fe_xSi$	no focusing	horizontal focusing

The measurements comprised taking quasi-elastic spectra at different q vectors to determine the linewidths of the fluctuations and their q dependence. In all the energy scans shown, negative energy transfer means that the neutrons gain energy in the scattering process (neutron energy gain side). Positive energy transfers mean that the neutron loses energy in the scattering process (neutron energy loss side).

Chapter 3

Results of the spin transfer torque experiment

3.1 Rocking curves and demagnetizing effects

The diffraction experiments start with finding the Bragg peaks of the magnetic structure. This is achieved by so-called rocking scans, where the sample table with the Helmholtz magnet is rotated around the vertical axis. When the scattering intensity is plotted versus the rotation angle, the maximum of the intensity yields the Bragg angle and the width of the rocking curve yields the mosaicity, i.e., the statistical spread of the q vectors around the mean Bragg angle. In figure 3.1 two such rocking scans are presented.

Figure 3.1 (a) shows on the left the scattering picture of the helical phase in MnSi with no current running through the sample at $16\,\mathrm{K}$ and zero magnetic field, where the propagation directions of the helices are parallel to the crystalline $\langle 111 \rangle$ directions. The data of figure 3.1 was measured with sample (ii). The direction of the neutron beam is perpendicular to the plane of the picture, i.e., the line of sight is the neutron beam path (this is also the case in all the following scattering pictures). The viewing direction in all the scattering pictures points into the neutron beam, i.e, toward the neutron source at the reactor. The picture is the sum of all scattering intensities at all rocking angles of a rocking scan.

The line of sight, which is the direction of the neutron beam, is a crystalline $\langle 110 \rangle$ axis, which in this cubic symmetry means that the plane perpendicular to the beam is spanned by a crystalline $\langle 110 \rangle$ axis (vertical direction) and a $\langle 100 \rangle$ axis (horizontal). The $\langle 111 \rangle$ directions also lie in this plane.

The first order diffraction peaks are the peaks 2, 3, 5 and 6. The peaks 1 and 4 that lie on the horizontal axis and which have much less intensity, are produced by double scattering, i.e. peak 1 is produced by neutrons scattered by the helix pointing into the direction of peak 2 and subsequently scattered by the helix pointing into the direction of peak 6. The red dashed lines point from the center (direct beam) to the respective peaks. The direct beam is masked here in order to better observe the

diffraction peaks. In the following, the direct beam will always be masked.

On the right side, the rocking curves of the first order peaks are shown. The intensity of the domain represented by peak 3 (top right) and peak 6 (bottom left) is much smaller than the intensity of the other domain represented by peak 2 (top left) and peak 5 (bottom right). This can be an effect of unequal domain population. The black lines are Gaussian fits to the data. The full width at half maximum of the curves correspond to the magnetic mosaicity $\eta_m \approx 3.5°$.

Figure 3.1 (b) shows on the left the scattering picture of the same sample as in (a) but in the A-phase at a magnetic field of $0.175\,\mathrm{T}$ at $27.7\,\mathrm{K}$ and zero current through the sample. The negative magnetic field value (see picture) means that the magnetic field points out of the plane, (indicated on bottom right of the picture). This directional convention will be maintained throughout the whole text. The crystalline orientation is the same as in (a).

The peaks are distributed in a hexagonal pattern, i.e., the angle between two peaks is 60°. The hexagonal scattering pattern is only encountered when the magnetic field is parallel to the neutron beam, regardless of the crystalline orientation, because the skyrmion lines are always parallel to the applied magnetic field. The structure is weakly coupled to the crystalline $\langle 110 \rangle$ direction [1] [4] [95] [96]. This means that when a $\langle 110 \rangle$ axis lies in the plane perpendicular to the magnetic field, then one direction of the hexagonal pattern points into this $\langle 110 \rangle$ direction (which are the spots 2 and 5 on the vertical axis here).

The diffraction picture is, like in (a), the sum over a rocking scan. Because it was rocked around a vertical axis, the spots 2 and 5 lying on the vertical axis are much weaker than the other spots. This is due to the fact that they cannot be rocked into the Bragg condition because they lie on the vertical rocking axis. They only show up weakly due to finite mosaicity.

On the right, the corresponding rocking curves are shown for the four peaks 1, 3, 4 and 6. The intensity is evenly distributed within the four spots.

The shapes of the rocking curves in (b) (the angular range of the rocking curves in (a) and (b) is the same) are rather odd and not Gaussian like in (a). This is due to demagnetizing fields [1] [4] [95]. Additionally, the width of the rocking curves is considerably smaller than in (a). This means that the correlation length of the skyrmion lattice is very large compared to the helical structure [1] [4] [95].

Demagnetizing fields are fringe effects. This is schematically depicted in figure 3.2 [1] [4]. When the sample surface is not perpendicular to the magnetic field, the magnetic field lines through the sample are deflected by an angle α, meaning that the field direction outside of the sample is not the same as inside the sample. The idea is that the length of the magnetic field lines running through the sample is to be maximized. Because the skyrmion lattice is always perpendicular to the field in the sample, this means that the skyrmion lattice is no longer perpendicular to the applied magnetic field but also shifted by the angle α. This gives an idea how the fields can be deflected by the sample shape. Also more complicated field distributions within the sample are thinkable, which could explain the odd shape of the rocking
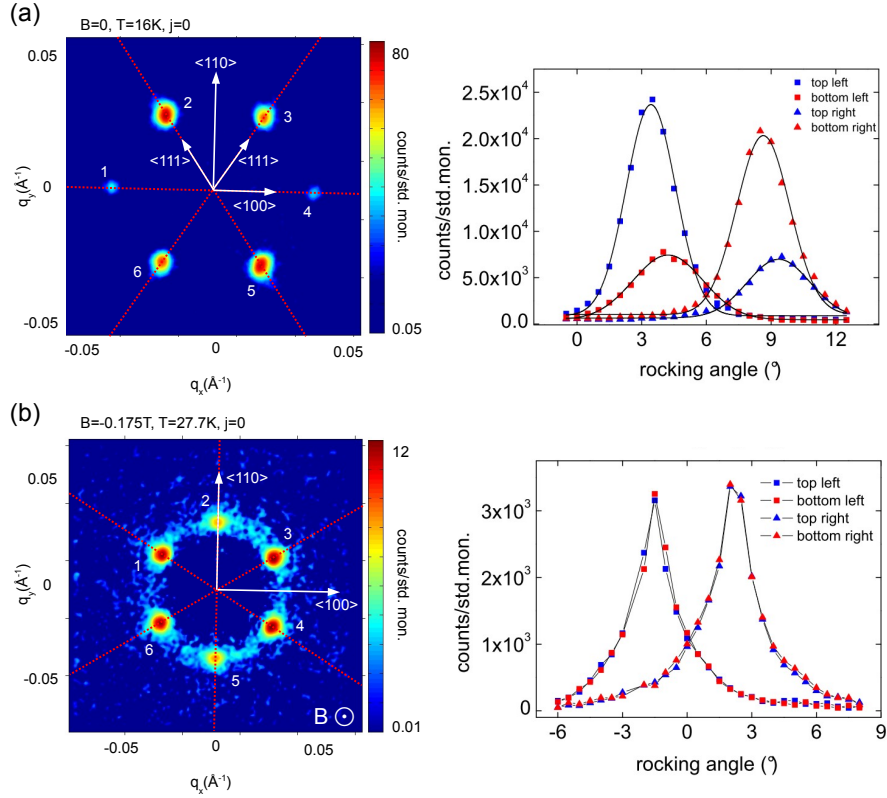
Figure 3.1: (a) Left: Scattering picture (sum picture of rocking scan) of helical phase at zero magnetic field, 16 K and zero current. Field, temperature and current are indicated on top left of the picture. White lines show crystal directions. Red dashed lines are drawn through the peaks. Right: Rocking curves for the peaks 2, 3, 5 and 6. Data is fitted by Gaussians. (b) Left: Scattering picture (sum picture of rocking scan) of A-phase at magnetic field of -0.175 T (pointing in negative direction, out of the plane), 27.7 K and zero current. Right: Rocking curves of the skyrmion lattice show a shape different from those in (a). Pictures are taken from [4].

curves in figure 3.1 (b).
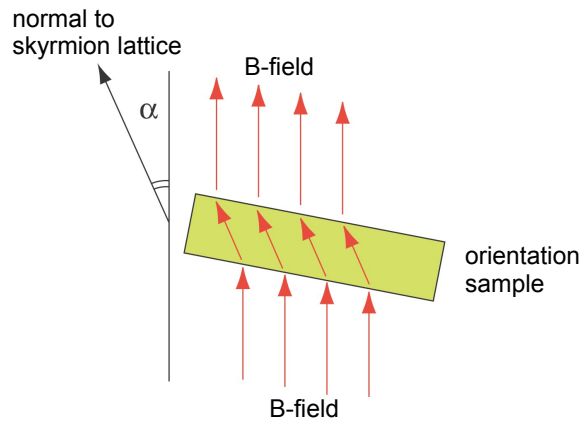
Figure 3.2: Schematic view (from above) of the variation of the magnetic field lines across the sample. Due to demagnetizing effects, the internal field neither coincides with the tilting angle nor with the incident neutron beam. The skyrmion lattice is perpendicular to the internal field. Picture is taken from [4].

In order to study the demagnetization effects in more detail, rocking scans of the helical order and the skyrmion lattice were measured in a sample with a different shape (sample (v)). The sample was flat and only few tenths of a mm thick with a maximal length of roughly 15 mm. It was positioned perpendicular to the magnetic field and incident neutron beam. By applying a cadmium mask, only the central part of the sample was examined, thus avoiding fringe effects. This way, the internal field distribution is assumed to be extremely narrow.

Typical rocking scans observed in this configuration are shown in figure 3.3. Figure 3.3 (a) shows on the left side the summed-up intensity of a rocking scan in the helical phase at zero magnetic field and 10K. The same peaks as in figure 3.1 (a) show up, but turned by 90° compared to figure 3.1 (a) due to the fact that the crystalline orientation (see the labeled white lines) is turned by 90° with respect to figure 3.1 (a). The corresponding rocking curves for the four peaks are shown on the right. In this case, the domain represented by peak 1 (top left) and peak 3 (bottom right) is weaklier populated than the domain represented by peak 4 (bottom left) and peak 2 (top right). Each peak is fitted by a Gaussian, giving a mosaicity η_m of approximately 3.5° in excellent agreement with all previous studies and the literature.

Figure 3.3 (b) shows the summed-up intensity of a rocking scan in the A-phase at a magnetic field of 0.175 T and a temperature of 27.7 K. Due to the crystal orientation (white labeled lines), the scattering picture is turned by 90° with respect to the scattering picture in figure 3.1 (b). Now, two peaks (peak 1 and peak 4) lie on the horizontal axis. The rocking curves of the horizontal peaks directly yield the Bragg angle and the mosaicity.

On the contrary, when there is an angle β between the horizontal axis and the diffraction peak (here, for example, the angle β between the horizontal axis and peak 2, peak 3, peak 5 or peak 6 is 60°) then the Bragg angle increases for small β by approximately the factor $\frac{1}{\cos(\beta)}$. The width of the rocking curve, the mosaicity, is increased by the same factor. This is due to the fact that for the non-horizontal q vectors the sample has to be further rotated in order to turn the q vectors into the Ewald sphere.

This phenomenon is seen in the corresponding rocking curves on the right hand side of (b). The horizontal peaks (black data) show up at smaller rocking angles than the other four peaks. Also, their widths are much smaller than the other peak widths. Each peak was fitted by a Gaussian. In contrast to the rocking curves of the skyrmion lattice in the spin torque sample in figure 3.1 (b), the shape of the rocking curves is Gaussian. The small rocking width of the skyrmion lattice (0.5°) is almost an order of magnitude smaller than the width in the helical phase (the rocking curves in (a) and (b) have the same angular scale). It is assumed that this small width is basically resolution limited.

This strongly suggests that the odd non-Gaussian shape of the rocking curves of the spin torque sample in figure 3.1 (b) results from the distribution of demagnetizing fields in the sample, as it was shown that a sample where the distribution of the demagnetizing fields was deliberately kept very narrow showed a typical Gaussian shape. This implies that the skyrmion lines follow the internal field distribution and

the skyrmion lattice exhibits well-developed long range order. This is an important assumption for the discussion of our data later.
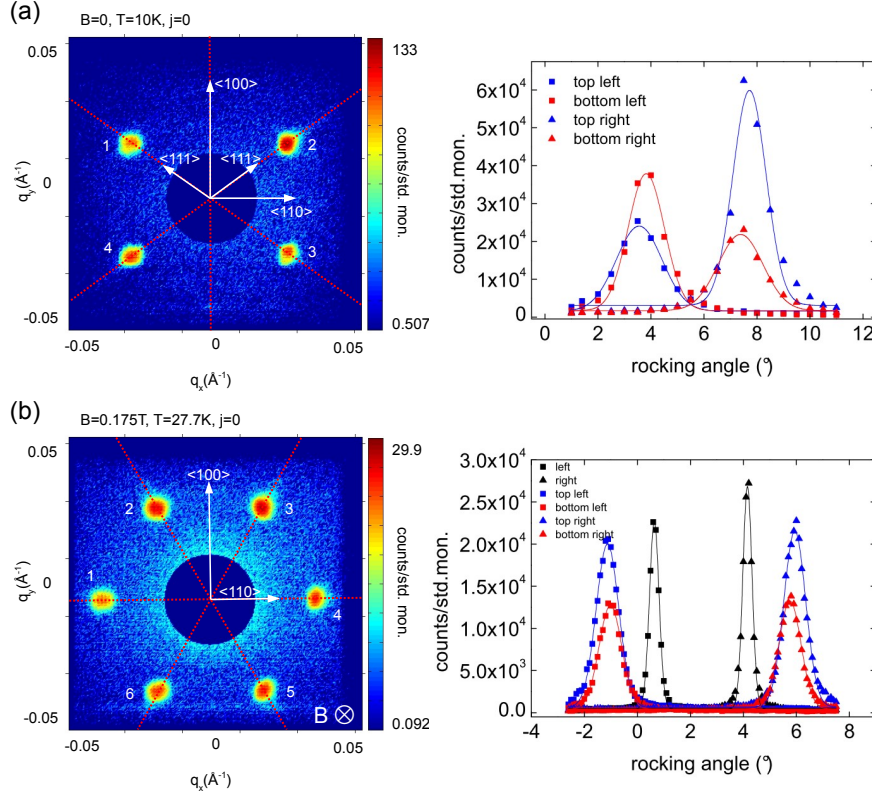

Figure 3.3: Rocking curves measured with sample (v). (a) Left: Sum over rocking scan in the helical phase at zero magnetic field and 10 K. The crystal orientation is now with the $\langle 100 \rangle$ axis in vertical direction. The peaks show up on the crystalline $\langle 111 \rangle$ directions. Right: Corresponding rocking curves. Data is fitted by Gaussians. (b) Left: Sum over rocking scan in the A-phase. The hexagonal pattern is fixed with two spots on the horizontal $\langle 110 \rangle$ axis. Right: Corresponding rocking curves for all six spots. Data is fitted by Gaussians. The mosaicity is much narrower than in (a). The shape of the rocking curves is different from the one in figure 3.1 (b), which was measured with a rectangular spin torque sample.

Until now, only rocking scans around the vertical axis have been described. Therefore, peaks lying on the vertical axis cannot be rocked into the Bragg condition. In order to get also these peaks into the Bragg condition, a tilting of the sample, which is equivalent to a rocking around a horizontal axis, was necessary.

Figure 3.4 shows such a tilt scan for the spin torque sample (sample (i)). Figure 3.4 (a) is a picture of the summed-up intensity of the scan. The magnetic field was 0.175 T and the temperature was 27.7 K. In this picture, the spots on the vertical axis have quite high intensity because they were tilted into the Bragg condition during the scan.

Figure 3.4 (b) shows the corresponding curves where the intensity is plotted versus the tilting angle. The peaks 2 and 5 on top and bottom (black data) show up as sharp peaks at the respective Bragg angles. The other peaks shown in blue (top spots) and red (bottom spots) are at higher tilt angles and are much broader, as they

are closer to the rocking (here tilting) axis. This phenomenon was already described above, in figure 3.3 (b), the only difference here is that the vertical rocking axis is replaced by a horizontal tilting axis. Therefore, the situation is just rotated by 90°. The fact that the blue and red curves are much broader and have less intensity than the black curves is probably again due to some demagnetization effect resulting from the long rectangular sample shape.
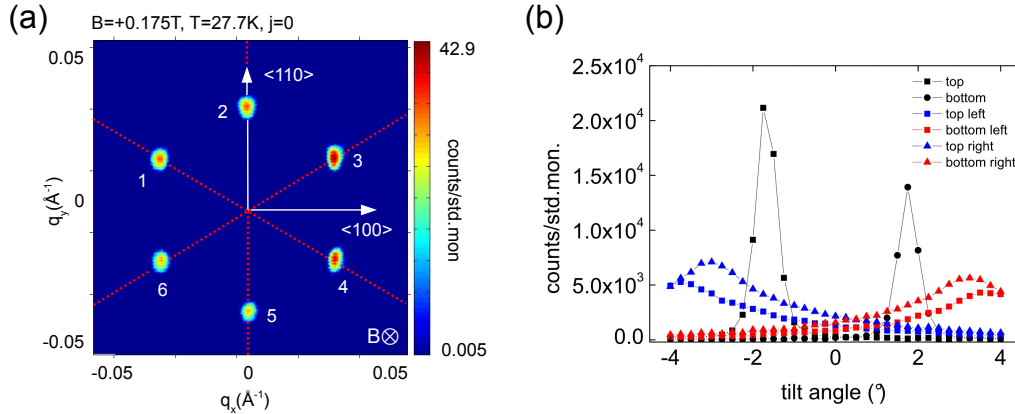
Figure 3.4: (a) Left: Sum picture over tilt scan in the A-phase measured with the spin torque sample (sample (i)). The tilting brings the peaks on the vertical axis into the Bragg condition, therefore they have high intensity. (b) Tilting curves, where scattering intensity versus tilt angle is plotted for all six spots in (a). The spots at top and bottom have sharp maxima.

In order to save time, the Bragg angles were determined at the beginning of the measurements by rocking and tilting scans. Then, in the actual measurements, the sample was consecutively rotated or tilted into the Bragg angles and the signal was counted. In the end, the intensities of the scattering patterns obtained at each Bragg position were summed up in order to have a scattering pattern of the A-phase with all six spots at high intensity.

3.2 Method of data analysis

An important part of the data analysis in the following will consist in obtaining information on the angular position of the peaks within the diffraction pattern and the width and intensities of the peaks. As the absolute values of the q vectors of all first order peaks both in the helical phase and in the skyrmion lattice of the A-phase are the same, the method illustrated in figure 3.5 will be applied for a quantitative analysis.

Figure 3.5 (a) shows a diffraction pattern in the A-phase with all six spots at high intensity. A ring between the white circles is defined so that the peaks are placed fully in the ring. Then, the intensity along the ring is binned into an azimuthal angle step, which for this analysis was chosen to be 1°. This leads to the diagram of figure 3.5 (b) where the intensity within the ring is plotted versus the azimuthal angle. The peak numbers in (a) correspond to the peak numbers in (b). The convention

for the angular scale is shown in (a). The zero angle is vertically on top. Clockwise, the angles are positive, anti clockwise, the angles are negative. The peak at 180° is identical to the one at -180°. The analysis then consists in fitting Gaussians on each peak in figure 3.5 (b):

$$f(x) = \frac{A}{\sigma\sqrt{2\pi}} \exp\left(-\frac{1}{2}\left(\frac{x - x_0}{\sigma}\right)^2\right) \tag{3.1}$$

The relevant parameters for the analysis are the peak center x_0, the azimuthal width of the peak σ, or rather the FWHM, which is

$$\text{FWHM} = \sigma \cdot 2\sqrt{2\ln 2},$$

and the integrated intensity A.
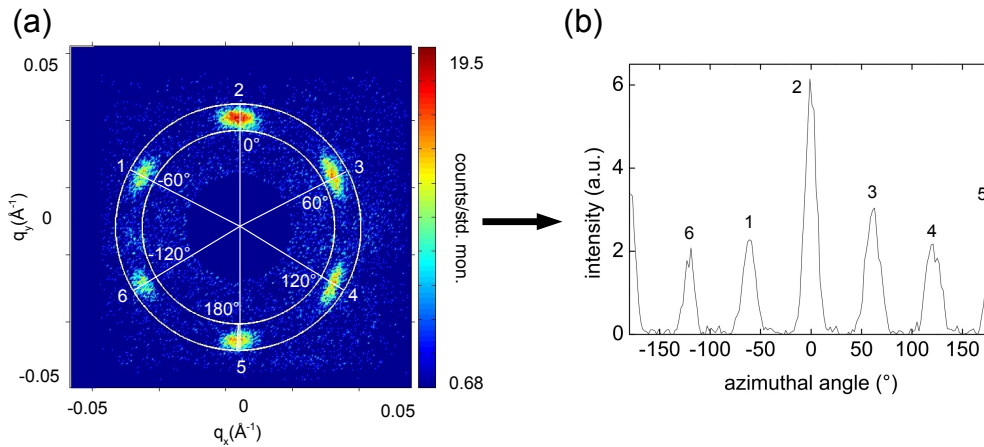
Figure 3.5: Procedure for analyzing the azimuthal angles. (a) A ring is drawn which contains the diffraction spots. The intensity within that ring is binned in angular intervals of 1° and plotted in (b) in dependence of the azimuthal angle. The peak numbers in (a) correspond to the peak numbers in (b). The angular scale is defined in (a): vertical on top is 0°. Clockwise, the angles are rising. Anti clockwise, the angles become negative.

3.3   Helical phase under current

At first, the helical phase with current through the sample was examined. The effects on current on the helical phase are illustrated in figure 3.6. Figure 3.6 (a) shows the scattering picture in the helical phase at zero magnetic field at a temperature of 13 K and with no current through the sample. The scattering picture in 3.6 (a) is taken at a fixed rocking angle. Therefore, due to the non-perfect crystal orientation, the intensities of the peaks differ from each other to a large extent. For example, peak 2 is very weak compared to the other peaks. Peak 1, which would result from double scattering, is completely missing.

In figure 3.6 (b), a current through the sample with a density of $j = 1.48 \cdot 10^6 \, \text{A/m}^2$ was applied. As the current is positive, the current direction (technical current direction) is pointing upward in vertical direction, as indicated on bottom right.

When comparing (b) with (a), no qualitative difference of the scattering pattern can be observed. In figure 3.6 (c) the current density was increased to the value $j = 2.22 \cdot 10^6 \, \text{A}/\text{m}^2$. When comparing (c) with (a) and (b), no changes are visible. The positions of the peaks have not changed, and the intensities of the peaks are virtually the same in all three pictures, which indicates that the domain population in the helical phase is not affected by the current.

This means that, within the instrumental resolution, current-induced effects could not be observed in the helical phase. Therefore, most experiments were carried out in the A-phase, because, as we will see, current-induced effects in the A-phase could be easily detected with the used experimental set-up.
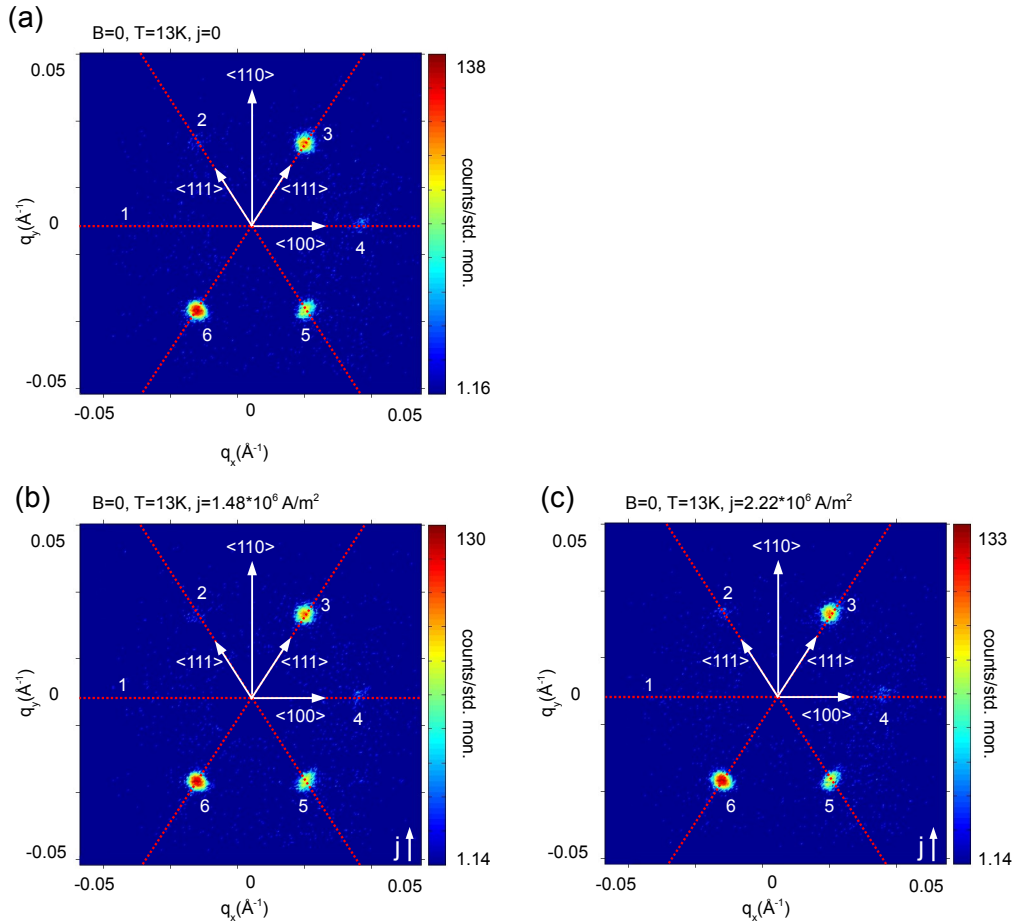
Figure 3.6: (a) Scattering picture at one rocking angle of helical phase at zero magnetic field and 13 K without current through the sample. Peaks are along the $\langle 111 \rangle$ directions. Peak 2 is very weak due to non-perfect crystal alignment. Peak 1 (not visible due to the scaling) and peak 4 on the horizontal axis are double-scattering peaks. (b) The sample under the same conditions of magnetic field and temperature and the same rocking angle as in (a) but under current flow. No changes are observed compared to (a). (c) Same conditions, but higher current. No changes are observable.

3.4 Skyrmion lattice under current

In the following, we show the measurements of the A-phase with current flow through the sample. A temperature gradient in the sample with well-defined direction was necessary to observe the spin transfer torque effects. Therefore, directionally well defined gradients were applied on the sample. This was achieved by glueing the sample onto the sample holder in a way that one end was firmly attached to the heat sink, and the other not. Then, by applying an electric current through the sample, ohmic heat would be generated, and the end of the sample firmly attached to the heat sink would be colder than the other end, creating a vertical temperature gradient. This was done by a small wedge of GE varnish between the aluminum socket and the sample, which was created by keeping one end of the sample at a small distance from the sample holder with the help of a plastic support underneath the sample.

This is depicted in figure 3.7. In (a), the set-up where the sample is firmly attached to the heat sink is shown. The sample is uniformly glued onto the heat sink and therefore lies parallel to the sample holder. No wedge of GE varnish between aluminum socket and sample is visible. This was the set-up with no vertical temperature gradient in the sample. In figure 3.7 (b), a plastic support at the bottom end of the sample results in a hot spot at the bottom end and a cold spot at the top end. This was the set-up for generating a temperature gradient pointing from top to bottom (the temperature gradient will always be defined as pointing from cold to hot). In figure 3.7 (c), the support is placed at the top end of the sample, therefore resulting in a temperature gradient pointing upward (from bottom to top end of the sample). The temperature difference between cold and hot spot in the experiments under current flow was in the range of $1\,\mathrm{K}$ to $2\,\mathrm{K}$, which was inferred from temperature scans of different parts of the sample.
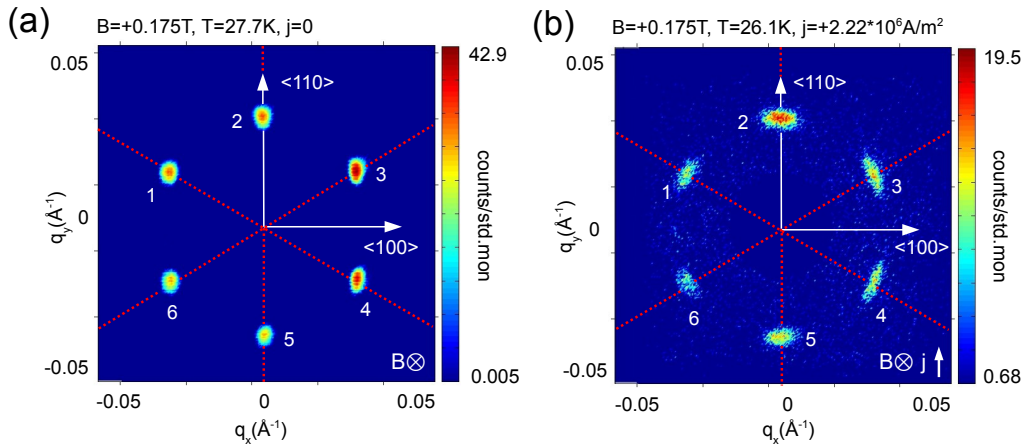
3.4.1 Absence of vertical temperature gradient

In the following, the results are presented that were obtained with sample (i) in the set-up with no forced vertical temperature gradient, as shown in figure 3.7 (a).

Figure 3.8 (a) shows the summed-up intensity over the scattering pictures of a tilting scan in the A-phase with no current through the sample. The peak shape is only determined by the instrument resolution.

Figure 3.8 (b) shows the scattering pattern in the A-phase when a current of $j = 2.22 \cdot 10^6\,\mathrm{A/m^2}$ is applied in positive direction. The picture was produced by subsequently rocking all six peaks into their Bragg condition and then summing up the diffraction pictures. The temperature had to be lowered to $26.1\,\mathrm{K}$ due to the ohmic heating shift to lower temperature of the A-phase. The intensity is much lower when current is applied (see the color bar on the right side of the pictures). Compared to (a), the diffraction peaks are azimuthally broadened but the azimuthal position of the peaks has not changed.
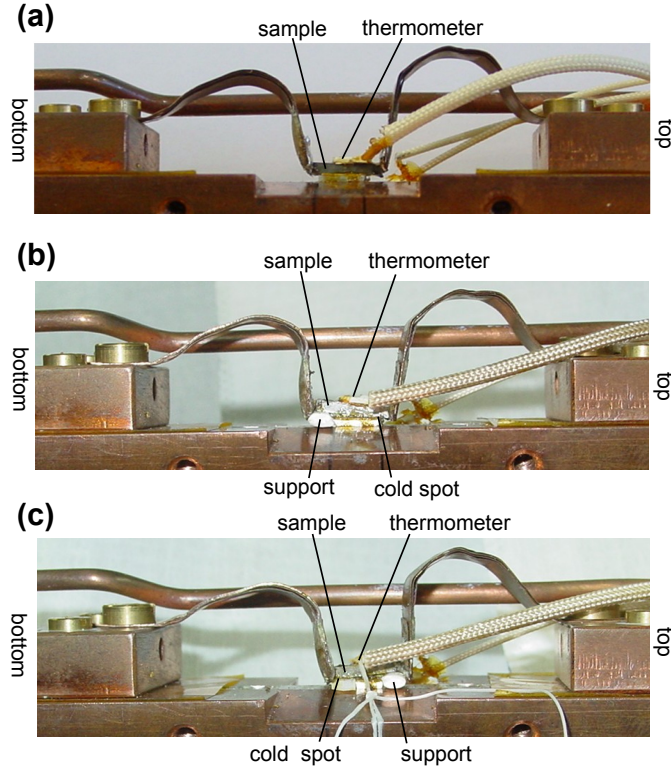
Figure 3.7: Temperature gradients in the sample. (a) Configuration without vertical temperature gradient. Sample firmly and uniformly attached to the heat sink. (b) Configuration for temperature gradient pointing from top to bottom. A small wedge of GE varnish underneath the sample is generated by the plastic support underneath the bottom sample end. (c) Configuration for temperature gradient pointing from bottom to top. Same procedure as in (b) but with the support placed at the top sample end.

Figure 3.8: Scattering patterns of the A-phase observed in the set-up with no forced vertical temperature gradient. (a) Scattering pattern (sum over a tilt scan) of the skyrmion lattice at zero current. (b) Scattering pattern of the skyrmion lattice with a current j in vertical direction. An azimuthal broadening of the peaks with respect to (a) is visible, the azimuthal positions of the peaks remain unchanged compared to (a).

Figure 3.9 shows a quantitative analysis of the diffraction pattern in figure 3.8 (a). The diagrams from (a) to (f) show the intensity of the peaks numbered from one to six according to the diffraction peaks in figure 3.8 (a). The intensity is plotted versus the azimuthal angle. The data were fitted by Gaussians (dashed lines). The

vertical blue dashed line is drawn through the center of the Gaussian curves. The peak centers are from (a) to (f): -61.9°, -1.2°, 60.0°, 121.0°, 180.0° and -121.4°. The difference between the peak centers is 60° within an error of less than 2°, thus confirming the hexagonal symmetry of the skyrmion lattice in the A-phase.
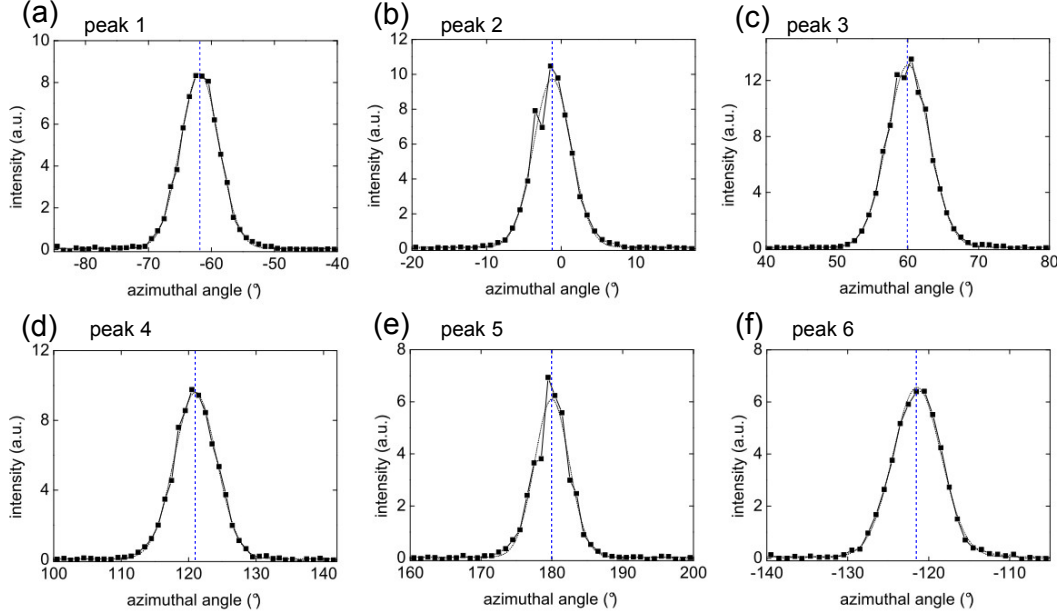
Figure 3.9: (a) to (f) Intensities of the six peaks in figure 3.8 (a) as a function of azimuthal angle. Data is fitted by Gaussians (dashed lines) and the peak centers are indicated by the dashed blue line.

Figure 3.10 shows the analysis of the diffraction pattern in figure 3.8 (b). The peak centers are from (a) to (f): -61.5°, -0.4°, 61.2°, 121.0°, 180.4° and -120.8°. The difference between the peak centers is 60° within an error of less than 2° and the peak centers coincide within this error with the peak centers of the zero current data in figure 3.9.
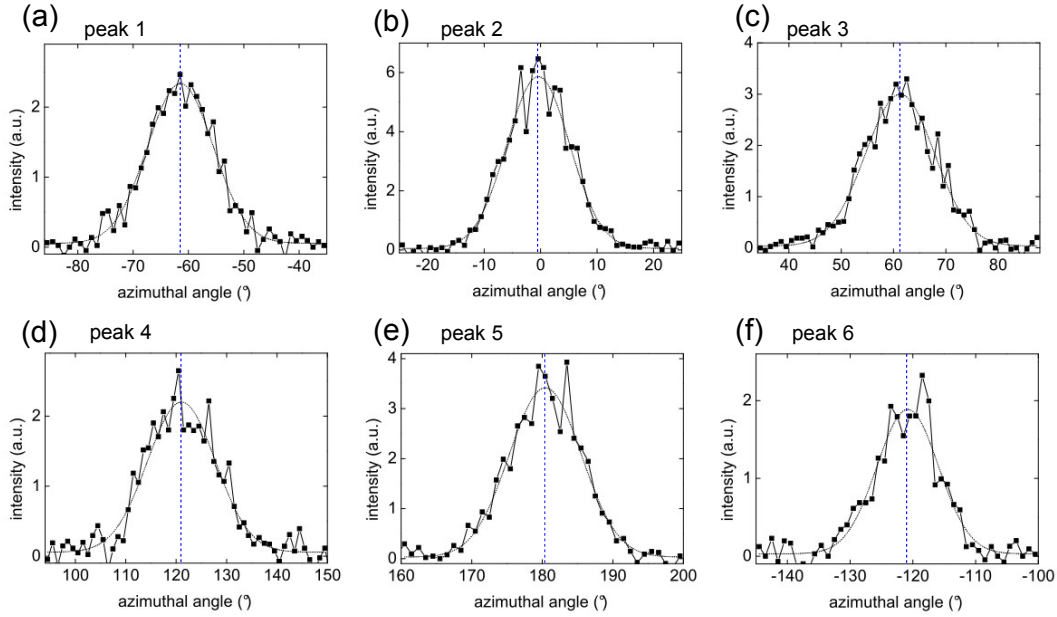
Figure 3.10: (a) to (f) Intensities of the six peaks in figure 3.8 (b) as a function of azimuthal angle. Data is fitted by Gaussians (dashed lines) and the peak centers are indicated by the dashed blue line.

3.4.2 Temperature gradient pointing downward

In the following, the results are presented that were obtained with sample (i) in the set-up with the vertical temperature gradient pointing downward, like shown in figure 3.7 (b).

Temperature scan

At first, a temperature scan over the A-phase was carried out. The magnetic field for examining the A-phase was kept constant at the value $B = 0.175\,\text{T}$. For the temperature scans, only the left and right spots where rocked into the Bragg condition and the summed intensity of both pictures was taken as the diffraction picture. Therefore, peaks on the vertical axis will remain weak in the temperature scans.

The vertical axis of the sample was a crystalline $\langle 110 \rangle$ axis, the horizontal axis perpendicular to the beam was a $\langle 100 \rangle$ axis and the beam direction was parallel to a $\langle 110 \rangle$ axis.

Figure 3.11 shows the resulting A-phase scattering intensity plotted against the temperature. The data for zero current through the sample is shown in green. The temperature interval of the A-phase is rather small. The step size of the temperature scan was $0.1\,\text{K}$.

The black data shows the scattering intensity when a current with density of $j = 2.22 \cdot 10^6\,\text{A/m}^2$ is sent through the sample in vertical direction from bottom to top, hence the positive sign in the legend. The step size of this temperature scan was $0.2\,\text{K}$. The data in red was taken at the same current value but opposite current

direction from top to bottom, hence the negative sign in the legend. The step size in this scan was 0.1 K.

The A-phase with current is shifted to lower temperatures. The scattering intensity with current is much smaller than at zero current. Furthermore, instead of a small temperature interval, a long tail in the intensity up to high temperatures can be seen.

The shift to lower temperatures of the A-phase with current is due to ohmic heating. The ohmic heat constantly generated in the sample by the current is carried out of the sample in the equilibrium state (constant temperature) by a temperature gradient between the interior of the sample and its surface. This means that the sample is hotter in its interior than at its surface, where the sample thermometer is fixed. Therefore, the temperature measured by the sample thermometer is lower than the temperature in the sample interior.

The smaller intensity with current is probably due to the same temperature gradients between sample interior and sample surface. The proportions of the sample having the same temperatures get smaller. Therefore, various parts of the sample that are at different temperatures contribute to the scattering signal. Due to the small temperature interval where the A-phase is stable, only a part of the sample is at temperatures within the A-phase, whereas other parts of the sample can have temperatures already outside of the A-phase. Therefore, the scattering intensity in the A-phase is reduced with current.

The long tail of scattering intensity up to increasing temperatures when current is applied is very likely also due to the effect of temperature gradients because under the assumption of a gradient, even when the main body of the sample is already at high temperatures outside of the A-phase, there can still be small parts of the sample at lower temperatures within the A-phase, delivering a small scattering signal.
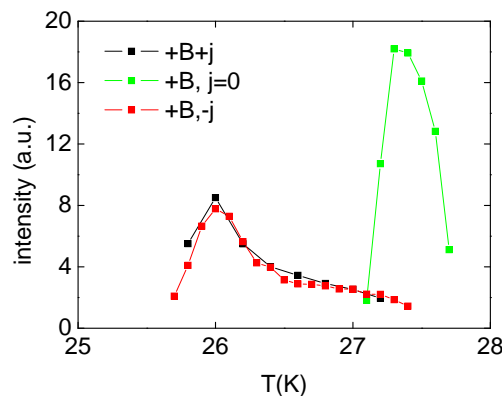
Figure 3.11: Scattering intensity of the A-phase as a function of temperature. Data at zero current is shown in green. Data at positive current is shown in black, data at negative current is shown in red. The zero current data shows an A-phase with a small temperature range. The data with current is shifted to lower temperature due to ohmic heating and exhibits a long intensity tail at high temperatures.

Figure 3.12 (a) on the left shows one of the scattering patterns taken in the tempera-

ture scan of the A-phase at positive current direction. Vertical temperature gradient, magnetic field direction and current direction are indicated on all the scattering pictures of figure 3.12. The temperature where this scattering picture was taken was 25.8 K, which is (see figure 3.11) slightly below the temperature of maximal intensity in the A-phase.

Figure 3.12 (a) on the right shows a scattering picture of the same temperature scan but at a higher temperature, at 27.2 K. This is (see figure 3.11) at high temperature in the intensity tail. The whole scattering pattern has been rotated anti clockwise when compared to the scattering picture at low temperature on the left. The red dashed lines to guide the eye are the same lines as on the left scattering picture in order to make the rotation easily visible.

Figure 3.12 (b) shows the same procedure as in (a), but with the temperature scan at zero current. The temperature of the left scattering pattern is 27.2 K, which is (see figure 3.11) at a temperature slightly below the temperature where the A-phase has maximal intensity.

The right diffraction pattern in (b) was taken at a higher temperature of 27.7 K, which is (see figure 3.11) the highest temperature of the scan. In contrast to (a), the angular positions of the peaks have not changed with temperature.

Figure 3.12 (c) shows the same procedure as in (a) and (b) for the temperature scan with negative current direction. The left picture shows the diffraction pattern at 25.9 K, which is (see figure 3.11) at slightly lower temperature than the temperature of maximal A-phase signal. The scattering pattern is not different from the corresponding scattering pattern with positive current direction in (a).

At a higher temperature of 27.3 K, which is (see figure 3.11) in the intensity tail at high temperatures, the whole rotation pattern has rotated in a clockwise direction, just the opposite rotational sense as in (a).

So, in short, we see temperature-dependent rotations in the temperature scans of the A-phase when a current is sent through the sample. The rotations are dependent on the current direction. Without current no rotations are observed.

Figure 3.13 shows the temperature scan for the positive current direction. In each diagram, the intensity is plotted versus the azimuthal angle along the ring for one temperature of the temperature scan. Only the peak 2 at approximately 60° angular position is shown. The angular scale is the same in each diagram. The blue dashed line shows the angular position of the peak maximum at 25.8 K, the lowest temperature. In each panel, the data is fitted by a Gaussian. The resulting peak center of the fit, which is the azimuthal position of the peak, and the integrated intensity A are given on top left in each diagram.

The integrated intensity A increases at first, reaching the maximum at 26.0 K and then it falls continuously (compare also to figure 3.11). The peak center decreases continuously in angular position with increasing temperature, which is equivalent to an anti clockwise rotation, as was already suggested in figure 3.12 (a). With the help of the dashed blue line, the shift of the peak to lower azimuthal angles with
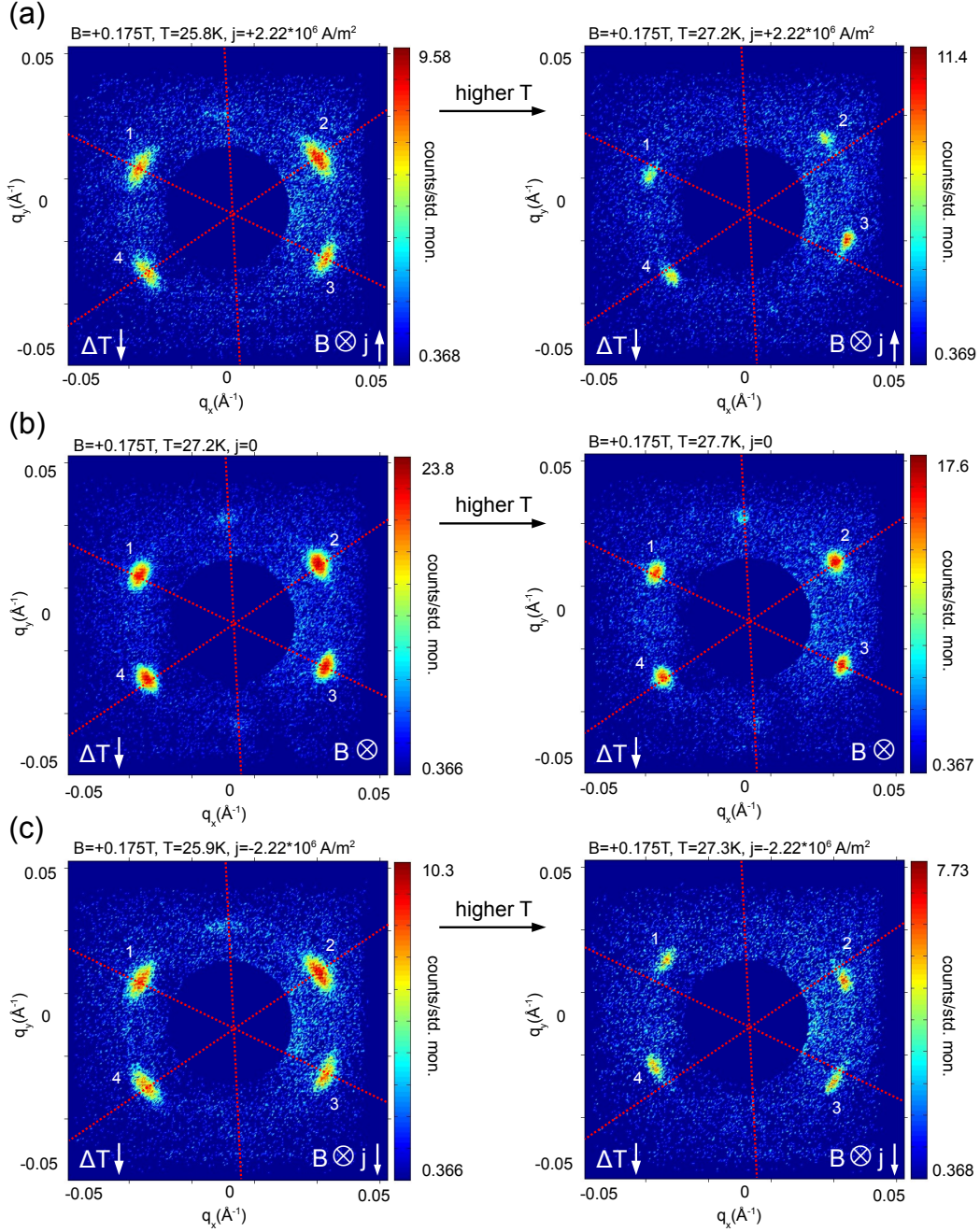
Figure 3.12: Some scattering patterns of the temperature scans of the A-phase. Left column: Scattering pictures at low temperatures of the temperature scan. Right column: Scattering pictures at high temperature in the intensity tail. (a) Data at positive current. The diffraction pattern has rotated in anti clockwise direction at the high temperature. (b) Data at zero current. The diffraction pattern has not changed in respect of the azimuthal angles at high temperature. (c) Data at negative current. The scattering pattern rotates clockwise at high temperatures.

increasing temperature is clearly visible.

The temperature-dependent azimuthal displacement of the peaks is shown in figure 3.14. Here, the azimuthal angle determined by the peak center of the Gaussian fits is plotted versus the temperature for all three temperature scans. The azimuthal position shown here is the average position of the four peaks. The data indicate
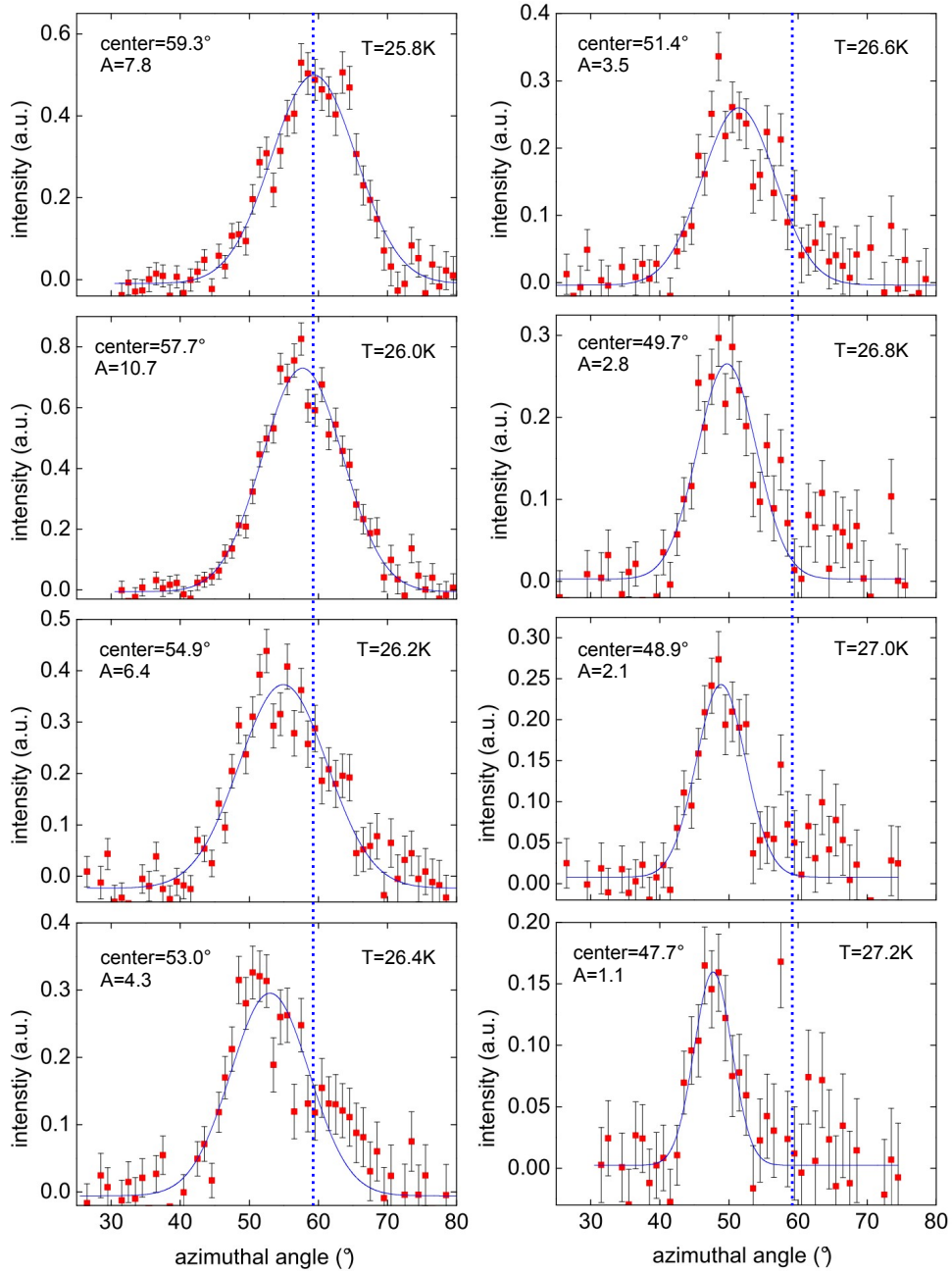
Figure 3.13: Scattering intensity plotted versus the azimuthal angle for peak 2 (see figure 3.12) for the temperature scan with positive current direction. Each diagram is at one temperature of the temperature scan. The data is fitted by a Gaussian. The peak center obtained from the fits and the integrated intensity A below the Gaussians is given on top left on each diagram. The dashed blue line is drawn through the peak center at the lowest temperature (25.8 K). The shift of the peak center to the left, which indicates an anti clockwise rotation with increasing temperature, is clearly visible.

the anti clockwise rotation for the positive current (black data), the non existent rotation for zero current (green data) and the clockwise rotation for the negative current direction (red data).
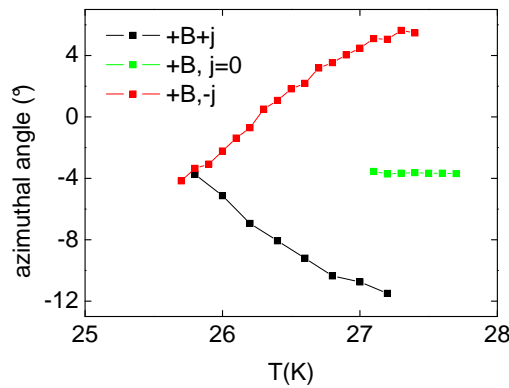
Figure 3.14: The azimuthal angles of the temperature scan averaged over the four diffraction peaks are plotted versus the temperature. The data at zero current shows no slope and therefore no temperature-dependent rotation. The black data (positive current) shows the anti clockwise rotation and the red data (negative current) shows the clockwise rotation with increasing temperature.

Directional dependence of rotation

In the next step, we set a temperature at which we could see a large rotation of the scattering pattern in the temperature scans above. At this temperature and the same absolute value of current density $j = 2.22 \cdot 10^6 \, \text{A/m}^2$, scattering patterns were taken at the four possible combinations of direction of magnetic field and current direction, allowing them to be positive or negative. Figure 3.15 shows the resulting four scattering pictures. A temperature of $26.8 \, \text{K}$ was chosen, which ensures a visible rotation, which is verified by looking at figure 3.13 and figure 3.14.

Figure 3.15 (a) shows the diffraction pattern at the combination with positive magnetic field and positive current direction. The picture was obtained by rotating and tilting the sample into the Bragg angles for the six spots and then summing up the intensity. Therefore, all six spots are visible at high intensity.

The scattering pattern is turned in anti clockwise direction with respect to the crystal directions. The scattering pattern in figure 3.15 (b) has rotated in clockwise direction with respect to the crystalline axes. The only difference between (a) and (b) is the current direction. Figure 3.15 (c) shows the diffraction pattern with both magnetic field and current direction negative. The peaks rotate back to the positions of (a). Figure 3.15 (d) shows the diffraction picture for the combination with negative magnetic field direction but positive current. The rotational sense of the scattering pattern is the same as in (b).

In short, when only one of the directions, magnetic field direction or current direction, is negative, we have a clockwise rotation of the scattering pattern and when both directions are positive or both are negative, we have an anti clockwise rotation.

In order to make the rotations better visible, we made difference pictures of the intensity between the diffraction pictures of different combinations in figure 3.15. Figure 3.16 (a) shows the difference picture where the diffraction pattern figure 3.15
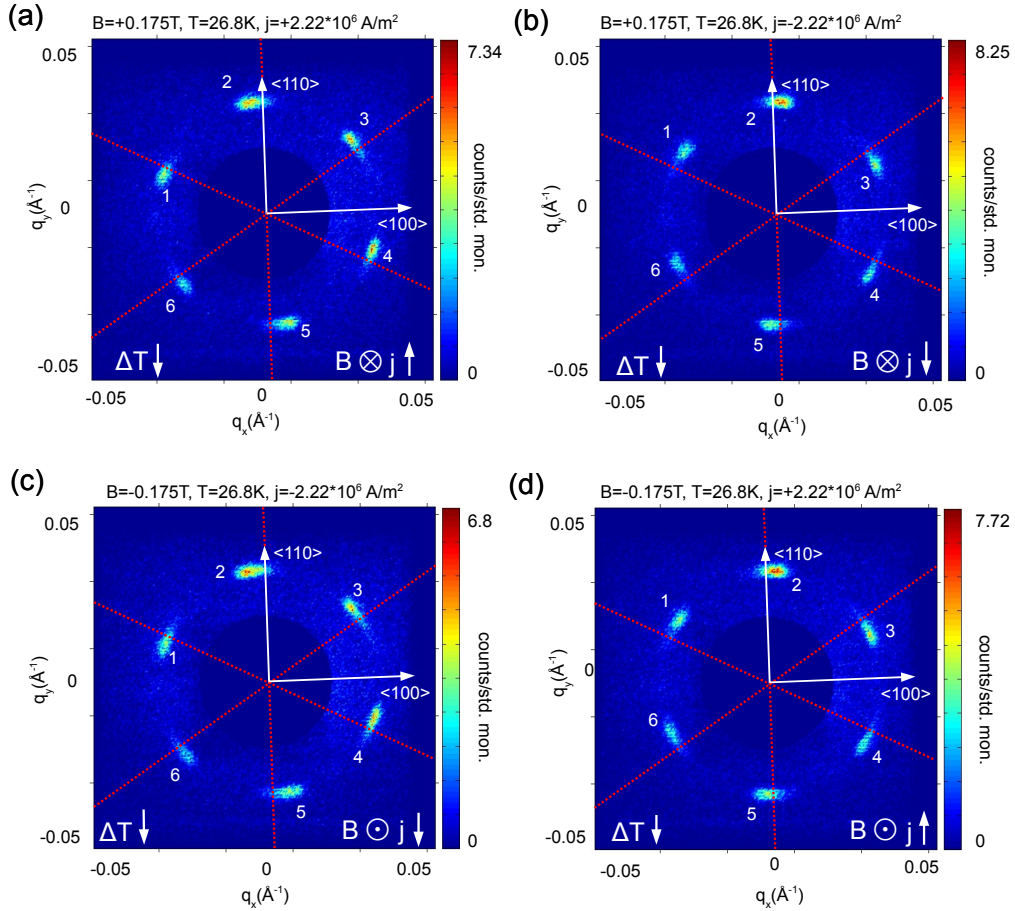
Figure 3.15: Diffraction patterns taken at a high temperature of 26.8 K in the intensity tail of the temperature scans at the four different combinations of magnetic field direction and current direction. (a) Combination with magnetic field and current direction both positive. The scattering pattern is rotated anti clockwise with respect to the crystalline orientation. (b) Current direction negative, magnetic field positive. Scattering pattern is rotated clockwise. (c) Both magnetic field and current direction negative. Rotation is the same as in (a). (d) Magnetic field direction negative, current direction positive. Rotation is the same as in (b).

(b) was subtracted from figure 3.15 (a). The clockwise rotation of the scattering pattern at negative current direction in figure 3.15 (b) is easily recognizable. Which combination of current and magnetic field direction is subtracted from which one is indicated at the top left of the pictures.

Figure 3.16 (b) shows that the combination with magnetic field and current both negative coincides with the combination where both are positive, because the intensity is nearly zero everywhere in the picture. Figure 3.16 (c) is nearly identical to figure 3.16 (a), which means that for the rotation it does not matter whether the current is negative, like in (a), or the magnetic field, like in (c). Figure 3.16 (d) shows, like in (b), zero intensity in the whole picture. This enforces what is already said above, that for the rotation it does not matter whether the current is negative or the magnetic field.

Figure 3.17 shows a quantitative analysis of the diffraction pictures in figure 3.15. The diagrams from (a) to (f) display the intensity of the peaks numbered from
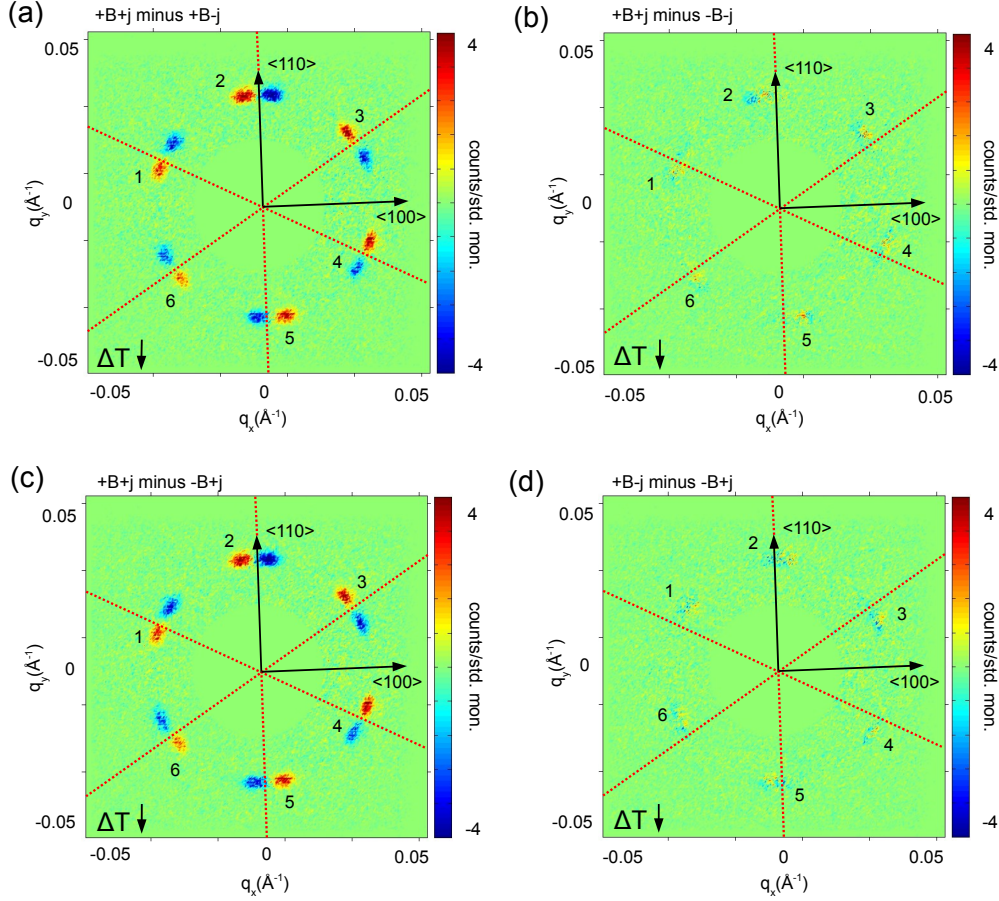
Figure 3.16: Differences of the scattering pictures in figure 3.15. The subtraction is indicated on top left of each picture. (a) Picture with negative current is subtracted from picture with both magnetic field and current direction positive. The clockwise rotation is visible. (b) Picture with both directions negative is subtracted from picture with both positive. No rotation is visible. (c) Picture with negative magnetic field is subtracted from picture with both directions positive. Same rotation as in (a). (d) Picture with negative magnetic field is subtracted from picture with negative current. Like in (b), no rotation is visible.

one to six according to the diffraction peaks in figure 3.15. The intensity is plotted versus the azimuthal angle. The data for the combination where both magnetic field direction and current direction are positive (see figure 3.15 (a)) is shown in black. The data for the combination with positive magnetic field and negative current direction (see figure 3.15 (b)) is shown in red.

The clockwise rotation at negative current direction (figure 3.15 (b)) with respect to positive current direction is seen by the fact that the data in red is shifted to higher azimuthal angles. The data were fitted by Gaussians (dashed lines). The vertical blue dashed line is drawn through the center of the Gaussian curves. The difference in azimuthal position of the peak centers between the black and the red curves, which determines the rotation, is called $\Delta\Phi$.

The difference in azimuthal angle $\Delta\Phi$ is from (a) to (f): 13.3°, 10.2°, 13.7°, 12.2°, 11.0° and 11.6°. The mean difference averaged over all peaks is 12.0°. The peak centers of the black curve for positive current are from (a) to (f): -68.9°, -8.1°, 49.0°,

109.4°, 170.6° and -129.0°. The difference between the peak centers is 60° within an error of at most 3°, thus confirming the hexagonal symmetry of the skyrmion lattice in the A-phase.
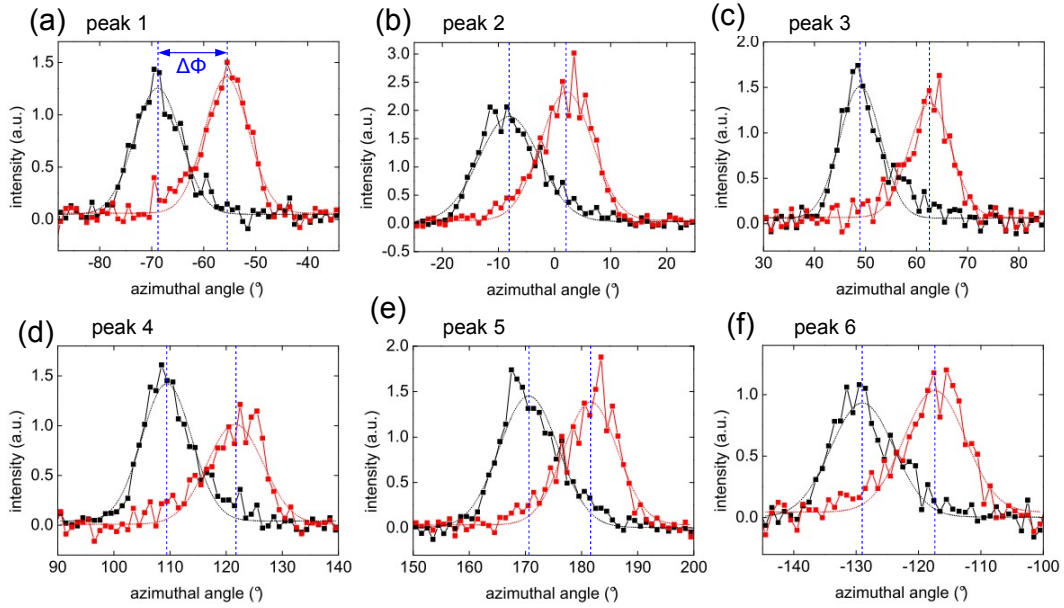
Figure 3.17: Analysis of scattering pictures in figure 3.15. From (a) to (f) the intensity is plotted against the azimuthal angle for each of the six peaks. Data is fitted by Gaussians (dashed black and red line). The peak center of the Gaussians is indicated by the dashed blue line. The black data is at positive magnetic field and positive current. The red data is at positive magnetic field and negative current direction. $\Delta\Phi$ is the rotation.

3.4.3 Temperature gradient pointing upward

In the next step, the direction of the temperature gradient was reversed. The results that are presented in the following were obtained with sample (i) in the set-up shown in figure 3.7 (c). The current density remained at the value $j = 2.22 \cdot 10^6 \, \text{A/m}^2$.

Temperature scan

At first, temperate scans over the A-phase were carried out like in figure 3.11 (where the temperature gradient pointed in the opposite direction). Figure 3.18 shows the analogous picture to figure 3.11.

The temperatures of the A-phase are higher than in figure 3.11. This is due to a slightly changed experimental set-up involving exchange gas and soldered contacts of the sample. The intensity tail to high temperatures is also seen here. The same reasons as in figure 3.11 can be applied here to explain the tail of intensity. The temperature gradient leads to the situation that some parts of the sample are still in the A-phase when other parts have already left the A-phase.
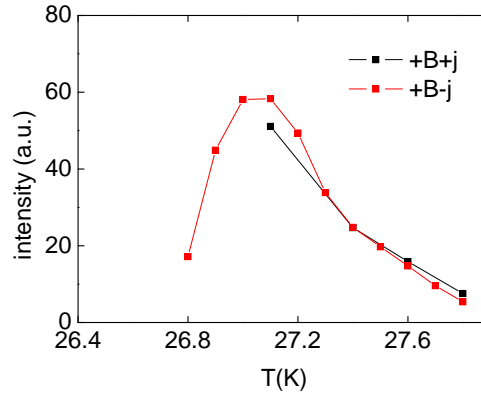
Figure 3.18: Scattering intensity of the A-phase as a function of temperature. The data with positive current is shown in black, the data with negative current is shown in red. At both current directions, a long intensity tail at high temperatures is observed.

Figure 3.19 (a) on the left shows one of the scattering patterns taken in the temperature scan of the A-phase at positive current direction. The temperature where this scattering picture was taken was $27.1\,K$, which is (see figure 3.18) the temperature of maximal intensity of the A-phase.

Figure 3.19 (a) on the right hand side shows a scattering picture of the same temperature scan but at a higher temperature, at $27.8\,K$. This is (see figure 3.18) at high temperature in the intensity tail. Clearly, the whole scattering pattern has rotated clockwise.

Figure 3.19 (b) shows the same procedure as in (a) for the temperature scan with negative current direction. The left picture shows the diffraction pattern at $26.9\,K$, which is (see figure 3.18) at slightly lower temperature than the temperature where the A-phase signal is maximal. The scattering pattern shows no difference to the one in (a).

At a higher temperature of $27.6\,K$, which is (see figure 3.18) in the intensity tail at high temperatures, the whole rotation pattern has rotated in anti clockwise direction, just the opposite rotational sense as in (a).

The rotations in figure 3.19 have the opposite sense of the rotations in figure 3.12. The difference between these two figures is the direction of the vertical temperature gradient, which suggests its decisive role in explaining the rotations.

The temperature dependent azimuthal displacement of the peaks (the mean azimuthal position of the four peaks) is displayed in figure 3.20. Like in figure 3.14, the slopes of the temperature-dependent rotation for the positive and the negative current have different signs. As the rotational senses are opposite to each other, the black and red data are swapped between figure 3.14 and figure 3.20.
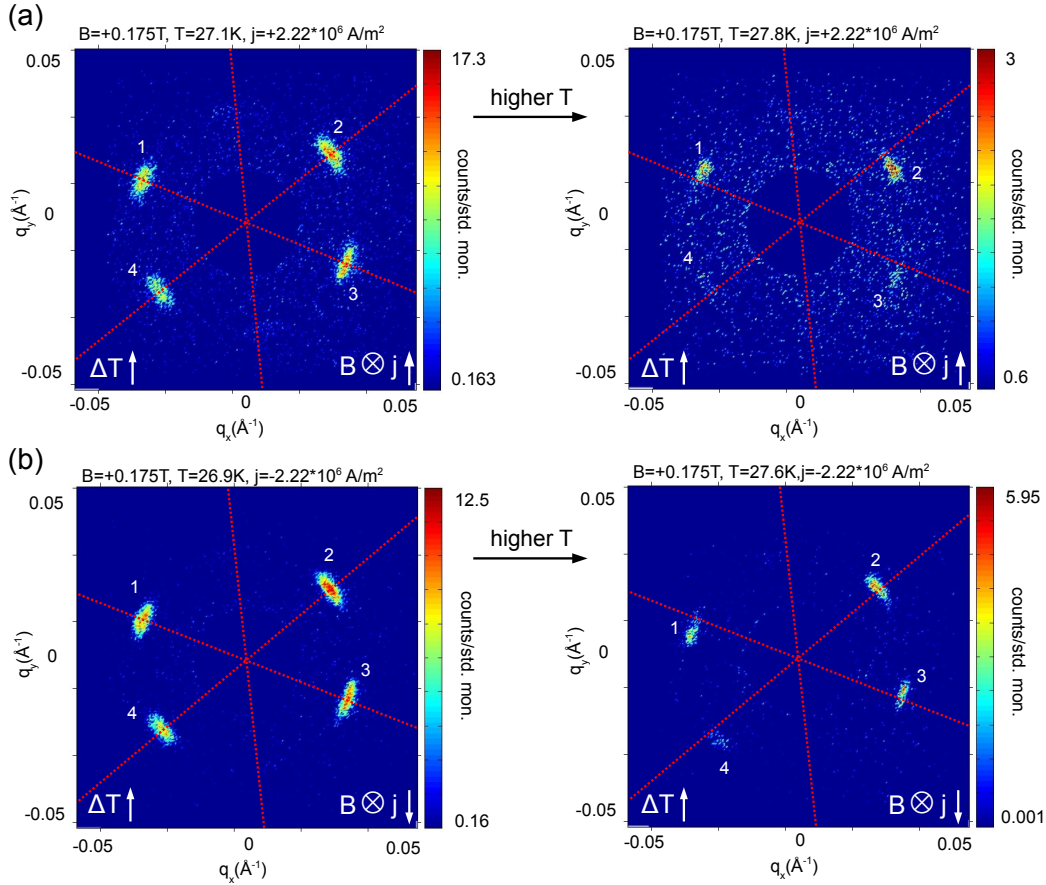
Figure 3.19: Some scattering patterns of the temperature scans of the A-phase. Left column: Scattering pictures at low temperatures of the temperature scan. Right column: Scattering pictures at high temperature in the intensity tail. (a) Data at positive current. The diffraction pattern has rotated in clockwise direction at the high temperature. (b) Data at negative current. The scattering pattern rotates anti clockwise at high temperatures.
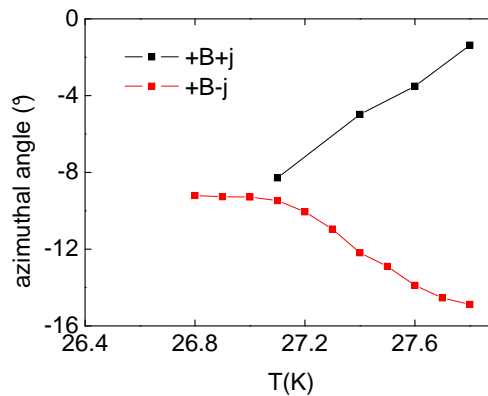
Figure 3.20: The azimuthal angles of the temperature scan averaged over the four diffraction peaks are plotted versus the temperature. The black data (positive current) shows the clockwise rotation and the red data (negative current) shows the anti clockwise rotation with increasing temperature.

Directional dependence of rotation

In the next step, we set a temperature at which we could see a large rotation of the scattering pattern in the temperature scans. At this temperature and the same

absolute value of current density $j = 2.22 \cdot 10^6$ A/m^2, scattering patterns were taken in the four possible combinations of direction of magnetic field and current direction, see figure 3.21. A temperature of 27.8 K was chosen, which ensures a visible rotation (see figure 3.20). This is the same procedure as in figure 3.15 (where the temperature gradient pointed in the opposite direction).

In short, we have the same situation like in figure 3.15: The rotational sense when only one of the directions, magnetic field direction or current direction, is negative, is opposite to the rotational sense when both directions are positive or both directions are negative. The rotational sense is opposite to the one in figure 3.15.
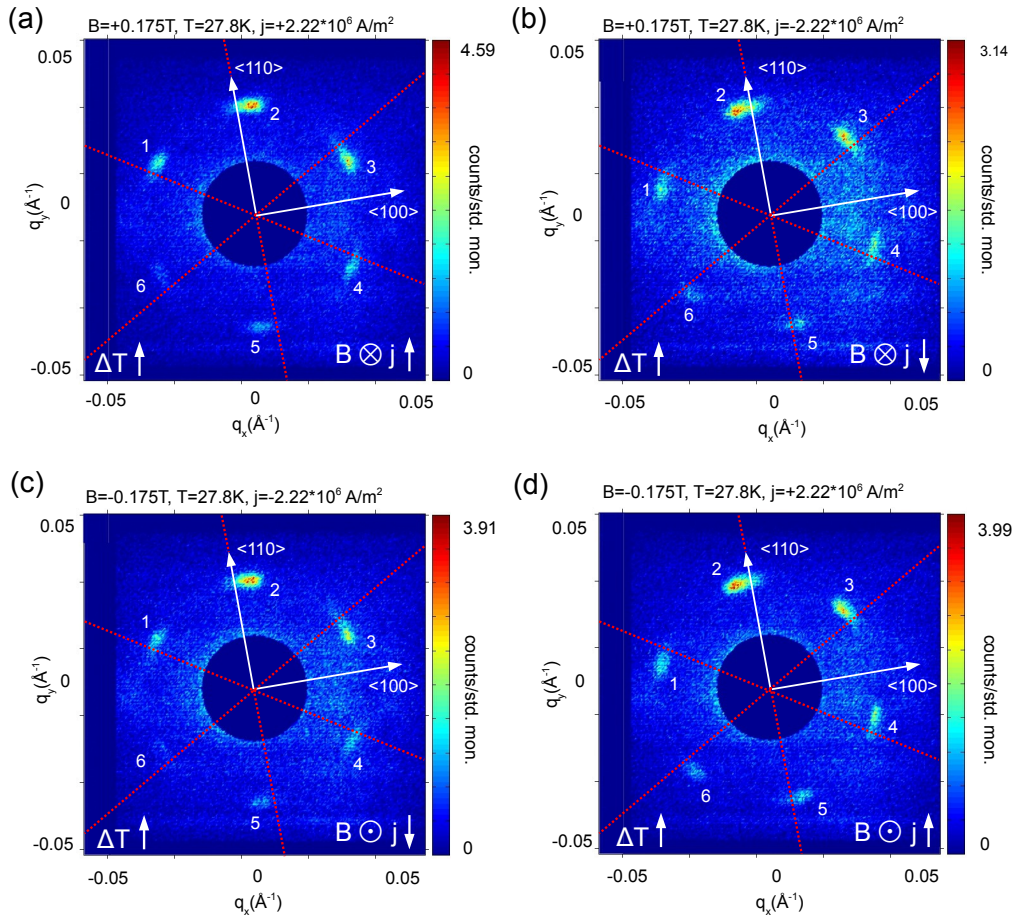
Figure 3.21: Diffraction patterns taken at a high temperature of 27.8 K in the intensity tail of the temperature scans at the four different combinations of magnetic field direction and current direction. (a) Combination with magnetic field and current direction both positive. The scattering pattern is rotated clockwise. (b) Negative current direction, positive magnetic field. Scattering pattern has rotated anti clockwise. (c) Both magnetic field and current direction negative. Rotation is the same as in (a). (d) Magnetic field direction negative, current is positive. Rotation is the same as in (b).

Figure 3.22 is the analogous picture to figure 3.16 (where the temperature gradient pointed in the opposite direction). Compared with figure 3.16, the rotational sense has reversed.

Figure 3.23 shows the quantitative analysis of the diffraction pictures in figure 3.21. It is the analogous picture to 3.17 (where the temperature gradient pointed in the
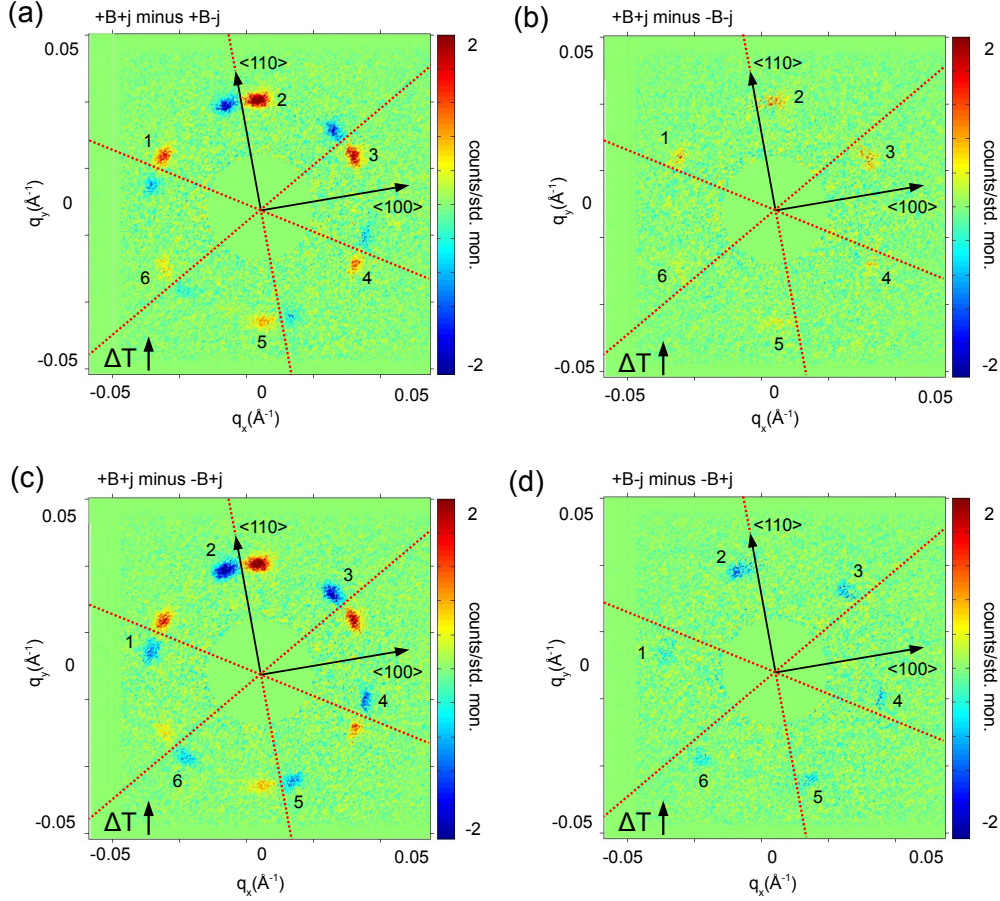
Figure 3.22: Differences of the scattering pictures in 3.21. The subtraction is indicated on top left of each picture. (a) Picture with negative current is subtracted from picture with both magnetic field and current direction positive. The anti clockwise rotation is visible. (b) Picture with both directions negative is subtracted from picture with both positive. No rotation is visible. (c) Picture with negative magnetic field is subtracted from picture with both directions positive. Same rotation as in (a). (d) Picture with negative magnetic field is subtracted from picture with negative current. Like in (b), no rotation is visible.

opposite direction). The data for the combination with both magnetic field direction and current direction positive (see figure 3.21 (a)) is shown in black. The data for the combination with positive magnetic field and negative current direction (see figure 3.21 (b)) is shown in red.

The anti clockwise rotation at negative current direction (figure 3.21 (b)) with respect to positive current direction is seen by the fact that the red data is shifted to smaller azimuthal angles. The data were fitted by Gaussians (dashed lines). The vertical blue dashed line is drawn through the center of the Gaussian curves. The difference in azimuthal position of the peak centers, which determines the rotation, is called $\Delta\Phi$.

The difference in azimuthal angle $\Delta\Phi$ is from (a) to (f): 12.8°, 12.1°, 15.2°, 10.8°, 10.6° and 14.1°. The mean difference averaged over all peaks is 12.6°. The peak centers of the black curve for positive current are from (a) to (f): -63.7°, -2.5°, 60.4°, 117.0°, 177.3° and -121.4°. The difference between the peak centers is 60° within an

error of at most 4°.
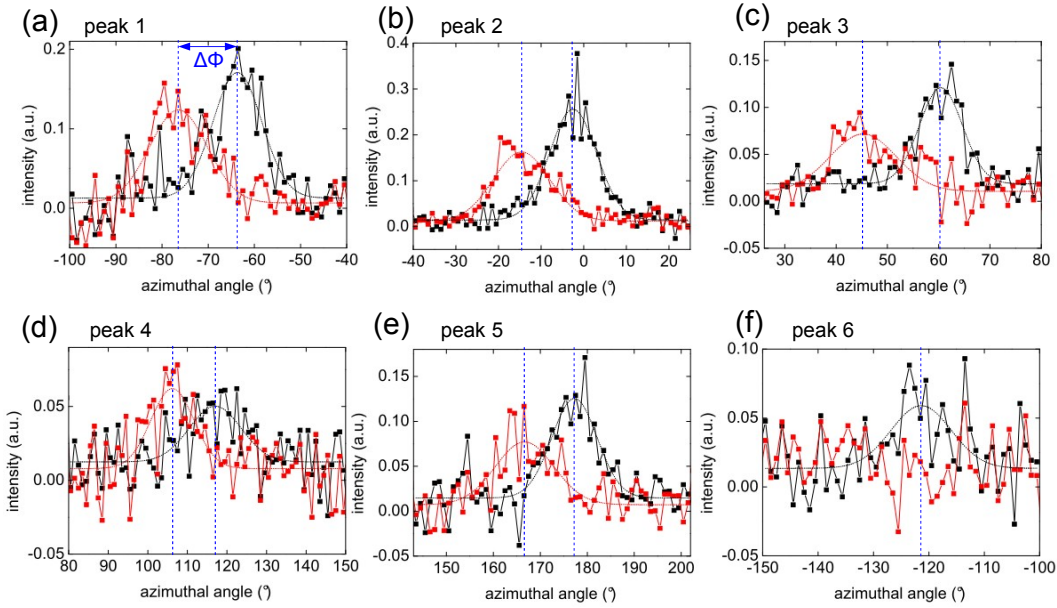
Figure 3.23: Analysis of scattering pictures in figure 3.21. From (a) to (f) the intensity is plotted against the azimuthal angle for each of the six peaks. Data is fitted by Gaussians (dashed black and red line). The peak center of the Gaussians is indicated by the dashed blue line. The black data is at positive magnetic field and positive current. The red data is at positive magnetic field and negative current direction. $\Delta\Phi$ is the rotation.

3.4.4   Scan of current density

An important question is how the rotations that we saw above depend on the current density. Therefore, a current scan was carried out. A temperature within the A-phase was kept constant and the current was driven from negative to positive values. At each step size of current, a diffraction picture was taken. The observed effects were not hysteretic in current.

The current scans were done at three different temperatures within the A-phase, at $26.8\,\mathrm{K}$, at $27.2\,\mathrm{K}$ and at $27.4\,\mathrm{K}$. As can be seen in figure 3.24, only the left-sided peaks and the right-sided peaks were rocked into the Bragg condition. Therefore, the peaks on the vertical axis are very weak. The experimental set-up is displayed in figure 3.7(b), with the temperature gradient pointing downward. The magnetic field was always positive.

Figure 3.24 (a) shows three scattering pictures of the scan at $26.8\,\mathrm{K}$. The left picture is taken at the most negative current density $j = -2.22\cdot10^6\,\mathrm{A/m^2}$, the picture in the center is taken at the smallest current density near zero, here $j = +0.89\cdot10^6\,\mathrm{A/m^2}$, and the right picture is taken at the highest positive current density $j = +2.22\cdot 10^6\,\mathrm{A/m^2}$. In (a), there is no data at zero current density, because at a temperature of $26.8\,\mathrm{K}$ no A-phase signal is seen at zero current.

The diffraction spots on the left in (a) are rotated clockwise while the spots on the

right are rotated anti clockwise. These rotations match the rotations in figure 3.15.

Figure 3.24 (b) shows the corresponding pictures at the temperature 27.2 K, and figure 3.24 (c) shows the pictures at 27.4 K. In (b) and (c), the current in the central picture is zero. The rotation pattern in (b) and (c) is the same as in (a).
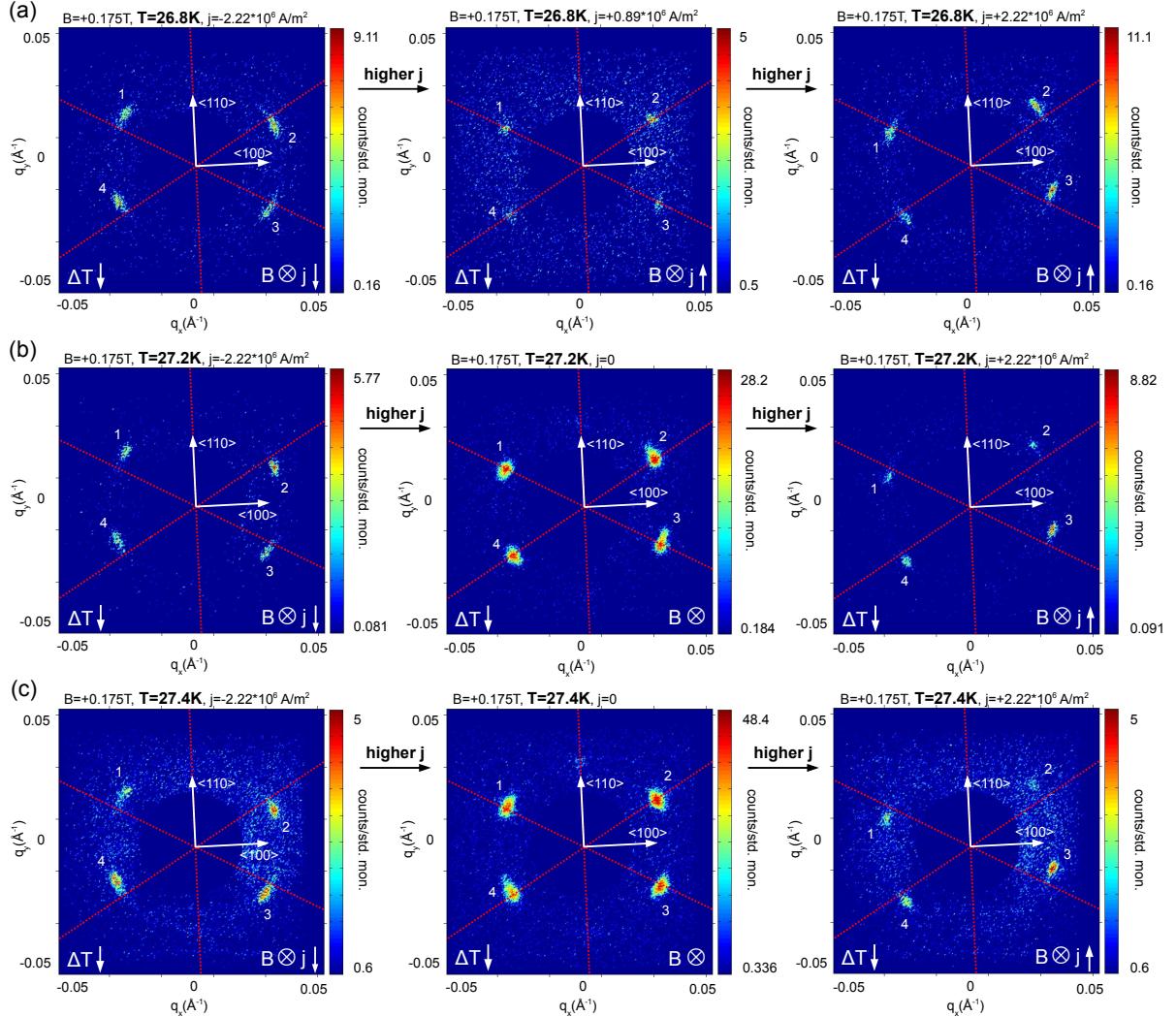
Figure 3.24: Some scattering pictures of the electric current scan of the A-phase at 26.8 K in (a), at 27.2 K in (b) and at 27.4 K in (c). Left column: Scattering picture at the most negative current density. Center column: Scattering picture at zero current (except in (a) where the value for the current is the lowest used in that scan). Right column: Scattering picture at the most positive current. The anti clockwise rotation with increasing current density is clearly visible in (a), (b) and (c).

Figure 3.25 presents the quantitative analysis of the current scans. The data from the scan at 26.8 K is shown in black, the data from the scan at 27.2 K is shown in red, and the data at 27.4 K is shown in green. The intensity of all the diffraction pictures of the three scans was plotted versus the azimuthal angle (procedure described in figure 3.5) and each peak was fitted with a Gaussian. The diagrams (a), (b) and (d) show the parameters obtained from the fits plotted against the current densities of the scan. Here, the displayed parameters are the averages over the four peaks in each scattering picture.

Figure 3.25 (a) displays the azimuthal position Φ. Higher values of this parameter signify clockwise rotation, lower values signify anti clockwise rotation. There is a threshold current density of approximately $j_c = \pm 1 \cdot 10^6 \, \text{A/m}^2$ where the rotation starts.

Figure 3.25 (b) displays the intensities. At the temperature of $26.8 \, \text{K}$ (black data), the intensity rises with increasing current due to the effect that the current heats up the sample interior into the A-phase, i.e. there is a temperature gradient between the cooler sample surface and the hotter sample interior. At higher current values, the intensity drops again because the current heats the sample interior beyond the A-phase temperatures. At $27.2 \, \text{K}$, the same effect occurs, but already at lower currents because the sample is already in the A-phase at zero current. At $27.4 \, \text{K}$, the sample is obviously in the maximum of the A-phase at zero current. Rising currents heat the sample interior beyond the A-phase temperatures, reducing the intensity.

Figure 3.25 (c) displays the temperature difference ΔT between the sample thermometer on the sample surface (which is also the control thermometer and is kept at constant temperature throughout the current scans) and the thermometer placed on the sample holder as a function of current density. A smooth quadratic increase with current density independent of the direction of the current is seen in contrast to the pronounced threshold in (a). The quadratic rise of ΔT means that in order to maintain the controlling sample thermometer at the constant value when the current and ohmic heat generated in the sample interior are rising, the system cools down the sample holder, therefore creating a temperature gradient so that the ohmic heat can be transported out of the sample.

Figure 3.25 (d) displays the azimuthal width $\Delta\Phi$ as a function of current density. Especially the data at the low temperatures $26.8 \, \text{K}$ and $27.2 \, \text{K}$ indicate the same threshold value of current density $j_c = \pm 1 \cdot 10^6 \, \text{A/m}^2$ as in (a) where the azimuthal broadening starts.

(a)

(b)

(c)

(d)
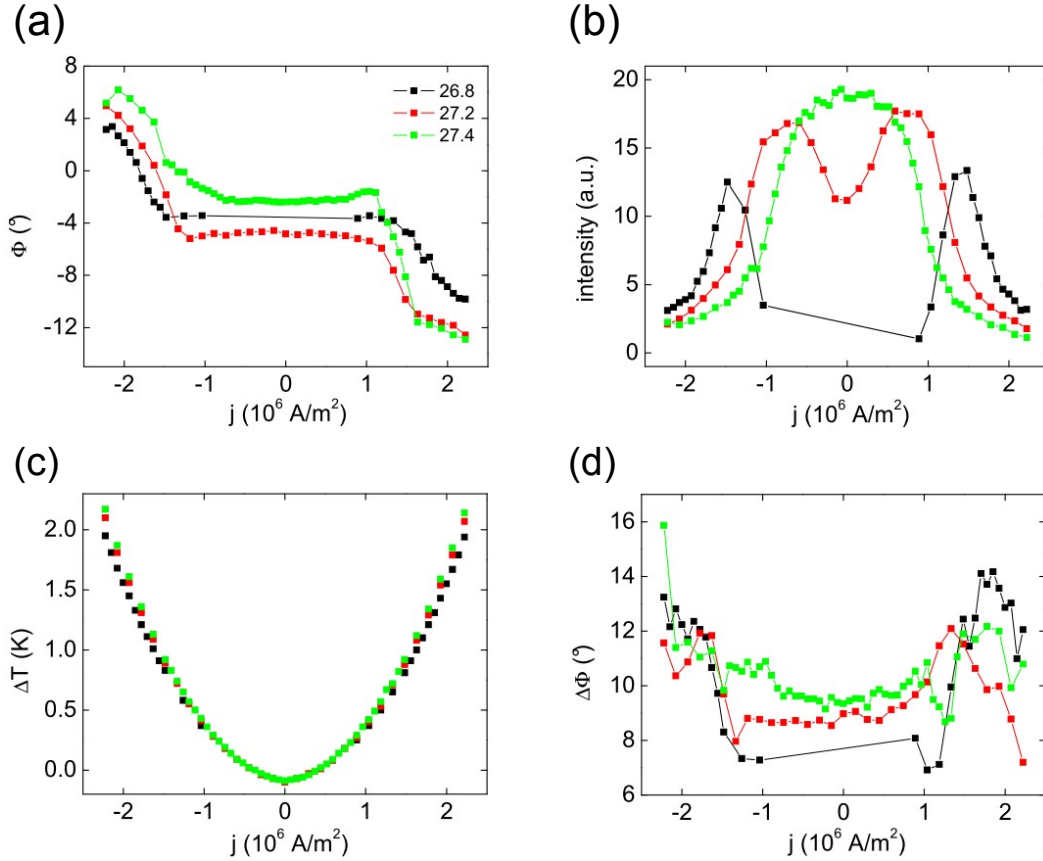
Figure 3.25: Analysis of the electric current scan. (a) Averaged azimuthal position plotted versus current density. The rotation starts at a threshold of about $j_c = \pm 1 \cdot 10^6 \, \text{A/m}^2$. (b) Averaged scattering intensity versus current density. The data demonstrates the effect of ohmic heating and the resulting temperature gradient between sample interior and sample surface (see text). (c) The temperature difference between sample surface and sample holder shows a smooth quadratic increase independent of current direction. (d) Averaged azimuthal width plotted versus the current density. The azimuthal broadening starts at the same threshold value of current density as in (a).

3.4.5   Other crystalline directions and sample shapes

Sample turned away from crystalline orientation

Sample (i) was also studied in other crystalline orientations. For example, the crystal was rotated around the vertical axis by approximately 20° in clockwise direction away from the crystalline orientation. The current is therefore still parallel to the vertical crystalline $\langle 110 \rangle$ axis but there is no particular crystalline orientation of the sample with respect to the magnetic field and neutron beam. Figure 3.26 presents the scattering pictures of the A-phase at zero current (a), at positive magnetic field and positive current in (b) and at the combination of positive magnetic field and negative current direction in (c). The set-up with temperature gradient pointing downward (figure 3.7 (b)) was chosen.

The temperature in figure 3.26 (a) is 27.7 K, which is right in the center of the A-phase. When applying a current $j = 2.22 \cdot 10^6 \, \text{A/m}^2$ through the sample in (b) and

(c), the temperature had to be reduced to 27.5 K due to the ohmic heating shift of the A-phase. At positive current and magnetic field in (b), the scattering pattern is rotated in anti clockwise direction. At negative current in (c), the scattering pattern rotates clockwise. This is the same rotational behavior as in figure 3.15. The data suggest therefore that the rotational behavior is independent of the crystalline orientation.
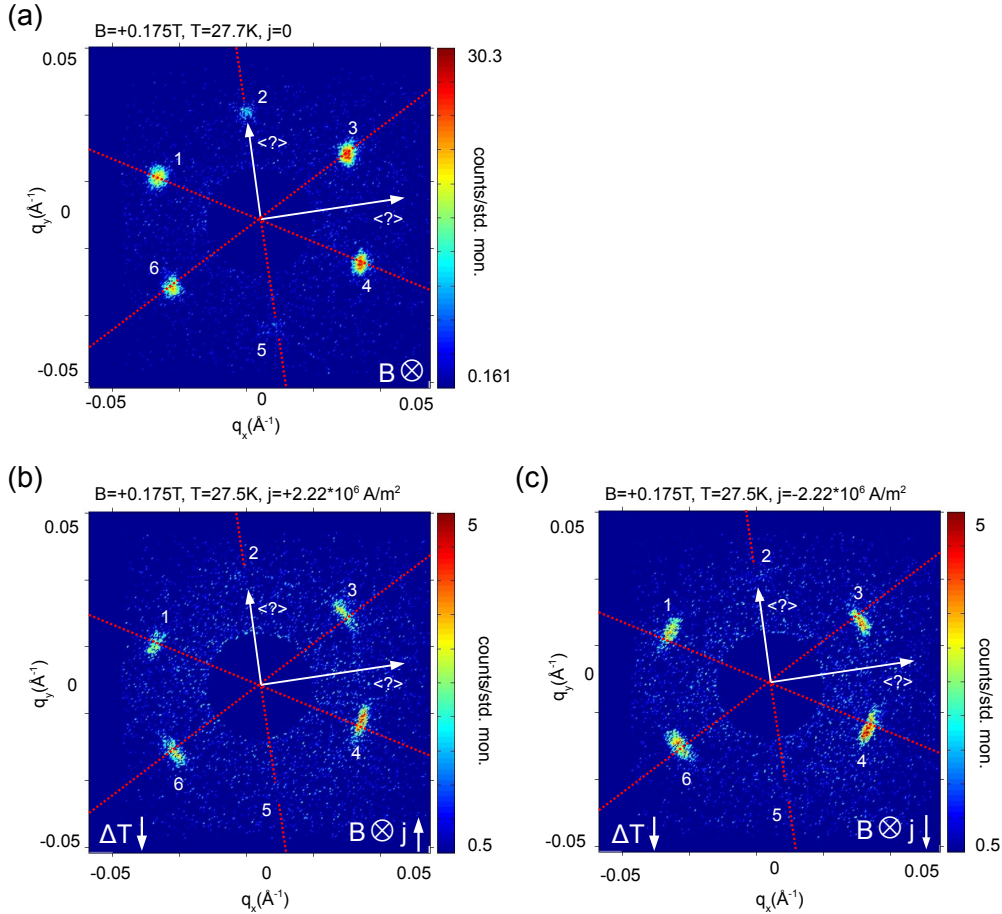
Figure 3.26: Scattering pictures of the A-phase where the sample was rotated out of crystalline orientation at positive magnetic field, (a) at zero current, (b) at positive current and (c) at negative current. The scattering pattern in (b) is rotated anti clockwise and the scattering pattern in (c) is rotated clockwise with respect to (a). The rotational sense corresponds to the one in figure 3.15.

Figure 3.27 shows the difference picture where the diffraction pattern figure 3.26 (c) was subtracted from figure 3.26 (b). The clockwise rotation of the scattering pattern at negative current direction in figure 3.26 (c) is clearly visible.

In effect, this indicates that rotating the crystal away from the crystalline orientation (by approximately 20°) does not provoke changes in the rotational behavior under current. But the current was still parallel to the vertical crystalline ⟨110⟩ axis.
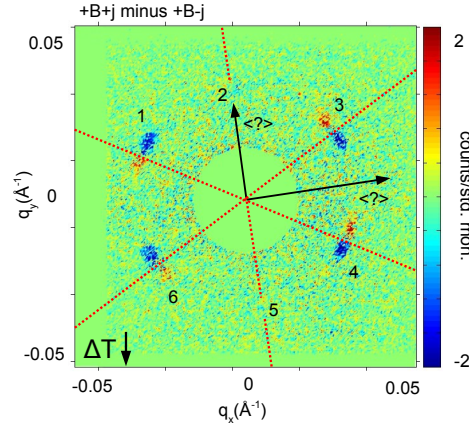
Figure 3.27: Difference of the scattering pictures (b) and (c) in figure 3.26. It shows the clockwise rotation at negative current.

Current direction parallel ⟨111⟩

The next step was to examine a completely different crystalline orientation with a sample where the current was parallel to the ⟨111⟩ axis. Sample (vi) (see table 2.1) was used. The temperature gradient was pointing upward.

Figure 3.28 (a) shows the scattering picture of the A-phase at zero current. The vertical axis of the sample is a ⟨111⟩ crystalline axis, the horizontal axis is a ⟨110⟩ axis. The direction of the neutron beam and the magnetic field is a crystalline ⟨112⟩ direction. As the skyrmion lattice is weakly pinned to the ⟨110⟩ axis, two spots emerge on the horizontal axis. The temperature of 27.7 K ensures that we are in the center of the A-phase.

Figure 3.28 (b) to (e) show the four scattering pictures at the four combinations of magnetic field and current direction. It is the analogous picture to figure 3.21, where the vertical temperature gradient pointed in the same direction. A temperature of 26.8 K was chosen, which ensured a visible rotation. The current value was again $j = 2.22 \cdot 10^6 \, \text{A/m}^2$. The current direction is parallel to the vertical axis of the sample and therefore coinciding with the ⟨111⟩ direction.

We can see that the rotational behavior is the same as in figure 3.21. This suggests that the rotational behavior is independent of the crystal orientation.

Figure 3.29 shows the difference pictures of the diffraction patterns in figure 3.28 (b) to (e). It is the analogous picture to figure 3.22 and indicates the same rotational behavior.
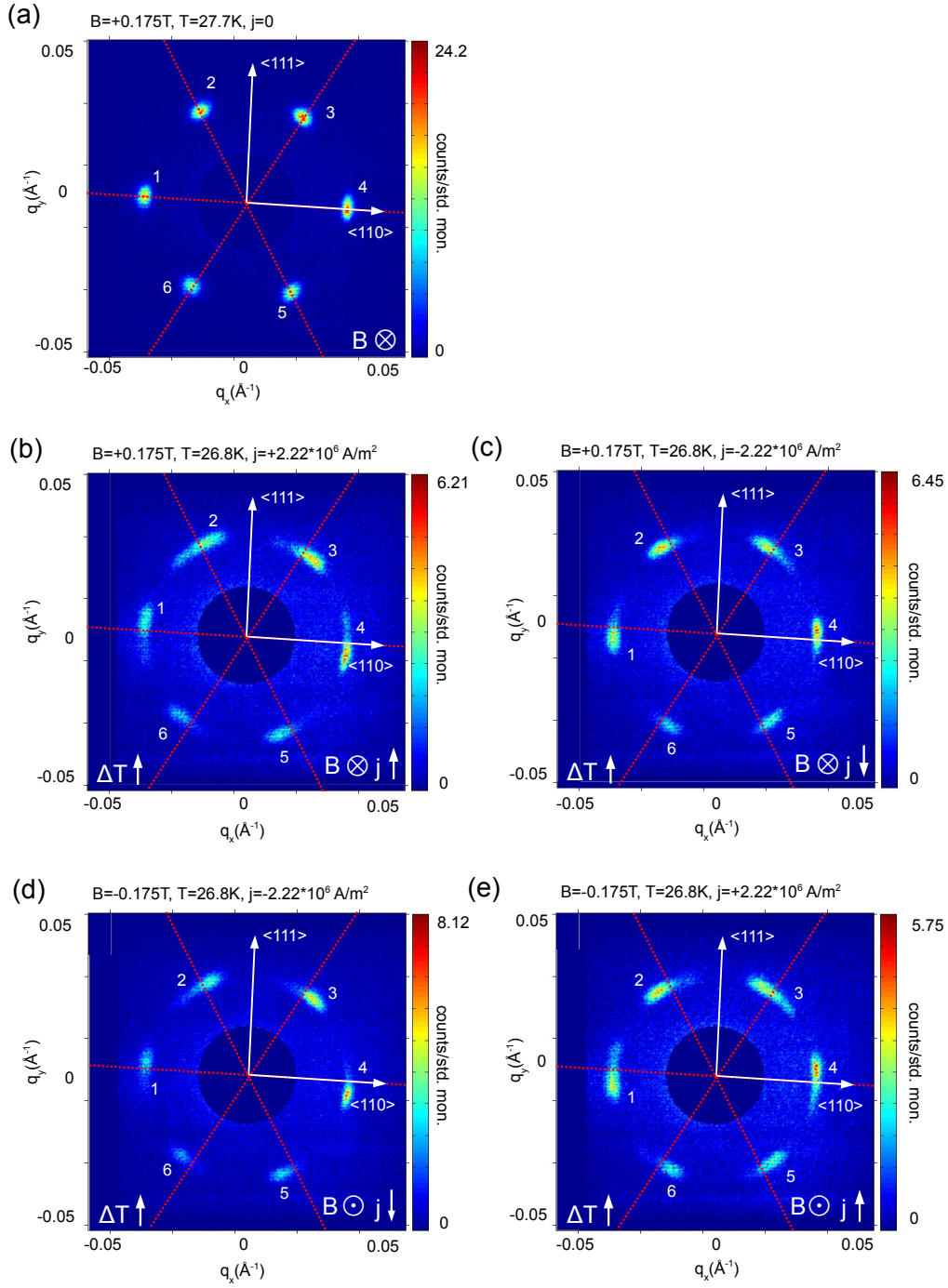
Figure 3.28: Diffraction patterns of the A-phase where the vertical sample axis is parallel to $\langle 111 \rangle$ and the beam direction is parallel to $\langle 112 \rangle$ at zero current in (a) and the four different combinations of magnetic field direction and current direction in (b) to (e). (b) Combination with magnetic field and current direction both positive. The scattering pattern is rotated clockwise. (c) Current direction negative, magnetic field positive. Scattering pattern has rotated anti clockwise. (d) Both magnetic field and current direction negative. Rotation is the same as in (b). (e) Negative magnetic field, positive current. Rotation is the same as in (c). The rotational sense with current is the same as in figure 3.21.
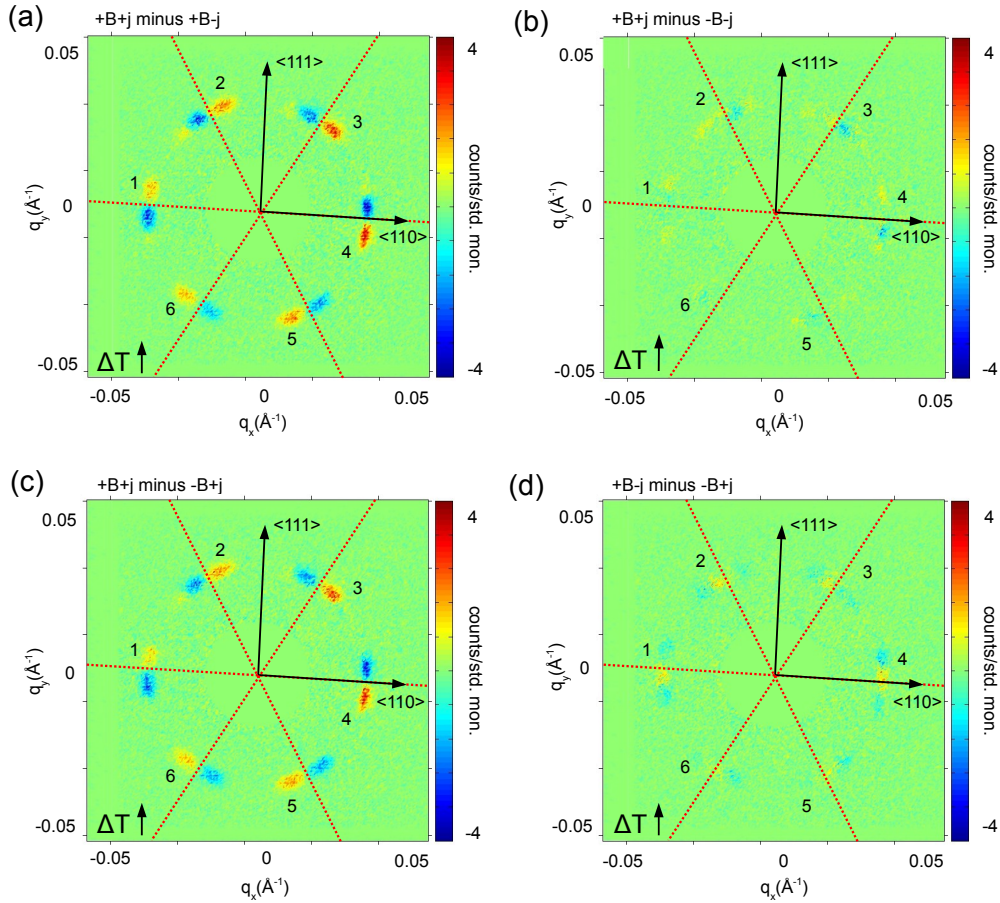
Figure 3.29: Differences of the scattering pictures in 3.28 (b) to (e). (a) Picture with negative current is subtracted from picture with both magnetic field and current direction positive. The anti clockwise rotation is visible. (b) Picture with both directions negative is subtracted from picture with both positive. No rotation is visible. (c) Picture with negative magnetic field is subtracted from picture with both directions positive. Same rotation as in (a). (d) Picture with negative magnetic field is subtracted from picture with negative current. Like in (b), no rotation is visible.

Different sample shape

Moreover, a sample with different shape (sample (iii) in table 2.1) was examined. As the sample is very thin and broad, it certainly has different demagnetizing fields. The question was whether the shape provokes any difference in the observed spin torque effects. Unfortunately, the sample broke during the experiment due to a micro fissure. Therefore, only few data could be taken. But this data indicates the same rotational behavior of the scattering patterns under current as observed in the other samples. Even the directional dependence of the rotational sense on the direction of the vertical temperature gradient seemed to be identical.

3.4.6   Current parallel to the skyrmion lines

We also tried the set-up with the magnetic field pointing in vertical direction (see figure 2.8 (b)), and thus parallel to the current direction. The current direction is then parallel to the skyrmion lines.

Figure 3.30 presents the data taken in neutron diffraction with the magnetic field pointing in vertical direction. The data was taken with sample (ii). The pictures are the summed-up intensity of a coarse rocking scan to ensure that no scattering signal from the horizontal peaks is missing. Figure 3.30 (a) shows the scattering pattern with no current applied. The temperature is $27.25\,\text{K}$, well inside the A-phase. The spots 1 and 3 are remnants of the conical phase and the spots 2 and 4 are two spots of the hexagonal scattering pattern of the A-phase. The hexagon of the skyrmion lattice lies now in the horizontal plane and only two spots can be made visible on the horizontal axis. The simultaneous existence of the conical phase and the A-phase can be explained by small temperature gradients that exist in the sample.

The diffraction pattern under an applied electric current density of $j = 1.24 \cdot 10^6\,\text{A/m}^2$ in vertical direction and thus parallel to the skyrmion lines is shown in figure 3.30 (b). Neither the spots of the conical phase nor the spots of the skyrmion lattice show any rotation or broadening whatsoever. For the same current density applied perpendicular to the skyrmion lines, strong rotations were seen in that sample.
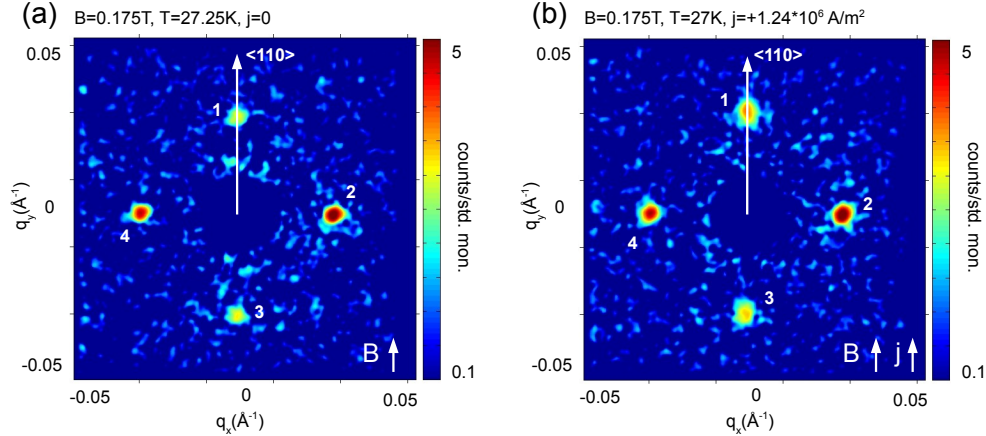
Figure 3.30: (a) Scattering picture (sum over a coarse rocking scan) in the A-phase at zero current with the magnetic field in vertical direction perpendicular to the neutron beam. The spots on the vertical axis (peak 1 and 3) are remnants of the conical phase, the peaks 2 and 4 on the horizontal axis are peaks of the skyrmion lattice which lies now in the horizontal plane. (b) Same as in (a) but with current applied in vertical direction parallel to the magnetic field. No changes to (a) are observable.

3.5   Discussion of the spin transfer torque experiments

We have described how we used neutron scattering to observe directly the influence of an electric current on the magnetic structure of MnSi. We observed non trivial current induced effects.

These effects were only seen in the A-phase of MnSi, which in the course of our experiments was identified as a skyrmion lattice, where the spins form a lattice of magnetic vortices, which are reminiscent of the vortex lattice in type II superconductors.

We were able to observe that the diffraction pattern of the skyrmion lattice rotates by an angle $\Delta\Phi$ when the currents exceed an ultra low threshold value of $10^6\,\mathrm{Am}^{-2}$, which is over five orders of magnitude smaller than the ones typically used in other spin transfer torque measurements that also examine the current driven magnetization dynamics, but are typically done in nanostructures of ferromagnetic metals and semiconductors. Some of those experiments were mentioned in 1.5.

In order to explain our results, a theory was elaborated in intensive collaboration with the group of Achim Rosch in Cologne, which shall be briefly described. The outline of this discussion follows [4].

3.5.1   Qualitative explanation of the results

Firstly, a brief and qualitative discussion will be done explaining the central parts of the theory. In accordance with the theory, our observation can be explained by an

extremely efficient coupling of spin currents to the topologically stable knots in the spin structure of the skyrmion lattice in MnSi and by the fact that the spin currents are inhomogeneous within the sample.

The skyrmion lattices in chiral magnets like MnSi are coupled very weakly to the atomic crystal structure [1]. Therefore, one expects them to pin very weakly to disorder. Furthermore, electric currents with density j couple very efficiently to skyrmions because of their magnetic vorticity. This can be explained in the following way: Electric currents also lead to spin currents, j_s, because the conduction electrons in the magnetic metal are partially spin-polarized with their spins oriented parallel to the local magnetization. When the spins follow the winding of the local magnetization, they pick up a quantum mechanical phase, the Berry phase, which leads to a very efficient, topologically quantized gyromagnetic coupling [97] of the spin currents to the skyrmions, able to deflect the current. This deflection has been observed as an additional topological contribution to the Hall effect [98]. Correspondingly, there is also a force on the magnetic structure which can be interpreted as an effective Magnus force acting on the skyrmions [99]. In figure 3.31 this Magnus force, which is perpendicular to current and field direction, is sketched together with an additional drag force arising from the flow of spin current. The Magnus and drag forces may lead to a translational motion of the skyrmion lattice, which, however, is very difficult to detect in a neutron scattering experiment. The instrumental resolutions are not sufficient for that purpose.

It has been described that in order to see the rotational effect a small temperature gradient on the sample was necessary. In the presence of a small temperature gradient, the magnetization varies in magnitude across a domain of the skyrmion lattice, and the spin currents vary accordingly. This effect of varying magnetization and therefore spin current is rather strong here (orders of magnitude estimates of the forces are given below) as the skyrmion lattice is only stable close to the transition temperature T_c, where small variations in T produce large variations in the amplitude of the local magnetization. Therefore, the strength of the Magnus force varies across the skyrmion lattice, see figure 3.31. This induces a net torque and thus a rotation which can directly be measured by neutron scattering. In contrast, the translation of the skyrmion lattice cannot be measured because, as already mentioned above, the instrumental resolution is not sufficient in neutron scattering.

3.5.2 Theory and estimates

The theory developed by the group of Achim Rosch will be briefly described without going into the details. Special emphasis is put on estimates made by this theory in order to help explain our results.

In our measurements, the electric current was applied along bar-shaped single crystals. The direction of the current was perpendicular to the magnetic field and therefore to the skyrmion lines. The neutron beam was parallel to the magnetic field. Only in this set-up (other set-ups were tried as well, as already described) could we see any non-trivial current induced effects.
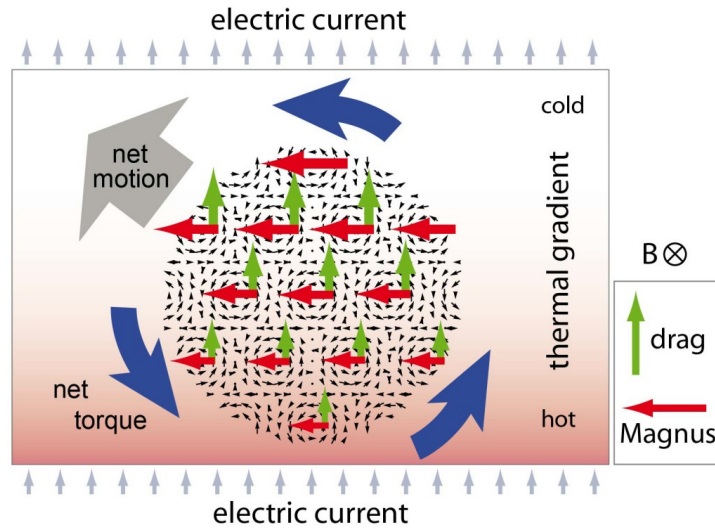
Figure 3.31: Schematic depiction of the spin transfer torque effects on the skyrmion lattice. The set-up with magnetic field parallel to the neutron beam is shown. The skyrmion lines are parallel to the line of sight, which is also the direction of neutron beam and magnetic field. The skyrmion vortex structure is depicted symbolically by the small black arrows. The current flow is in vertical direction. A temperature gradient in vertical direction combined with the electric current in the same direction induces inhomogeneous Magnus and drag forces and therefore a rotational torque.

The rotation has the following characteristics:

- The entire scattering pattern rotates around its center, i.e., all spots move by the same angle, although the electric current has a distinct direction.

- When changing the sign of the direction of the current or the direction of the applied magnetic field, the rotational sense changes sign.

- The rotation starts above a well-defined threshold of order $j_c \approx 10^6 \, \mathrm{Am}^{-2}$. For $|j| > j_c$, the scattering pattern rotates and the rotation angle rises steeply with rising $|j| - j_c$.

We can exclude a number of potential parasitic effects:

- Heating alone cannot explain the observed rotations. The temperature difference ΔT between the sample surface and the sample support was monitored. A smooth quadratic increase with current density is seen, as already described. This quadratic increase is independent of the direction of the current. This is in contrast to the observation showing

   - an antisymmetrical current dependence of the rotation angle $\Delta \Phi$ and
   - the pronounced threshold at $|j| = j_c$.

   Also, there are no changes of orientation of the skyrmion lattice as a function of temperature at $j = 0$ [100] [96] [101], which rules out temperature changes as a cause of the rotations of the skyrmion lattice.

- The Oersted field is the magnetic field created by the current through the sample. But for the current densities applied in our study, the Oersted field reaches a maximal value of roughly $1\,\text{mT}$, which is much smaller than the applied magnetic field of $175\,\text{mT}$ in the A-phase, and therefore negligible.

- For current parallel to the skyrmion lines or the helimagnetic state, neither a rotation nor a broadening are observed. So, our observations are restricted to a very specific set-up. One would expect parasitic effects to show up in a more general way independent of specific configurations. Certainly, a specific directional dependence would not be expected from simple ohmic heating effects.

The starting point of a more quantitative analysis of the forces acting on the skyrmion lattice is a Ginzburg Landau free energy:

$$F[\mathbf{M}] = \int d^3r \left(r_0 \mathbf{M}^2 + J(\nabla \mathbf{M})^2 + 2D\mathbf{M} \cdot (\nabla \times \mathbf{M}) + U\mathbf{M}^4 - \mathbf{B} \cdot \mathbf{M} \right). \qquad (3.2)$$

Here $\mathbf{M}(\mathbf{r})$ is the local magnetization, $\mathbf{B}$ the external magnetic field and r_0, D, J, U are parameters with the constraint $(U, J > 0)$ [24] [21]. As shown in [1], this theory describes the formation of the skyrmion lattice and its stabilization by thermal fluctuations. The energy scales and the hierarchy of forces in the system are determined by the strength of spin orbit coupling, λ_{SO}, which is very small in MnSi. The Dzyaloshinsky Moriya interaction $D \propto \lambda_{SO}$ determines the size of the skyrmions and the distance between them. In analogy, in the helimagnetic case this force determines the periodicity length of the helix. The distance between the skyrmions is given by $J/D \propto 1/\lambda_{SO}$ (for details see [1]).

In our case, the influence of three small additional forces, which are not included in equation 3.2, has to be considered:

- spin transfer torques, i.e., current induced forces

- pinning forces

- anisotropy terms

These terms determine the origin of our observations:

- The rotation and the angle Φ of the rotated diffraction pattern and

- the presence of a threshold of current density to trigger the rotations.

Spin transfer torques are calculated by, e.g., a Landau Lifshitz Gilbert (LLG) equation or variants of Landau Lifshitz Bloch equations [102]. These equations consider the reactive Magnus force and the dissipative drag force. Both forces are believed to be of the same order of magnitude [103]. The strength of the dissipative forces is determined by the parameter β in the LLG equations and is unknown, but one

can estimate the strength of the reactive forces. As explained above in the more qualitative description of the mechanisms involved, the Magnus forces arise when the spin of an electron picks up a Berry phase in a skyrmion lattice, which can be expressed as an Aharonov Bohm phase arising from a fictitious magnetic field. This is discussed in more detail in [98] [104] [105] [106]. The fictitious magnetic field is

$$\mathbf{B}_{\text{eff}}^i = \frac{\Phi_0}{8\pi}\epsilon_{ijk}\hat{M}(\partial_j\hat{M} \ \times \ \partial_k\hat{M}), \tag{3.3}$$

where $\hat{M} = \mathbf{M}/|M|$ is the direction of the magnetization and $\Phi_0 = h/e$ is the flux quantum.

In the skyrmion lattice of MnSi, B_{eff} has a topologically quantized average strenth of (-1) times a flux quantum per area of the magnetic unit cell, $B_{\text{eff}} \approx 2.5\,\text{T}$ (a more detailed explanation of this can be found in [98]). This effective field couples directly to the spin current j_s.

From B_{eff}, an effective Lorentz force arises, which has been observed experimentally in MnSi as a topological contribution to the Hall effect [98] [107]. Because the electrons are deflected, a force acts on the magnetic structure, which generates an efficient gyromagnetic coupling of the current to the skyrmion lattice [97] [99]. The counter force of the Lorentz force is the Magnus force per volume, f_M, which acts on the skyrmions. Its strength may be estimated as

$$\begin{aligned} f_M \approx ej_s B_{\text{eff}} &\approx p(T) \cdot \frac{j}{10^6\,\text{Am}^{-2}} \frac{2.5 \cdot 10^6\,\text{N}}{\text{m}^3} \\ &\approx p(T) \cdot \frac{j}{10^6\,\text{Am}^{-2}} \frac{2.7 \cdot 10^{-10}\,k_B T_c}{a^4}, \end{aligned} \tag{3.4}$$

where $a \approx 4.58\,\text{Å}$ is the lattice constant of MnSi and $T_c \approx 29.5\,\text{K}$ is the ordering temperature.

The local polarization is temperature-dependent and is defined as the ratio of the spin and charge current times the elementary charge, $p(T) = ej_s/j$. For the skyrmion phase it can be estimated $p(T) \approx 0.1$ (see [98]).

When this local polarization is inserted into equation 3.4, then one can see that already at the studied current densities j of $10^6\,\text{Am}^{-2}$ the resulting forces are considerable and much larger than, e.g., gravitational forces on the sample.

But at the same time, the forces are small in respect of the microscopic units, $k_B T_c/a^4$ (cf. equation 3.4). This raises the question why the critical currents are so small.

For $j < j_c$, the current induced forces are outweighed by pinning forces. These pinning forces are due to disorder and due to pinning by the underlying regular atomic crystal lattice. The pinning forces due to the crystal lattice may be neglected because they are exponentially small in $1/\lambda_{SO}$ [80]. This means that the pinning forces must arise from disorder.

It is interesting to compare this situation with the vortices in type II superconductors. There, the vortex cores are pinned by disorder. This pinning can be very

efficient because the order parameter (in this case the superconducting wave function, or simply the cooper pair density) vanishes on the core of the vortex and varies on a length scale typically much smaller than the vortex distance [108]. On the contrary, the amplitude of the magnetization of the skyrmion lattice (which plays the role of the order parameter here) is smooth and varies only weakly [1].

Several effects contribute to the very weak pinning in MnSi:

- The defect concentration in our samples is very low. This is seen by the large charge carrier mean free paths around $1000\,\text{Å}$, derived from the high residual resistivity ratio (RRR).

- The free energy density of the skyrmion lattice is small. It is estimated from the measured specific heat [109] and amounts to $\Delta F/V \sim 10^{-2}\, k_B T_c/a^3$.

- Pinning forces, which arise from the coupling to the magnitude of the magnetization, are small, because the magnitude varies slowly and by less than $\pm 20\%$ within the magnetic unit cell [1].

- The coupling of disorder to the direction of the spins is due to spin orbit interactions and hence very small.

- The forces, i.e., the energy changes per length, are small because the distance between the skyrmions is about a factor 40 larger than the lattice constant of MnSi ($a \approx 4.58\,\text{Å}$).

When taken together, these effects imply that even very strong defects, which destroy the magnetization locally, lead to a very small pinning force, $F_{max} \lesssim 10^{-5}\, k_B T_c/a$ per impurity. The measured critical current density j_c and the estimate of the Magnus force in equation 3.4 are therefore in accordance with strong pinning defects with a density below 1 ppm. Even if the real density of defects is higher in reality, their influence might be very weak since the system is in the collective pinning regime, which is known, e.g., from vortices in superconductors [108]. It means that the pinning forces average out because they are of random orientation and the skyrmion lattice has a pronounced rigidity.

Now the cause of the rotations and their size is being addressed in a quantitative way. The rotation of the skyrmion lattice for $j > j_c$ is determined by the balance of the torques τ_M and τ_L. τ_M is the torque due to the inhomogeneous Magnus forces and τ_L is the torque due to the atomic lattice. For symmetry reasons, the orientation of a skyrmion lattice (described by a third rank tensor) cannot be linearly influenced by the current j because of the hexagonal symmetry of the skyrmion lattice. A temperature gradient, however, breaks the symmetry and induces a varying magnetization amplitude, as the skyrmion lattice only exists close to T_c. These variations of the magnetization lead to variations in the polarization $p(T)$ of the electric currents. The Magnus force, which is described by equation 3.4, is proportional to the spin currents and thus to $p(T)$. As a result of the varying polarization $p(T)$, the Magnus force will be larger at the cold side of the skyrmion lattice than at the hot

side. This results in a net torque per volume

$$\boldsymbol{\tau}_M \sim \int \mathbf{r} \times \mathbf{f}_M(\mathbf{r}) d^3r / V.$$

Now, equation 3.4 is used for an order of magnitude estimate. For this purpose, a spatially varying $p(T)$ is inserted and dissipative forces are neglected for the estimate. Then, the rotational torque per volume, $\boldsymbol{\tau}_M$, in direction of the fictitious magnetic field $\mathbf{B}_{\text{eff}}$ for a skyrmion lattice domain of size R results in

$$\tau_M \sim 10^{-10} \frac{\mathbf{j} \cdot \boldsymbol{\nabla} p}{10^6 \, \text{Am}^{-2}} \frac{R^2}{a} \frac{k_B T_c}{a^3} \sim 10^{-5} \frac{k_B T_c}{a^3} \left(\frac{R}{1 \, \text{mm}} \right)^2. \qquad (3.5)$$

We inserted $j \approx j_c$ and $\nabla p \approx 0.1/10 \, \text{mm}$. The torque is proportional to the temperature gradient parallel to the current because

$$\boldsymbol{\nabla} p \approx \frac{\partial p}{\partial T} \boldsymbol{\nabla} T.$$

For a visualization of this see figure 3.31. $\boldsymbol{\tau}_M$ changes sign when current, magnetic field or temperature gradient change sign. This explains the most important results of our measurements. When we consider that charge carriers are holelike [98] [107], the sign of $\boldsymbol{\tau}_M$ and the other forces (see figure 3.31) is in accordance with our measurements.

We have explained that the rotational torques are caused by gradients in the spin current, which are induced via magnetization gradients that are, in turn, induced by temperature gradients.

We want to point out that it is more complicated to create a similar effect for vortices in superconductors, because, in contrast to the spin in skyrmion lattices, charge is exactly conserved. In order to induce rotations in superconductors, special tricks have to be used. In [110], a rotation of a superconducting vortex lattice was generated by varying current densities within the sample.

In order to estimate the factor $(R/1 \, \text{mm})^2$ in equation 3.5, an estimate of R, the skyrmion lattice domain size, must be made. It can be deduced from the rocking width of the magnetic Bragg peaks of the skyrmion lattice. From these rocking curves, a lower limit of $R > 1 \, \mu\text{m}$ is obtained.

Although the torque τ_M might be small, it can lead to large rotation angles, because the balancing torque, τ_L, which determines the orientation of the skyrmion lattice with respect to the atomic lattice, is small. The rotation angle Φ describes the orientation of the skyrmion lattice in the plane perpendicular to $\mathbf{B}$ for $j = 0$. It is only fixed by higher order anisotropy terms, since the free energy of equation 3.2 to leading order is invariant under rotations around $\mathbf{B}$. Because of the hexagonal symmetry of the skyrmion lattice, a potential that is proportional to $-\cos(6\Phi)$ is needed to fix Φ. Such a potential can only occur due to terms suppressed by the small factor λ_{SO}^6 with $\lambda_{SO} \sim 10^{-2}$. One of these terms is

$$\int (\partial_x^3 \mathbf{M})^2 + (\partial_y^3 \mathbf{M})^2 + (\partial_x^3 \mathbf{M})^2.$$

This term is proportional to the very small factor λ_{SO}^6 because the distance of skyrmions $\sim J/D$ is linearly dependent on $1/\lambda_{SO}$. On the contrary, the energy density of the skyrmion lattice, which is of the order of $\Delta F/V \sim 10^{-2} k_B T_c/a^3$ [109], is proportional to λ_{SO}^2 [1].

The torque per volume arising from the coupling to the atomic crystal lattice, τ_L, is then of the order

$$\tau_L \sim -10^{-2}\lambda_{SO}^4 \frac{k_B T_c}{a^3} \sin(6\Phi). \qquad (3.6)$$

For small rotation angles, one sees from equation 3.6 that the torque τ_L is linearly dependent on the rotation angle Φ. Contrary to the torques resulting from the inhomogeneous Magnus force, τ_L is independent of the domain size R.

The rotation Φ is governed by the balance of τ_M and τ_L. The small prefactor in equation 3.6, $10^{-2}\lambda_{SO}^4$, allows for the large rotation angles seen in our measurements, even for small domains, i.e., small R.

For $j > j_c$, simultaneous to the rotation, probably also a linear motion of the magnetic structure begins, because the rotation of a magnetic domain needs a depinning from defects, which would also allow for a translational movement corresponding to the forces acting on the structure (see also figure 3.31). As the domains move, the spin currents that are inserted in all formulas above have to be calculated in a frame of reference that moves with the domain. The translational motion experiences frictional forces which determine the velocity of the motion. These frictional forces break Galilean invariance [103]. Because the velocity of the translational motion enters in all the formulas given above, the rotation finally also depends strongly on the frictional forces.

Now, the observed broadening of the scattering pattern in the presence of a current will be discussed briefly. It can have different origins:

- The rotational torques, given in equation 3.5, depend strongly on the size of the domain and the local T gradients. This may give rise to a distribution of rotation angles, which is visible as a broadening of the diffraction peaks.

- For the symmetrical set-up with no extra forced temperature gradient (here we could not see the rotations), symmetrical thermal gradients may explain the spread of the angular distribution and the corresponding broadening of the diffraction peaks.

- An irregular shape of magnetic domains can lead to additional rotational torques of random sign, giving rise to a distribution of rotation angles and the corresponding broadening of the diffraction peaks.

- The interplay of pinning and Magnus forces can give rise to extra rotations. During the depinning, in some regions of the sample the rotation already starts, when at other regions this process has not started yet. The consequence would be a distribution of rotation angles and the corresponding broadening of the diffraction peaks.

3.5.3   Conclusion and outlook of the spin transfer torque measurements

The next experimental challenge will be the direct observation of the current induced motion of the skyrmion lattice in real space. Typical velocities of the motion to be expected will be similar to the drift velocity of the conduction electrons v_D, which is given by the current density divided by the number density of the electrons. It is assumed that $v_D \ll 1 \, \mathrm{mm/s}$.

In conclusion, we observed spin transfer torques at ultra low current densities of order $10^6 \, \mathrm{Am}^{-2}$ in the skyrmion lattice of MnSi. We conclude that helical magnets and non trivial topological structures are very convenient to improve the knowledge of spin transfer torque effects. As an example, spin transfer torques might be applied to manipulate single skyrmions, which were recently discovered in thin samples [101]. Surfaces and interfaces of complex magnetic structures could also show spin torque effects [111].

Chapter 4

Results of the spin fluctuation measurements

4.1 Determining T_c

In order to determine the transition temperature T_c, temperature scans were done on the magnetic satellite.

The quadratic symbols in figure 4.1 represent the temperature scan for MnSi on one of the magnetic satellite peaks. The temperature range begins at zero, but only temperatures around the transition temperature were measured, where the intensity already drops rapidly with increasing temperature. The transition temperature is T_c=28.9 K (indicated by the arrow). Above T_c, an intensity tail is visible, which originates from critical scattering. The value for T_c, the steep slope at T_c and the intensity tail due to critical scattering are in agreement with literature.
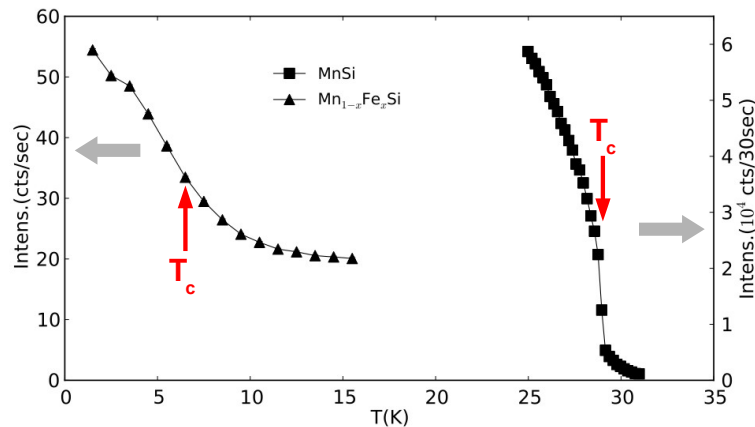
Figure 4.1: Temperature scan of the magnetic satellite in MnSi and $Mn_{1-x}Fe_xSi$. The transition temperatures are indicated by arrows. Error bars are smaller than symbol size.

In $Mn_{1-x}Fe_xSi$, there are no discrete magnetic peaks, instead, the magnetic scattering is smeared out on a sphere with a radius corresponding to the helical pitch because the direction of the helices is not pinned due to small anisotropy terms, i.e.,

the magnetic Bragg peaks are distributed on a sphere in reciprocal space. The triangular symbols in figure 4.1 represent the temperature scan on a selected point on the sphere. The intensities between the quadratic symbols and the triangular symbols cannot be compared. The temperature dependence is very different from the one in MnSi. The intensity also drops with increasing temperature, but no sharp transition is visible. Therefore, the transition temperature cannot be determined with this plot, but one can see that it is much lower than in MnSi. Bulk measurements [47] determined a T_c of 6.5 K (indicated by the arrow). The reason that the transition temperature T_c is much lower than in MnSi is the disorder introduced by the doping with Fe atoms. Furthermore, the intensity of the magnetic signal in $Mn_{1-x}Fe_xSi$ compounds is much weaker than in MnSi, which is also due to the disorder and, in particular, to the fact that the intensity is distributed on a sphere in reciprocal space instead of discrete peaks.

The incoherent elastic scattering is a constant background in both temperature scans. It is much larger in $Mn_{1-x}Fe_xSi$ than in MnSi due to the different neutron scattering lengths of Mn and Fe. The scattering length for Mn is $b_1 = -3.73$ fm, and the scattering length for Fe is $b_2 = 9.45$ fm. In our $Mn_{1-x}Fe_xSi$ sample with $x = 0.12$, the concentrations are $c_1 = 0.88$ for Mn and $c_2 = 0.12$ for Fe. The incoherent cross section is defined as $\sigma_{inc} = 4\pi(\overline{b^2} - (\overline{b})^2)$. With $\overline{b} = c_1 b_1 + c_2 b_2$ and $\overline{b^2} = c_1 b_1^2 + c_2 b_2^2$, this results in $\sigma_{inc} = 4\pi c_1 c_2 (b_1 - b_2)^2$. Therefore, a large difference in scattering lengths results in large incoherent scattering. In figure 4.1, the incoherent elastic scattering of MnSi is negligible, but for $Mn_{1-x}Fe_xSi$, it can be assumed that the intensity at the highest temperatures of around 15 K, i.e. at temperatures much higher than $T_c = 6.5$ K, is mainly due to incoherent scattering. Obviously, the magnetic scattering below T_c in $Mn_{1-x}Fe_xSi$ is of the same order of magnitude as the incoherent scattering.

4.2   Measurement of pure MnSi at PANDA

In the following, the results are presented that were obtained in the measurements of pure MnSi at PANDA.

The wave vector of the scattered neutrons was $k_f = 1.2 \, \text{Å}^{-1}$, which corresponds to a neutron energy of 2.98 meV. The collimation was 80' in all four spectrometer arms, resulting in a measured energy resolution of 0.074 meV.

In the experiment, the quasi-elastic spectra were measured at different constant q vectors and at different temperatures above T_c.

Figure 4.2 illustrates schematically the reciprocal space near the nuclear (110) Bragg peak with the magnetic satellite peaks and the reciprocal space positions of the points where the quasi-elastic spectra are measured. The q vectors were all parallel to the [110] crystalline direction. The reciprocal space units of the q vectors were $Q = (1 - \zeta, 1 - \zeta, 0)$ with $\zeta = 0.045, 0.050, 0.054$ and 0.075. A ring centered around the nuclear peak is drawn through the magnetic satellite peaks (red dashed line). It represents the intersection of the horizontal plane with a sphere in reciprocal space

that has a radius corresponding to the helical pitch. The reduced q vector q_{red} shall be defined as the distance between the reciprocal space position of the measurement point and the nearest point on the ring. The distance to the nuclear (110) Bragg peak shall be defined as q_{nucl}.
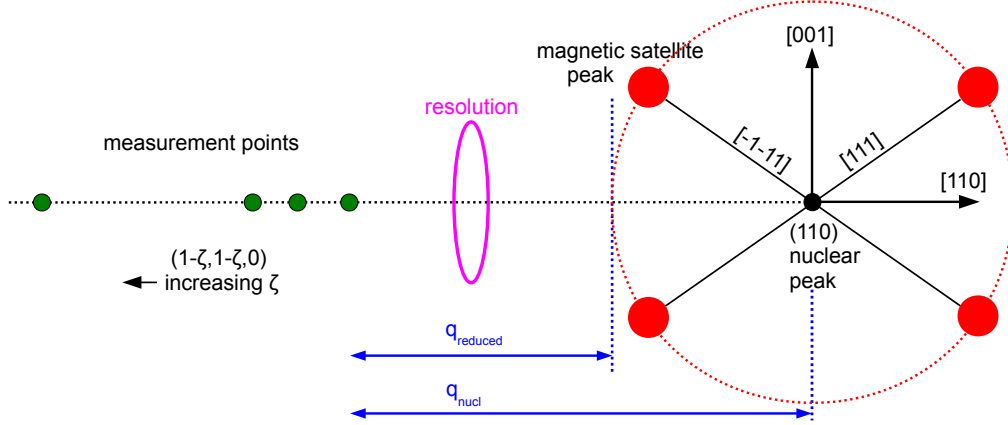
Figure 4.2: Schematic view of the reciprocal space near the nuclear (110) peak with the magnetic satellite peaks (red points) and the positions of the points where the quasi-elastic spectra are measured (green points). The ζ values are 0.045, 0.050, 0.054 and 0.075. The resolution is shown by the ellipse drawn in magenta.

Table 4.1 shows the ζ values, the corresponding q_{nucl} and q_{red}, and the temperatures at which the measurements were carried out. The wave vector of the helix in MnSi is $0.038\,\text{Å}^{-1}$, corresponding to $\zeta = 0.019$.

Table 4.1: Reciprocal space positions and temperatures of the measurements.

ζ	$q_{nucl}(\text{Å}^{-1})$	$q_{red}(\text{Å}^{-1})$	$T(\text{K})$
0.045	0.088	0.050	T_c, T_c+0.075, T_c+0.15, T_c+0.45, T_c+1.2, T_c+2, T_c+3, T_c+4
0.05	0.098	0.060	T_c+2.1
0.054	0.106	0.068	T_c+0.15, T_c+0.45, T_c+0.95, T_c+1.2
0.075	0.146	0.108	T_c+0.15, T_c+0.45, T_c+1.2, T_c+2.1

The measured intensities and their errors were normalized for a counting time of 30 seconds per point, i.e. they were divided by the number of incident neutrons and then multiplied by a factor corresponding to a measurement time of 30 seconds (given on the label of the y-axis). This measurement time gives us a scale for the signal strength. The real typical measurement times were 3.5 minutes per point at the central peak (high intensity) and 10 minutes per point at the intensity tails.

Figure 4.3 shows as an example a scan as measured for $\zeta = 0.045$. The raw data is represented by the black symbols. The background measurement is represented by the blue symbols. The background was measured at a low temperature of $3.5\,\text{K}$, where the contribution of magnetic scattering at $E = 0$ can be neglected and only the incoherent elastic scattering is relevant. The background points are fitted by a Gaussian (blue line), assuming a Gaussian instrument resolution. This Gaussian is

then subtracted from the data shown in black, resulting in the difference data shown in red, which is the convolution of the instrument resolution with the Lorentzian line shape of the paramagnetic scattering. This difference data will be analyzed in the following.
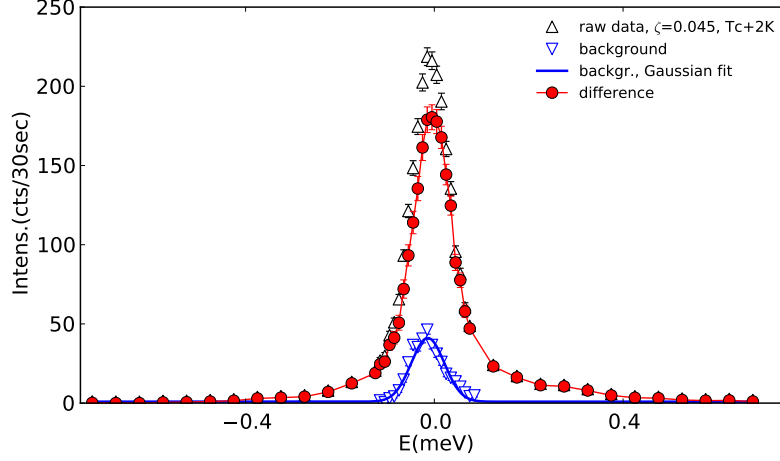
Figure 4.3: Raw data shown in black, background data in blue. The background is fitted by a Gaussian (blue line) which is then subtracted from the black data, resulting in the red difference data.

The analysis will be done using the four-dimensional deconvolution in $(\mathbf{q}, \omega)$ space with the program ResLib 3.4a [112]. It was developed by Andrey Zheludev, ETH Zürich, and is written in MATLAB.

The cross section contains a spectral weight function, which is assumed to be a Lorentzian in energy, and the Bose factor $\langle n \rangle$ [5] [113].

$$S(\mathbf{q}, \omega) = k_B T \cdot A_L \cdot \frac{1}{\pi} \cdot \frac{\Gamma}{(\hbar\omega)^2 + \Gamma^2} \cdot \frac{\hbar\omega}{k_B T} \cdot \langle n + 1 \rangle, \qquad (4.1)$$

with

$$\langle n + 1 \rangle = \frac{1}{1 - \exp(-\hbar\omega/k_B T)}. \qquad (4.2)$$

A_L is a measure for the intensity of the magnetic scattering (it becomes larger with more material in the beam) and Γ is the linewidth (HWHM). The parameters A_L and Γ were fitted. For isotropic ferromagnets, A_L is given in a good approximation by

$$A_L = \chi(0) \frac{\kappa^2}{\kappa^2 + q^2}, \qquad (4.3)$$

where $\chi(0)$ is the bulk susceptibility and κ is the inverse correlation length. For MnSi, κ^2 can be approximated by [6]

$$\kappa(T)^2 = \kappa_0^2 \cdot \frac{T - T_c}{T_c}. \qquad (4.4)$$

Ishikawa *et al.* determined a value of $\kappa_0^2 = 0.0325\,\text{Å}^{-2}$ [6]. As MnSi is considered to be a weak itinerant ferromagnet, the q dependence of the linewidth is given as [5] [6]

$$\Gamma(q) = \Gamma_0 \cdot q(\kappa^2 + q^2). \tag{4.5}$$

In earlier works [5] [6], the fluctuations were measured assuming that the relevant momentum transfer q is related to the nuclear Bragg peak (as for an isotropic ferromagnet), and therefore q_{nucl} was used as q in the equations above. In our case, we have a helimagnet, where the Dzyaloshinsky Moriya interaction plays a decisive role. In more recent works [9] [8] [37] [7], the helimagnetic stucture is considered by using q_{red} as q, because the relevant momentum transfer is related to the wave number of the helical pitch.

In the quasi-elastic spectra, after subtracting the background, a sharp spurion still remained close to T_c at low values of ζ. In figure 4.4, the data at $\zeta = 0.045$ and $T = T_c$ after subtracting the background is displayed. The red data points on the positive energy side show the spurion. It only appears on the neutron energy loss side (positive energies). Note, this spurion is absent in figure 4.3 because of the larger temperature there ($T_c + 2\,\text{K}$). The vanishing of the spurion with rising temperature indicates that it is of magnetic origin (e.g. it can be caused by erroneous scattering at a magnetic satellite in combination with incoherent scattering from the monochromator or analyzer, see [94]). In order to remove it, it was parameterized by the green Gaussian curve, which was subtracted from the data, resulting in the data represented by the black symbols. However, even after the subtraction of the spurion, a broad shoulder remains at the positive energy side. This shoulder is considered as a spurious remnant and will be fitted during the course of the data analysis by a broad Gaussian centered at the position of the (removed) spurion:

$$A_G \cdot \exp\left(-\frac{(\omega - \omega_G)^2}{2 \cdot \sigma^2}\right). \tag{4.6}$$

The overall cross section was then the sum of equation 4.1 and 4.6. Initially, all three parameters A_G, ω_G and σ were fitted, but it turned out that ω_G is roughly given by the position of the spurion (at $0.28\,\text{meV}$), therefore it was then fixed at that position. The width σ did not vary much between the data sets, and due to the strong correlation between all the fit parameters, σ was fixed for some data sets (namely the data at $\zeta = 0.075$).
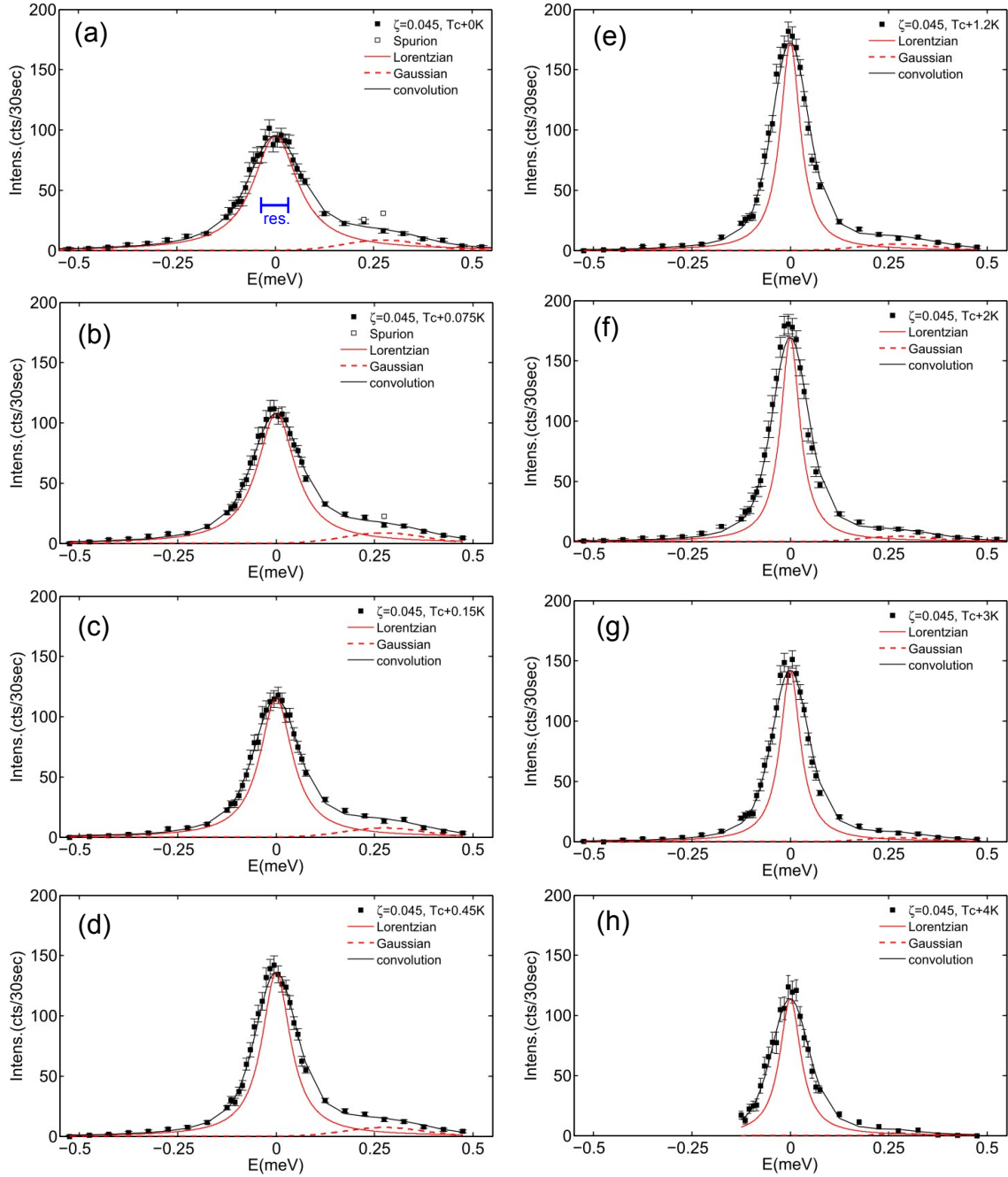
Figure 4.5 shows the analysis for $\zeta = 0.045$ at all measured temperatures. The temperatures are rising from (a) to (h). The black symbols represent the data after subtracting the background due to incoherent elastic scattering. The spurion centered at around $0.28\,\text{meV}$ is shown by the white symbols. It is only visible at low temperature in (a) and (b). The red line represents the Lorentzian cross section of equation 4.1 that was obtained by taking the resolution into account. It was fitted together with the broad Gaussian in equation 4.6, which is shown by the dashed red line. The black line is the convolution of the instrument resolution with the overall cross section (sum of red line and dashed red line), which fits the data well. The red curves are scaled so that the highest point of the red curve coincides with the highest point of the black curve. The scale of the energy and the intensity is the same in all spectra. One can see that the linewidth of the Lorentzian decreases with
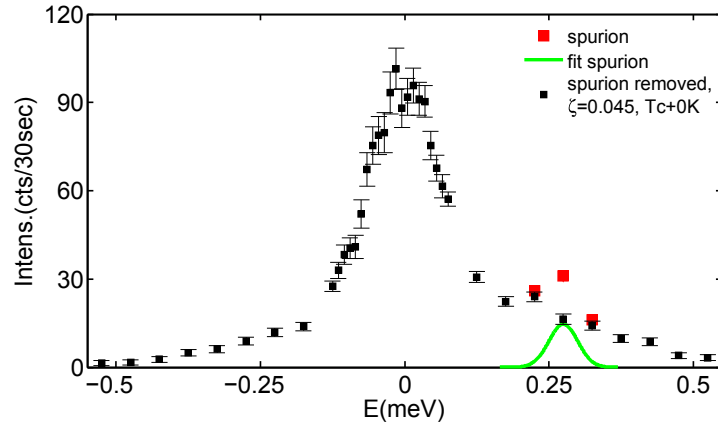
Figure 4.4: Red data points: Spurion. Green curve: Spurion parameterized by a Gaussian. Black data points: Data with removed spurion.

increasing temperature. The energy resolution (FWHM) is shown by the blue scale in figure 4.5 (a). It can be seen that the energy resolution of PANDA was excellent.

Figures 4.6, 4.7 and 4.8 show the similar analysis for $\zeta = 0.050$, $\zeta = 0.054$ and $\zeta = 0.075$, respectively. The scales of the energy are the same as in figure 4.5. The data indicates that the magnetic signal drops significantly with increasing ζ (therefore, the scale of the intensity was adapted).

Figure 4.5: Analysis for $\zeta = 0.045$ at all measured temperatures (rising from (a) to (h)). Black symbols: Data after background subtraction. White symbols: Spurion. Red line: Lorentzian cross section. Dashed red line: Gaussian to fit the shoulder. Black line: Convolution of instrument resolution with overall cross section, which fits the black data points. The energy resolution is shown by the blue scale in (a).
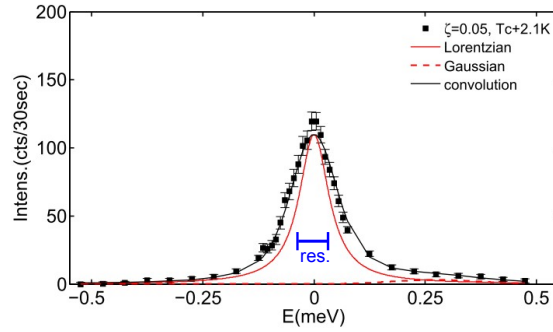
Figure 4.6: Analysis for $\zeta = 0.05$. Only one temperature was measured. The symbols have the same meaning as in figure 4.5. The energy resolution is shown by the blue scale.
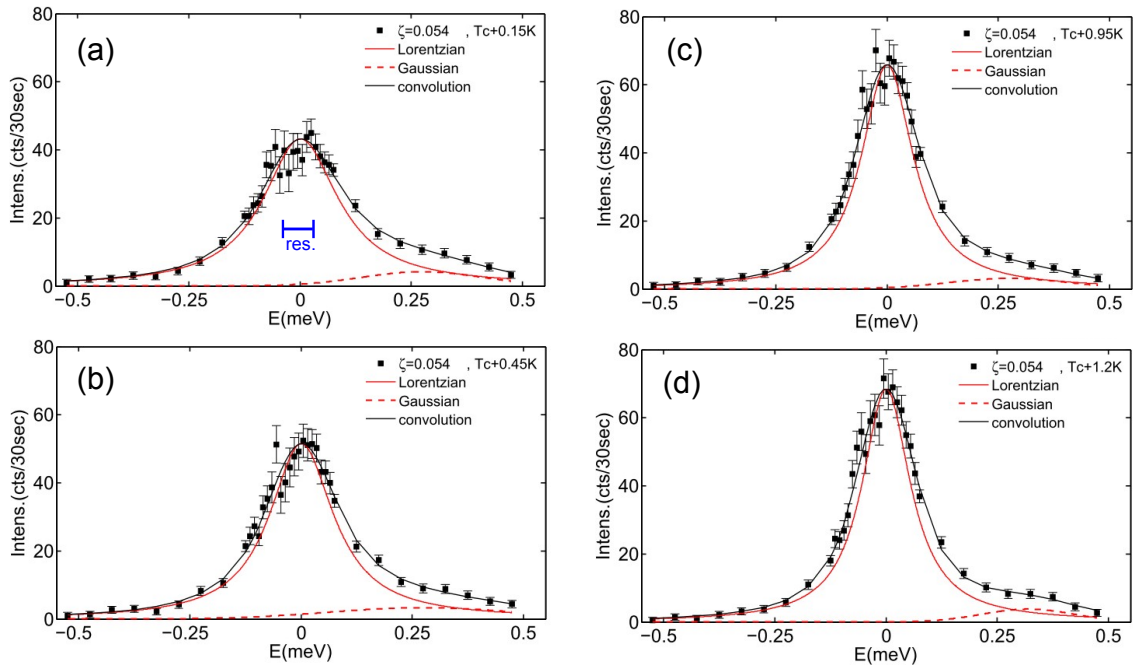
Figure 4.7: Analysis for $\zeta = 0.054$. Rising temperature from (a) to (d). The symbols have the same meaning as in figure 4.5. The energy resolution is shown by the blue scale in (a).
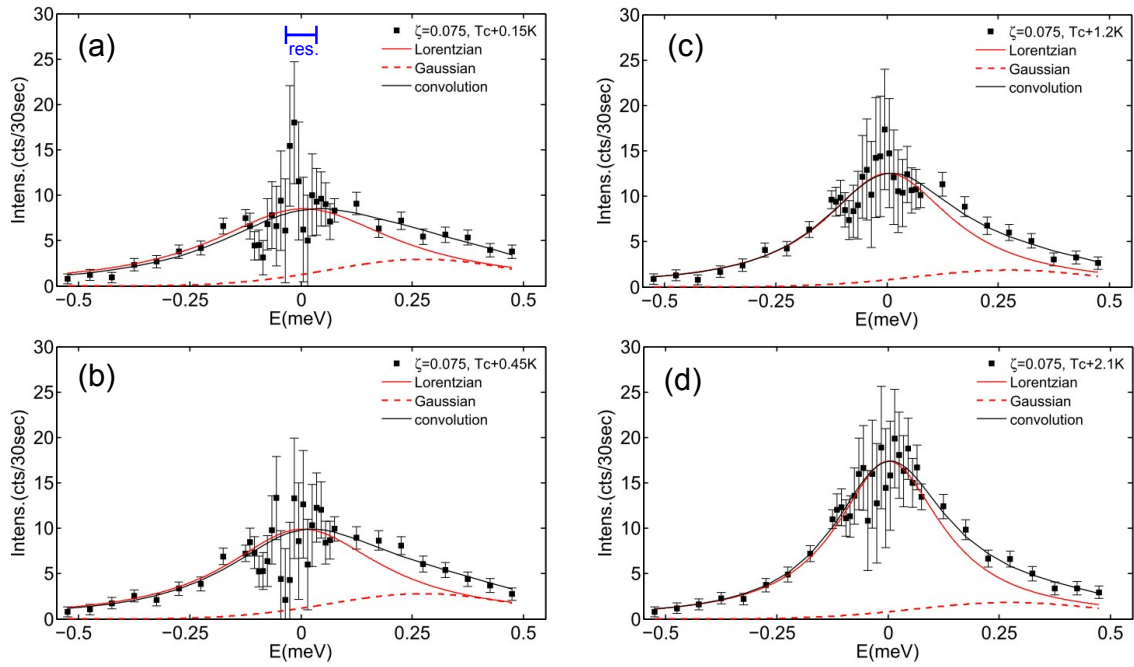
Figure 4.8: Analysis for $\zeta = 0.075$. Rising temperature from (a) to (d). The symbols have the same meaning as in figure 4.5. The energy resolution is shown by the blue scale in (a)

The fit parameters A_L, Γ and A_G are listed in tables 4.2 to 4.5, where each table is for one value of ζ. The parameters A_L and A_G are given in arbitrary units, they cannot be compared within the table. The heights of the Lorentzian and the Gaussian relative to each other are correctly given by the red lines and the dashed red lines in figures 4.5 to 4.8. Also shown is the χ^2 of the fit. It is often less than one. This is due to the fact that the background was fitted and then subtracted and that the errors of the background signal are included in the errors of the difference signal. Therefore, the difference signal can be smoother than the error bars might indicate, thus resulting in a small χ^2. This effect is particularly strong at large ζ.

Table 4.2: Parameters obtained in the fits at $\zeta = 0.045$.

ζ	T(K)	A_L (a.u.)	Γ(meV)	A_G (a.u.)	χ^2
0.045	$T_c + 0$	12.34±0.45	0.069±0.004	20.85±4.56	1.0
0.045	$T_c + 0.075$	12.34±0.43	0.059±0.004	21.66±4.35	0.9
0.045	$T_c + 0.15$	11.76±0.40	0.050±0.003	20.03±4.25	0.8
0.045	$T_c + 0.45$	12.49±0.39	0.044±0.003	19.92±4.18	1.1
0.045	$T_c + 1.2K$	12.43±0.35	0.031±0.002	16.44±3.88	2.0
0.045	$T_c + 2$	11.52±0.32	0.030±0.002	13.78±3.75	2.5
0.045	$T_c + 3$	9.46±0.30	0.031±0.002	9.92±3.82	1.8
0.045	$T_c + 4$	7.48±0.38	0.033±0.004	5.63±4.26	1.2

Table 4.3: Parameters obtained in the fit at $\zeta = 0.05$.

ζ	T(K)	A_L (a.u.)	Γ(meV)	A_G (a.u.)	χ^2
0.050	$T_c + 2.1$	8.78±0.36	0.041±0.004	8.32±4.61	1.0

Table 4.4: Parameters obtained in the fits at $\zeta = 0.054$.

ζ	T(K)	A_L (a.u.)	Γ(meV)	A_G (a.u.)	χ^2
0.054	$T_c + 0.15$	7.28±0.48	0.103±0.010	8.81±3.56	0.5
0.054	$T_c + 0.45$	7.36±0.71	0.088±0.009	7.05±2.49	0.7
0.054	$T_c + 0.95$	7.97±0.40	0.071±0.006	6.95±3.21	0.5
0.054	$T_c + 1.2$	7.80±0.34	0.066±0.005	8.71±3.55	0.6

Table 4.5: Parameters obtained in the fits at $\zeta = 0.075$.

| ζ	T(K)	A_L (a.u.)	Γ(meV)	A_G (a.u.)	χ^2
0.075	$T_c + 0.15$	2.73±0.47	0.252±0.057	4.81±1.81	0.7
0.075	$T_c + 0.45$	2.79±0.43	0.215±0.045	4.73±1.79	0.6
0.075	$T_c + 1.2$	3.01±0.38	0.175±0.032	3.39±1.74	0.5
0.075	$T_c + 2.1$	3.43±0.51	0.144±0.022	3.41±1.71	0.3

The values of A_L are plotted against the temperature in figure 4.9, where each color represents one value of ζ. Clearly, A_L decreases with increasing ζ. This is in qualitative agreement with equation 4.3, as q is in the denominator. At a constant ζ

value, A_L seems to be temperature-independent below approximately 31 K. The data at $\zeta = 0.045$ (the only data measured to higher temperatures) indicate a decrease with rising temperature above 31 K. According to equation 4.4, κ increases with increasing temperature. As a consequence, the term $\frac{\kappa^2}{\kappa^2+q^2}$ in equation 4.3 rises (it is zero at $\kappa = 0$ and reaches the value 1 asymptotically for $\kappa \rightarrow \infty$). Therefore, a decrease of A_L with increasing temperature means, according to equation 4.3, that $\chi(0)$ decreases with increasing temperature, which is qualitatively expected from critical behavior.
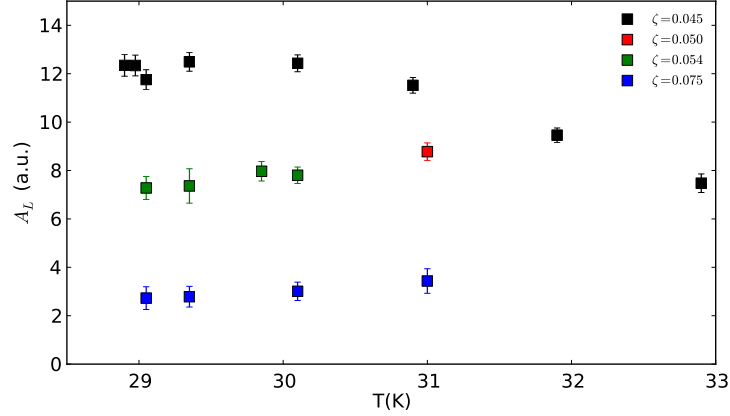
Figure 4.9: Plot of A_L versus temperature. Each color represents one value of ζ.

The temperature dependence of the linewidth Γ is plotted in figure 4.10, where each color represents one value of ζ. Γ increases with increasing ζ, in qualitative agreement with equation 4.5, as q increases with ζ. At constant ζ value, Γ decreases with increasing temperature. The data at $\zeta = 0.045$ shows the decrease with temperature only at the low temperatures, at high temperatures, Γ is independent of temperature. The data for $\zeta = 0.054$ and $\zeta = 0.075$ were only measured up to approximately 31 K and show a decrease with increasing temperature. This behavior is not in agreement with equation 4.5 and equation 4.4. Instead, according to the theory of weak itinerant ferromagnetism, an increase of Γ with increasing temperature is expected.
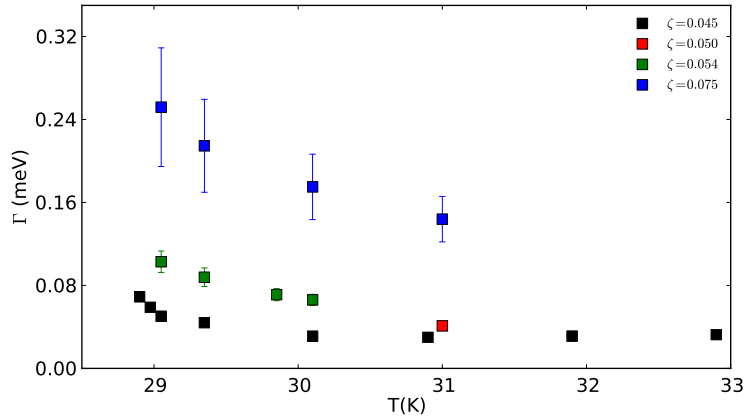

Figure 4.10: Linewidth Γ plotted versus temperature. Each color represents one value of ζ.

The parameter A_G, which is the amplitude of the shoulder as obtained by the Gaus-

sian fit, is plotted in figure 4.11 in dependence of the temperature, where each color represents one value of ζ. It decreases with increasing ζ. Furthermore, it decreases with increasing temperature, except the one for $\zeta = 0.054$, however, the error bars are so large that a decrease would still be within statistics for $\zeta = 0.054$. Both results are consistent with a magnetic origin of the shoulder, because the magnetic signal decreases rapidly with increasing temperature near T_c and because with increasing ζ, one is moving away from the magnetic Bragg peaks (see figure 4.2). We suppose that, at the low temperatures near $29\,\mathrm{K}$, the resolution function still picks up some signal from the magnetic diffraction peaks or from their tails and, at the higher temperatures, from the magnetic fluctuations, which are very strong close to the magnetic satellites. This is suggested by the fact that the qualitative behavior of the data at $\zeta = 0.045$ in figure 4.9 is similar to the corresponding data in figure 4.11. Both show a decrease with increasing temperature.
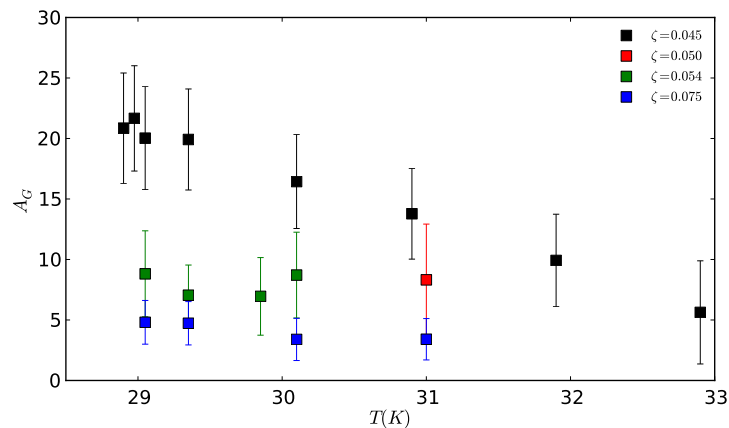
Figure 4.11: Plot of A_G versus temperature. Each color represents one value of ζ.

4.3 Measurement of $\mathrm{Mn}_{1-x}\mathrm{Fe}_x\mathrm{Si}$ at PANDA

In the following, the results are presented that were obtained in the measurements of $\mathrm{Mn}_{1-x}\mathrm{Fe}_x\mathrm{Si}$ with $x = 0.12$ at PANDA.

The wave vector of the scattered neutrons was $k_f = 1.3\,\text{\AA}^{-1}$, which corresponds to a neutron energy of $3.5\,\mathrm{meV}$. Both monochromator and analyzer were horizontally focusing. The measured energy resolution was $0.085\,\mathrm{meV}$.

In the experiment, the quasi-elastic spectra were measured at different constant q vectors at a temperature of $20\,\mathrm{K}$, which is considerably higher than the magnetic transition temperature $T_c = 6.5\,\mathrm{K}$, making sure that we are in the paramagnetic phase but still low enough to allow for clearly observable paramagnetic scattering.

Figure 4.12 illustrates schematically the reciprocal space near the nuclear (110) Bragg peak with the reciprocal space positions of the points where the quasi-elastic spectra are measured. The q vectors were all lying on the [110] crystalline direction. The reciprocal space positions were $Q = (1 + \zeta, 1 + \zeta, 0)$ with $\zeta = 0.04, 0.06, 0.07,$ $0.08, 0.095, 0.1, 0.125$ and 0.15. In contrast to pure MnSi, no discrete magnetic

peaks appear, instead, the magnetic scattering below T_c shows up on a ring (shown in red), which is the intersection of the horizontal plane with a sphere in reciprocal space. The reduced q vector q_{red} is defined as the distance between the reciprocal space position of the measurement point and the nearest point on the ring. The distance to the nuclear (110) Bragg peak shall be defined as q_{nucl}.
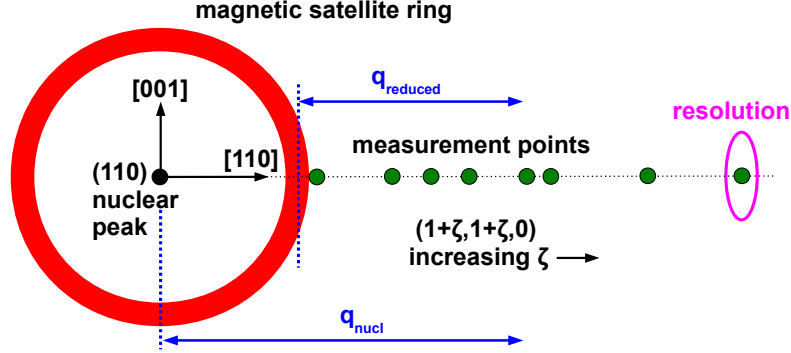
Figure 4.12: Schematic view of the reciprocal space near the nuclear (110) peak with the satellite ring and the positions of the points where the quasi-elastic spectra are measured. The ζ values are 0.04, 0.06, 0.07, 0.08, 0.095, 0.1, 0.125 and 0.15. The resolution is shown by the ellipse drawn in magenta.

Table 4.6 shows the ζ values, the corresponding q_{nucl} and q_{red}, and the temperature at which the measurements were carried out (which was always 20 K).

Table 4.6: Reciprocal space positions and temperatures of the measurements.

ζ	$q_{nucl}(\text{Å}^{-1})$	$q_{red}(\text{Å}^{-1})$	$T(\text{K})$
0.04	0.078	0.01	20
0.06	0.117	0.049	20
0.07	0.136	0.068	20
0.08	0.156	0.088	20
0.095	0.185	0.117	20
0.1	0.195	0.127	20
0.125	0.243	0.175	20
0.15	0.292	0.224	20

Figure 4.13 shows one of the measurements as an example. The raw data measured at 20 K is represented by the black triangles pointing upward. The background measurement is represented by the blue triangles pointing downward.

The background was measured at a high temperature of 80 K, far above T_c, to ensure that there is no magnetic contamination in the quasi-elastic spectra. In fact, we just assume that the data at 80 K shows the background. This implies that the large peak at zero energy, where the data at 20 K and the background at 80 K have virtually the same height, is due to a dominant incoherent scattering in Mn$_{1-x}$Fe$_x$Si. In case this assumption was wrong, and the large peaks at zero energy were produced by magnetic scattering at 20 K and 80 K, then equation 4.4 and equation 4.5 with a value of $T_c = 6.5$ K and a q of 0.01 Å^{-1} (to give just a qualitative approximation)

would predict that the linewidth of the data at 80 K would be more than five times larger than the linewidth at 20 K. But as this is obviously not the case here, we can assume that the data at 80 K really represents the background.

The elastic incoherent scattering is very dominant and is much bigger than any paramagnetic scattering. The reason that the incoherent scattering is much larger than in MnSi (compare to figure 4.3) is due to the large difference in neutron scattering lengths between Fe and Mn, as was already pointed out.

The points representing the background are fitted by a Gaussian (blue line). This Gaussian is then subtracted from the data shown in black, resulting in the difference data shown in red, which is the convolution of the instrument resolution with the Lorentzian line shape of the paramagnetic scattering. This difference data will be analyzed in the following.

Due to the fact that the incoherent scattering is so large, the background data (blue) around zero energy is virtually as high as the signal (black). Due to small uncertainties in the Gaussian fit of the background data, this can result in a difference signal that can have even negative intensities near zero energy (like in figure 4.13). Furthermore, the error bars of the difference signal near zero energy are very large. Therefore, the center part around zero energy is considered as worthless for our analysis, only the tails of the difference curves, where the Gaussian fit of the background almost drops to zero, might contain valuable information. Therefore, only the tails of the curve will be analyzed, whereas the center will be ignored.
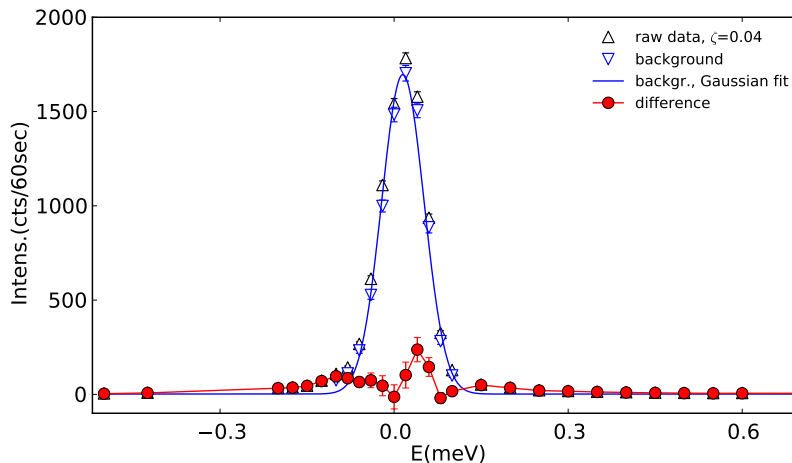

Figure 4.13: Raw data is shown by black triangles pointing upward, background data is shown by blue triangles pointing downward. The background is fitted by a Gaussian (blue line) which is then subtracted from the black data, resulting in the red difference data.

The cross section used was the same as for MnSi and is given by equation 4.1.

Then, a convolution fit in one dimension was done where only the energy resolution is considered. The parameterized Lorentzian curve is convoluted in each iteration step of the fitting procedure with the measured resolution curve, which is, in fact, the Gaussian fit of the background. The ideal procedure would be a four dimensional deconvolution in $(\mathbf{q}, \omega)$ space. However, as monochromator and analyzer were both focusing, a large number of instrument parameters (e.g., monochromator and

analyzer curvature) have to be known exactly for a correct calculation of the resolution (Popovici method). Unfortunately, these instrument parameters were not documented carefully enough. On the contrary, when having flat monochromator and analyzer, only the collimations in the four spectrometer arms are necessary for the calculation (Cooper Nathans method). But even in this case, it is known from practical use that, mostly, the calculated resolution cannot exactly predict the measured one [114]. In the case of focusing conditions, the prediction of the resolution might become even more unreliable due to the more complicated calculations with more instrument parameters.

The one-dimensional deconvolution in energy is demonstrated in figure 4.14. The symbols represent the data after subtracting the background, which is the same as the data shown in red in figure 4.13 (the data around zero energy is left out). The green line shows the energy resolution. The red line represents the Lorentzian cross section. The black curve is the convolution of the resolution with the cross section. It fits the black data. For a better visualization, all curves have the same height. One can see that the convolution (black curve) is only slightly wider than the cross section (red curve), because the energy resolution (green curve) is significantly narrower than the cross section. The very narrow energy resolution justifies that no four-dimensional deconvolution was carried out, as the effect of finite resolution can be neglected. Therefore, it is sufficient to directly fit the Lorentzian to the difference data, which will be done in the following.
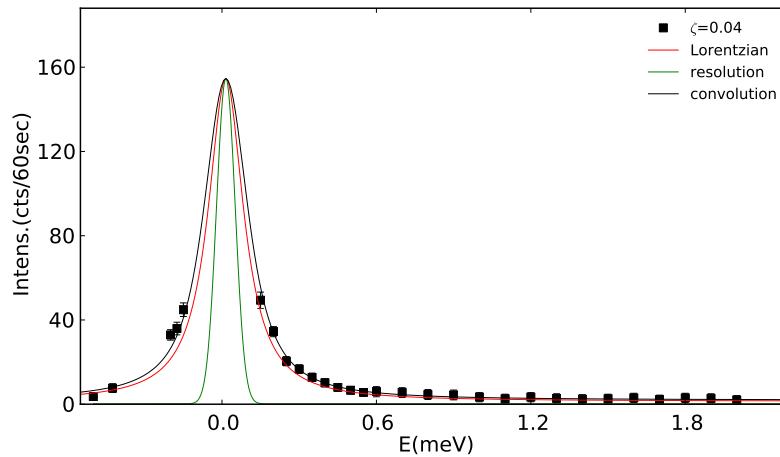
Figure 4.14: Black symbols: Data after background subtraction. Green line: Resolution. Red line: Lorentzian. Black line: Convolution of resolution with Lorentzian, which fits the black data.

Figure 4.15 shows the analysis for all values of ζ, which is increasing from (a) to (h). The black line is the fit to the data. One sees, that the linewidth increases with increasing ζ and that the height of the Lorentzian decreases with increasing ζ.

The values obtained in the fits are given in table 4.7. Also shown is the χ^2 of the fits.
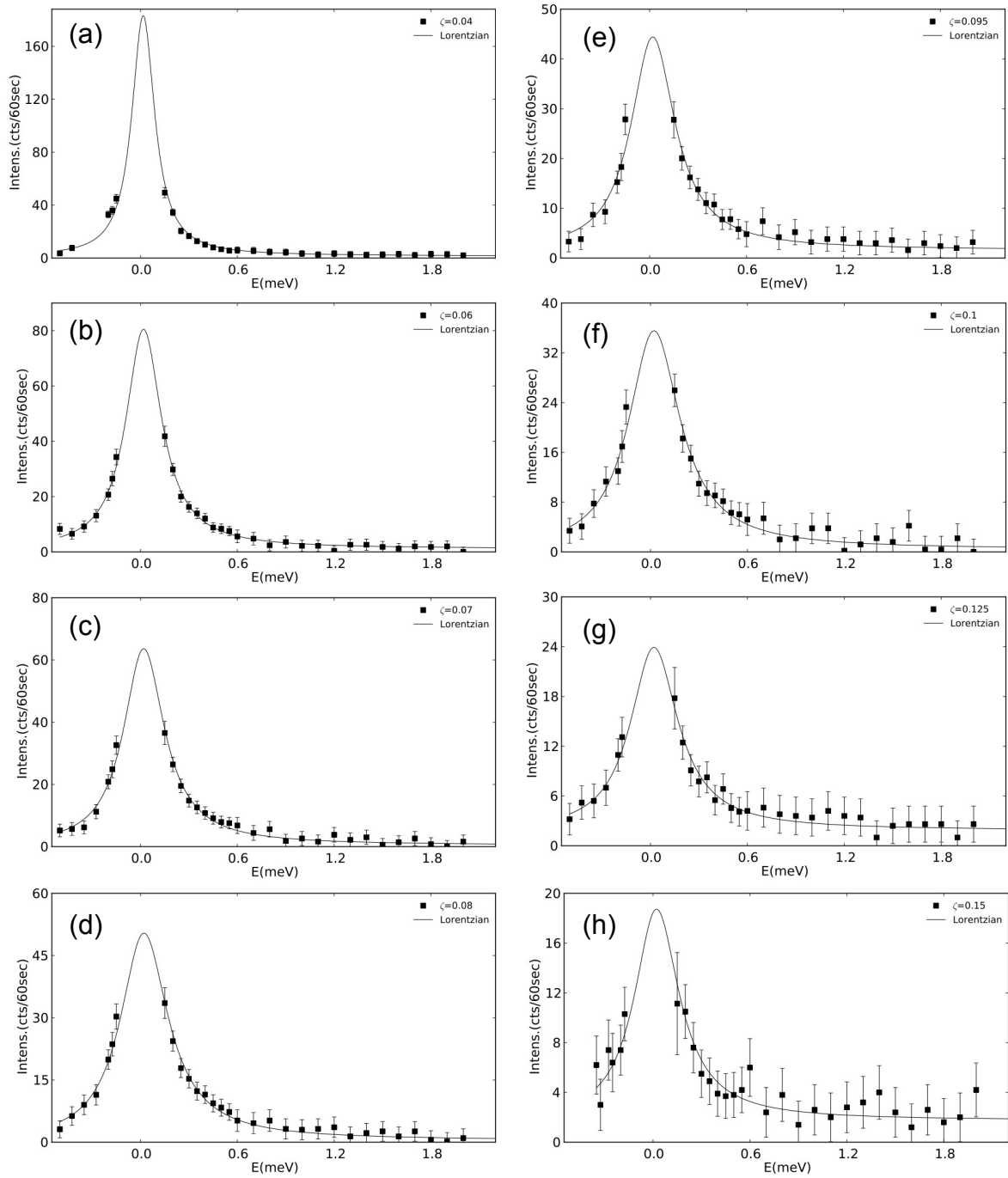
Figure 4.15: Black symbols: Data after background subtraction with rising ζ from (a) to (h). Black line: Lorentzian fit to the black data.

Table 4.7: Parameters obtained in the fits.

ζ	T(K)	A_L (a.u.)	Γ(meV)	χ^2
0.04	20	17.8±4.9	0.086±0.035	1.0
0.06	20	12.2±1.5	0.134±0.034	0.3
0.07	20	11.1±1.2	0.154±0.039	0.4
0.08	20	10.2±0.9	0.180±0.044	0.3
0.095	20	8.1±1.0	0.166±0.055	0.4
0.1	20	7.7±0.7	0.193±0.051	0.4
0.125	20	4.5±0.9	0.179±0.096	0.2
0.15	20	3.3±1.0	0.170±0.135	0.3

The values of A_L are plotted against q_{red} in figure 4.16. A_L decreases with rising q. This is in qualitative agreement with equation 4.3.
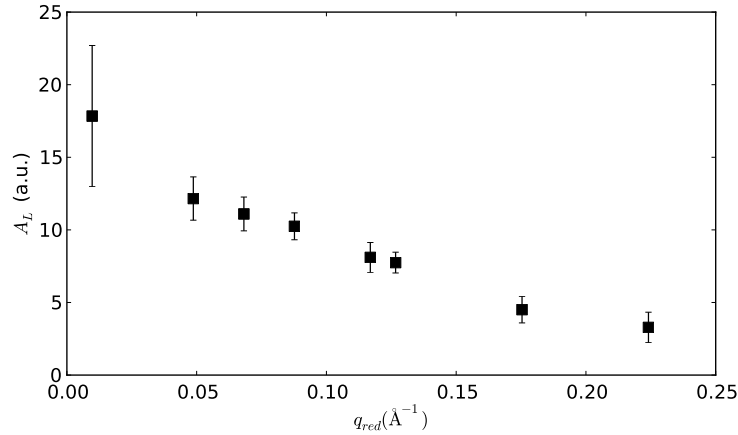
Figure 4.16: Plot of A_L versus q_{red}.

The values of Γ are plotted against q_{red} in figure 4.17. At lower values of q_{red}, the statistics is sufficient to determine an increase of Γ with rising q, which is in qualitative agreement with equation 4.5. At higher values of q_{red}, the statistics is very bad.
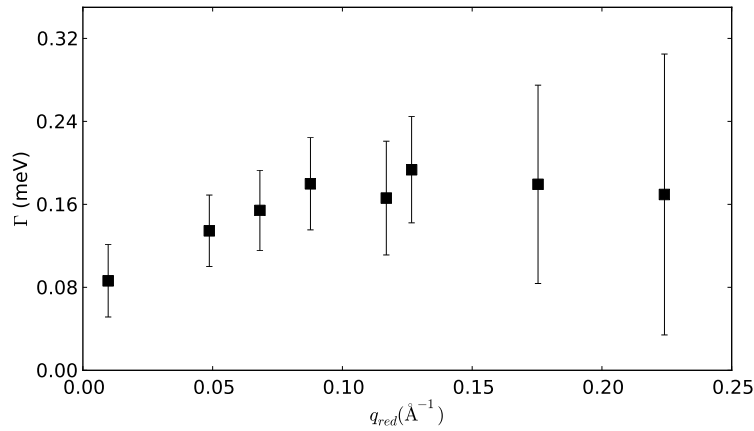
Figure 4.17: Linewidth Γ plotted versus q_{red}.

4.4   Discussion of the spin fluctuation measurements

The data of our measurements of the spin fluctuations in MnSi and $Mn_{1-x}Fe_xSi$ at PANDA will be discussed and, if possible, compared to the data taken in spin echo measurements at RESEDA (FRM II) by Tischendorf [9], to the data measured by Ishikawa *et al.* with triple axis spectrometry [5] [6], to the data measured by Pappas *et al.* (with spin echo) [7] and to the data obtained by Grigoriev *et al.* (also with spin echo) [8].

4.4.1 Analyzing the data for MnSi

The best way to test whether our data of MnSi is consistent with the formalism for isotropic ferromagnets given in equations 4.3 to 4.5, which was used by Ishikawa *et al.* in [5] and [6], is to examine data taken at identical temperature and to analyze the q dependence, because then, $\kappa(T)$, determined by equation 4.4, is a constant. When looking at table 4.1 or tables 4.2 to 4.5, we see that we have only at the temperatures $T_c + 0.15\,\text{K}$, $T_c + 0.45\,\text{K}$ and $T_c + 1.2\,\text{K}$ a series of three different q vectors.

We can now invert equation 4.3,

$$\frac{1}{A_L} = \frac{1}{\chi(0)} + \frac{q^2}{\kappa^2 \chi(0)}, \tag{4.7}$$

and plot $\frac{1}{A_L}$ versus q^2. Then, a fit of a regression line yields $\chi(0)$ and κ. This is done in figure 4.18, where we use q_{nucl} as q, and thus relate the momentum transfer to the nuclear peak. The regression line for each temperature is plotted using the same color as the data points. The fit parameters were $\chi(0)$ and κ. We see that the intersection of the regression lines with the y-axis is negative, which is physically not possible, as the amplitudes A_L cannot be negative.
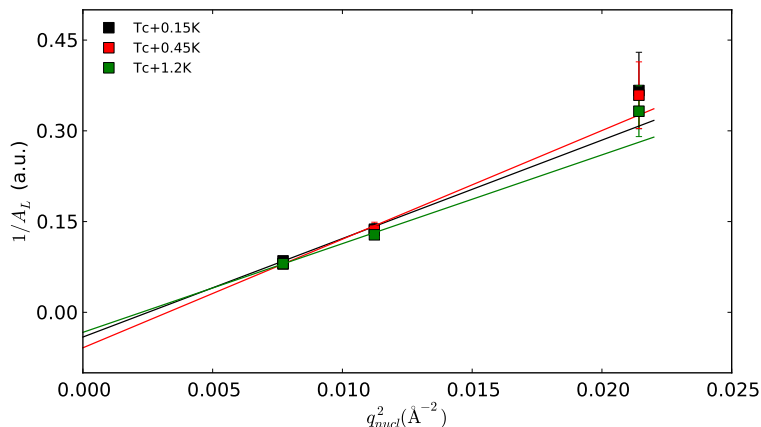
Figure 4.18: Inverse Lorentzian amplitude versus q_{nucl}^2 and regression lines.

Then, we tried the same, but this time using q_{red} as q, which is shown in figure 4.19. Now, the data is well fitted by regression lines with a positive intersection with the y-axis. Consequently, we assume that our data for MnSi is better described by relating the momentum transfer to the wave number of the helical pitch, using q_{red}. Furthermore, in all recent works on the fluctuations in MnSi [37] [7] [8] [9], q_{red} is taken as the physically relevant momentum transfer for a helimagnet.
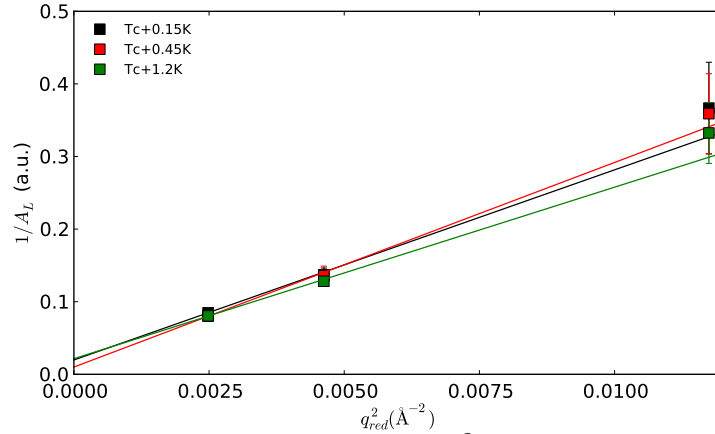
Figure 4.19: Inverse Lorentzian amplitude versus q_{red}^2 and fits according to equation 4.7.

The obtained $\chi(0)$ are plotted versus the normalized temperature T/T_c in figure 4.20. The error on the temperature axis was calculated by considering that T_c is only known with an accuracy of $\pm 0.2\,\mathrm{K}$. For a second order phase transition, like it is assumed for a ferromagnetic transition, $\chi(0)$ would have a singularity at $T = T_c$, i.e., it would be infinite. However, an increase of $\chi(0)$ when approaching $T/T_c = 1$ cannot be observed. This indicates that the phase transition is not purely second order, in agreement with the claim of [37] [7], where a more complex transition mainly of first order was proposed, involving a skyrmion liquid phase close to T_c. But in our measurement, the statistics is not sufficient to make a more precise statement in that respect.
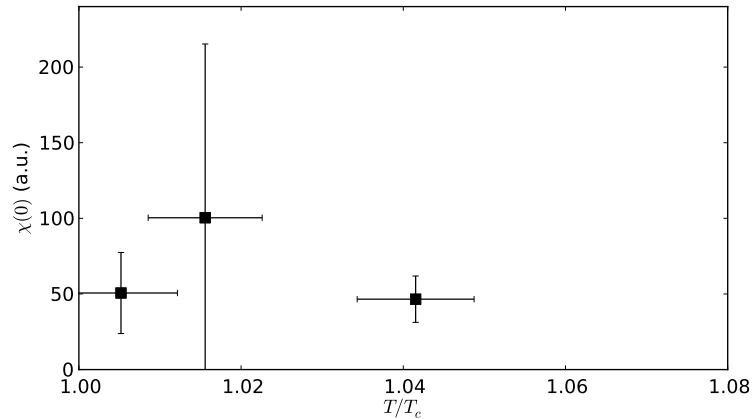
Figure 4.20: $\chi(0)$ versus normalized temperature.

Figure 4.21 displays the values of κ obtained in the fits in dependence of the normalized temperature T/T_c. The uncertainty in the temperature is the same as in figure 4.20. Additionally, the curve deduced from equation 4.4 is depicted, which was taken from Ishikawa *et al.*:

$$\kappa(T) = \kappa_0 \cdot \sqrt{\frac{T - T_c}{T_c}}. \tag{4.8}$$

Within statistics, our experimental values are roughly compatible with the curve determined by Ishikawa, however, they are not sufficiently accurate to prove the detailed dependence on T/T_c.
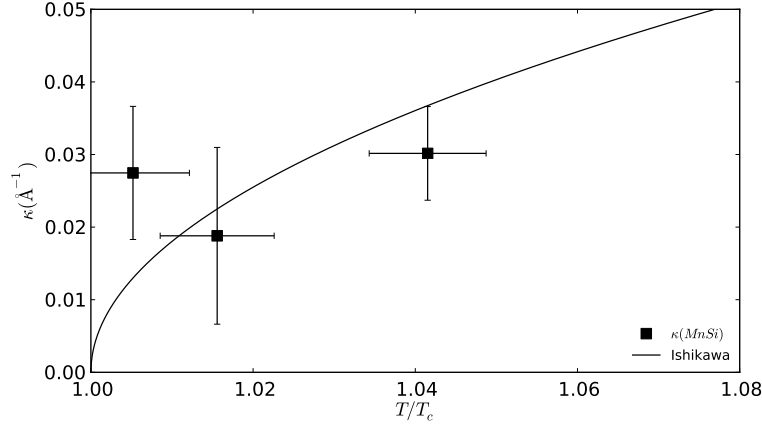
Figure 4.21: κ versus normalized temperature. The solid line represents the results of Ishikawa *et al.*.

The dependence of the Lorentzian linewidths Γ on the momentum transfer relative to the helical pitch, q_{red}, is plotted in figure 4.22, where each color represents one temperature. The solid lines drawn in the same colors as the data points represent fits of the data according to equation 4.5,

$$\Gamma(q) = \Gamma_0 \cdot q(\kappa^2 + q^2), \tag{4.9}$$

where q_{red} is used as q. The fit parameter was Γ_0. For the fits, the values of κ are taken from our measurements, i.e., they are the data points shown in figure 4.21. They have only small influence on the curves: this is shown by the dashed lines, which represent equation 4.9 with $\kappa = 0$ and the same Γ_0 as used for the solid lines. The resulting Γ_0 for each temperature are listed in table 4.8 in the second column. The values for $T_c + 0.15\,\mathrm{K}$ and $T_c + 0.45\,\mathrm{K}$ are coincident within statistics.
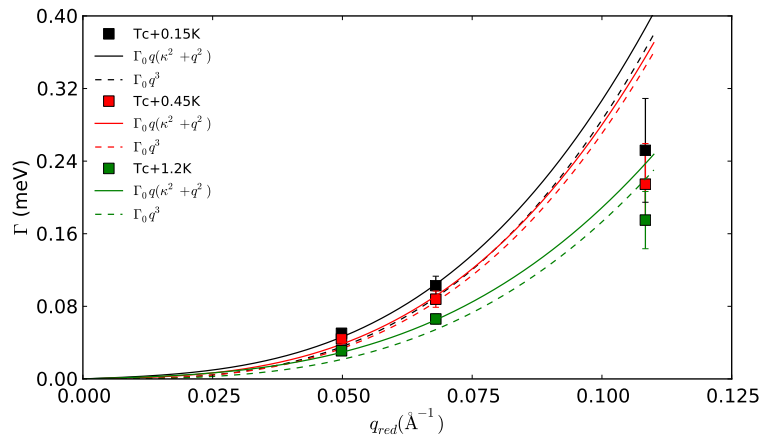
Figure 4.22: Linewidth versus q_{red} and fits according to equation 4.9.

In figure 4.23, we fitted, as a test, the same data as in figure 4.22 by the term

$$\Gamma(q) = \Gamma_0 \cdot q^z, \tag{4.10}$$

which represents dynamic scaling theory for a second order phase transition. The fit parameters were Γ_0 and the exponent z. The resulting values of Γ_0 and z are presented in table 4.8 in the third and fourth column. When comparing figures 4.22 and 4.23 we see, that the data can be better fitted by equation 4.10. The fit

curves in figure 4.22 are dominated by the q^3 dependence, whereas the fit curves in figure 4.23 show a q^z dependence with $z < 3$ (given in the fourth column of table 4.8). Within statistics, a value of $z = 2.5$ would be possible, which is the exponent expected, e.g., for the Heisenberg local moment magnetism and also for itinerant ferromagnets at large length scales.
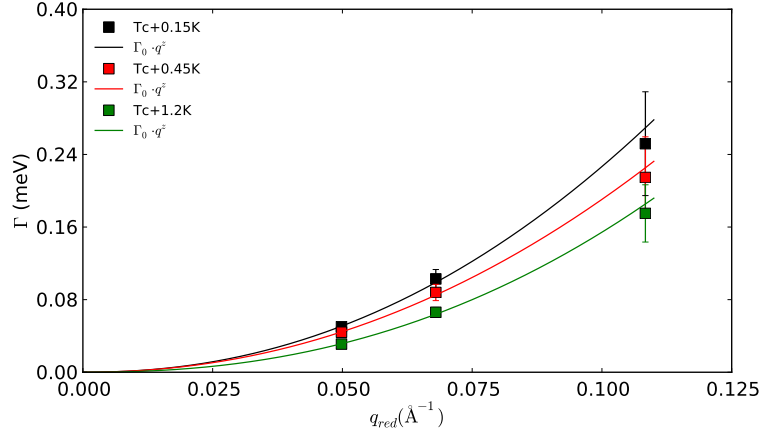
**Figure 4.23:** Linewidth versus q_{red} and fits according to equation 4.10.

Table 4.8: Parameters obtained by fitting equation 4.9 and 4.10 to our PANDA data.

	$\Gamma_0 \cdot q_{red}(\kappa^2 + q_{red}^2)$	$\Gamma_0 \cdot q_{red}^z$	
T(K)	Γ_0(meV Å^3)	Γ_0(meV Å^z)	z
$T_c + 0.15$	285.4 ± 15.6	31.9 ± 22.8	2.15 ± 0.25
$T_c + 0.45$	270.5 ± 14.4	23.4 ± 16.0	2.09 ± 0.24
$T_c + 1.2$	173.0 ± 8.6	29.7 ± 17.8	2.28 ± 0.21

We will now compare the linewidths determined in our measurements at PANDA with the linewidths obtained by Ishikawa *et al.* in 1982 and 1985 [5] [6], because they were also obtained with triple axis spectroscopy. As the temperatures and q values at which the measurements were conducted differ between the experiments, we cannot directly compare values at same temperatures or q values. Instead, in figure 4.24, where the linewidth is plotted against q_{nucl}, we display all values near T_c for a comparison of the measurements. The value of $T_c = 29.0$ K determined by Ishikawa is almost coincident with the value $T_c = 28.9$ K determined in our experiment. We use q_{nucl} instead of q_{red} because Ishikawa related the momentum transfers to the nuclear peak, i.e., he neglected the helimagnetic nature of MnSi by treating it like an isotropic ferromagnet. The triangular symbols show the data obtained by Ishikawa *et al.* between the temperatures 31 K to 34 K. Our data from PANDA, which were taken at similar temperatures, are represented by the circles shown in red. We display all of our values, not only the values shown in figure 4.22 and 4.23. In the latter, only the data were shown that can be aligned to series of different q vectors at constant temperature.

The green line represents the q dependence according to equation 4.9 with a value of $\Gamma_0 = 50.0$ meV Å^3 as it was determined by Ishikawa [6]. For κ, we took the value calculated by $\kappa(T)^2 = \kappa_0^2 \cdot \frac{T - T_c}{T_c}$ (equation 4.4) inserting $T = T_c$, i.e., $\kappa^2 = 0$. The dashed green line also represents equation 4.9 with the same value of Γ_0 as the solid

green line, but with κ^2 calculated for $T = T_c + 4\,\mathrm{K}$, because the highest temperature values shown in figure 4.24 were taken at approximately $4\,\mathrm{K}$ above T_c. The solid blue line and the dashed blue line represent the same equations as the green lines but for a value of $\Gamma_0 = 60.8\,\mathrm{meV}\ \mathrm{\AA}^3$ [6]. Ishikawa proposed a value of Γ_0 between $\Gamma_0 = 50.0\,\mathrm{meV}\ \mathrm{\AA}^3$ and $\Gamma_0 = 60.8\,\mathrm{meV}\ \mathrm{\AA}^3$. We see that most of the data points lie within these lines. This means that our data measured at PANDA roughly agrees with the data measured by Ishikawa.
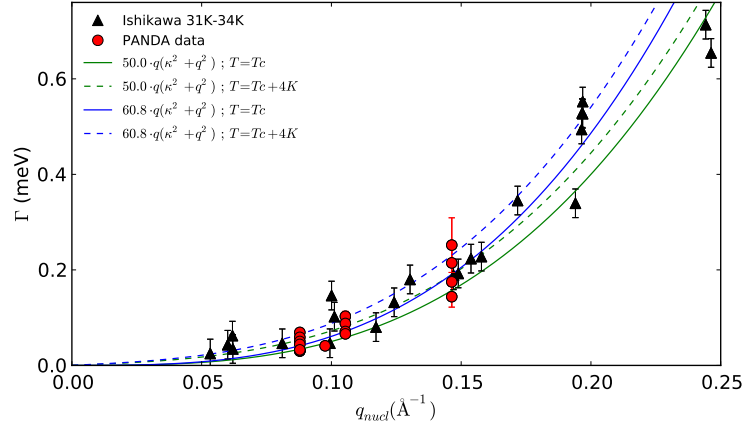
Figure 4.24: Linewidths obtained by Ishikawa *et al.* and our PANDA measurements plotted versus q_{nucl}. The solid green and blue lines represent the theory of itinerant ferromagnets for $T = T_c$ with a value of $\Gamma_0 = 50.0\,\mathrm{meV}\ \mathrm{\AA}^3$ and $\Gamma_0 = 60.8\,\mathrm{meV}\ \mathrm{\AA}^3$ respectively. The dashed lines represent $T = T_c + 4\,\mathrm{K}$.

However, when we plot the PANDA data from figure 4.24 in dependence of the temperature in figure 4.25, where each value of q_{nucl} is represented by a different color, we see that the linewidth at constant q vector decreases with increasing temperature and levels off at large temperature (see the data in black). This decrease of the linewidth is not consistent with the theoretical model of itinerant ferromagnetism represented by equations 4.3 to 4.5, as $\kappa(T)$ would increase with increasing temperature (see equation 4.4) and consequently $\Gamma(T)$ would increase (see equation 4.5). The decrease of the linewidth with increasing temperature can also be seen in the data shown in figures 4.22 and 4.23.
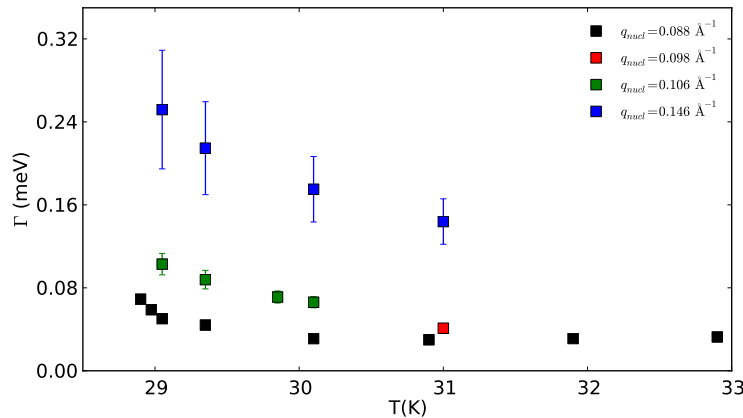
Figure 4.25: Linewidths obtained in our measurements at PANDA for all values of q_{nucl} (cf. figure 4.24) in dependence of temperature.

Figure 4.26 shows the same data as figure 4.24 but with the linewidths plotted versus $q(\kappa^2 + q^2)$ using q_{nucl} as q. Therefore, the green line and the blue line in figure 4.24 appear now as straight lines. Roughly, the data is in qualitative accordance with the theory represented by the green and blue line, as was already pointed out when discussing figure 4.24. However, as we saw in figure 4.25, the temperature dependence of our PANDA data does not behave like expected from the theory, and therefore, the data points shown in red, which represent our data, do not lie exactly on a straight line (neither does the data obtained by Ishikawa shown in black).
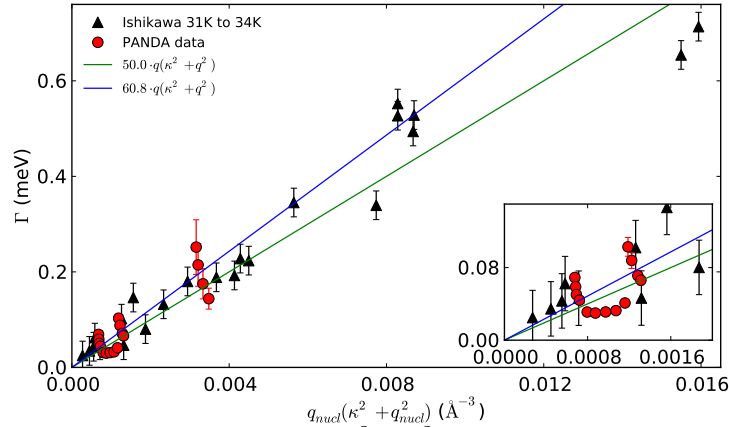
Figure 4.26: Linewidth plotted versus $q(\kappa^2 + q^2)$ using q_{nucl} as q. The solid green and blue lines represent the same curves as in figure 4.24.

We will now compare our data measured at PANDA to the data obtained in spin echo measurements by Tischendorf (at RESEDA) [9], by Pappas *et al.* [7] and by Grigoriev *et al.* [8].

Figure 4.27 displays the data from the measurements on RESEDA together with the data obtained by Pappas and Grigoriev that were measured at similar temperatures. Pappas and Grigoriev measured at very low values of q_{red}. The value of T_c determined in the RESEDA measurements was the same as the value determined in our PANDA measurements ($T_c = 28.9 \, \text{K}$). The values of T_c determined by Pappas were, depending on the used cryostat and thermometry, $28.60 \, \text{K}$ or $29.05 \, \text{K}$ and thus roughly coinciding with the value determined in the RESEDA experiment. The transition temperature T_c determined by Grigoriev *et al.* was, depending on the used cryostat and thermometry, $28.80 \, \text{K}$ or $29.05 \, \text{K}$ and thus roughly coinciding with the T_c determined by Pappas. Comparable temperatures are shown by the same colors. The data shown in black, taken very close to T_c, is consistent between RESEDA, Pappas and Grigoriev. The data shown in green, which represents temperatures of $1.4 \, \text{K}$ and $1.2 \, \text{K}$ above T_c, demonstrate that the measurements on RESEDA are consistent with the measurements conducted by Pappas.
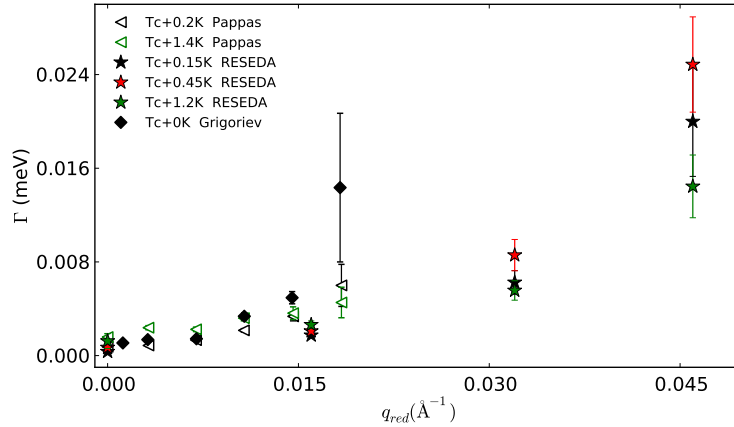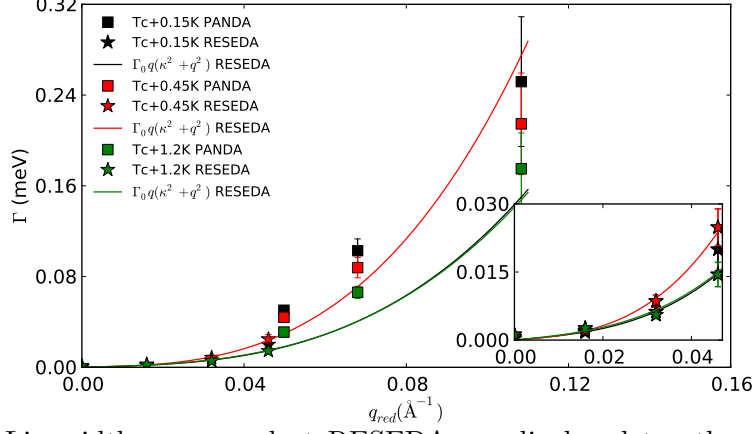
Figure 4.27: Data measured at RESEDA is displayed together with data measured by Pappas *et al.* and by Grigoriev *et al.*. Similar temperatures are shown by the same color.

Now, we compare our data measured at PANDA with the data obtained at RESEDA. Figure 4.28 shows the PANDA data by the quadratic symbols and the RESEDA data by the star-shaped symbols. Same temperatures are represented by the same colors. The lines drawn in the same colors (caution: the green and black line almost coincide) are fits of the RESEDA-data according to equation 4.9, where Γ_0 was fitted. The values of κ are the same as in figure 4.22, they are taken from figure 4.21. Our PANDA data roughly extends the RESEDA data to higher q values. However, there is a small shoulder between the two data sets, which is probably due to systematic errors of unknown origin. The resulting values of Γ_0 are shown in table 4.9 in the second column. When we compare them to the values obtained from our PANDA data in the second column of table 4.8, we see that the values derived from the RESEDA data are of the same order of magnitude but considerably smaller. The systematic error between the two data sets might contribute to a large extent to the discrepancies.

When looking at the RESEDA data (see the inset), we notice that the linewidths at same q vectors do not increase monotonically with increasing temperature, instead, the data at $T_c + 0.45\,\mathrm{K}$, shown in red, has the largest linewidths at the two largest q vectors. So, neither the PANDA data nor the RESEDA data show a monotonic increase of the linewidth with increasing temperature, in discrepancy to the theory of itinerant ferromagnetism. However, the RESEDA data is well fitted by this theory (equation 4.9).

Figure 4.28: Linewidths measured at RESEDA are displayed together with our data measured at PANDA. The lines are fits of equation 4.9 to the RESEDA data.

As a test, the RESEDA data was also fitted by equation 4.10, which is shown in figure 4.29. The fit parameters were Γ_0 and the exponent z. Like in figure 4.28, the data could be well fitted. The resulting values are given in table 4.9 in the third and fourth column. Some of the values are similar to the corresponding values obtained from our PANDA data given in table 4.8, but others differ considerably. Also here, the systematic error represented by the small shoulder between the two data sets might contribute to a large extent to the discrepancies.
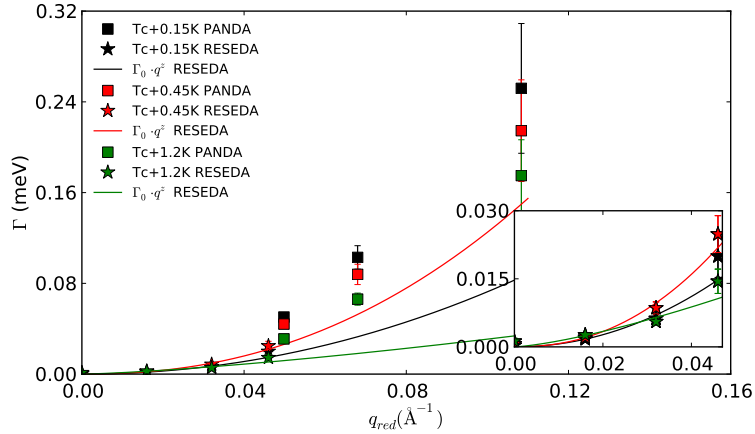
Figure 4.29: Linewidths measured at RESEDA are displayed together with our data measured at PANDA. The lines are fits of equation 4.10 to the RESEDA data.

Table 4.9: Parameters obtained by fitting equation 4.9 and 4.10 to the RESEDA data.

$T(\mathrm{K})$	$\Gamma_0 \cdot q_{red}(\kappa^2 + q_{red}^2)$	$\Gamma_0 \cdot q_{red}^z$	
	$\Gamma_0(\mathrm{meV\ \mathring{A}^3})$	$\Gamma_0(\mathrm{meV\ \mathring{A}^z})$	z
$T_c + 0.15$	110.8 ± 9.1	8.1 ± 6.8	2.05 ± 0.22
$T_c + 0.45$	209.8 ± 16.0	22.0 ± 14.8	2.24 ± 0.18
$T_c + 1.2$	107.7 ± 9.3	0.7 ± 0.6	1.37 ± 0.22

Conclusion of the measurements of MnSi

We started the discussion by analyzing the inverse Lorentzian amplitudes. As they were lying on a straight line, we could apply the model represented by equations 4.3 to 4.5 by fitting equation 4.3. By comparing figure 4.18 and 4.19, we concluded that the physically relevant moment transfer in a helimagnetic material has to be related to the helical pitch. Consequently, we used q_{red} in the further discussion. This is also done in all recent works on the fluctuations in MnSi [37] [7] [8] [9]. But in fact, the situation might be more complicated. For example, one could assume that, instead of a single q vector (like q_{red}), all q vectors of the sphere in reciprocal space (with a radius equal to the helical pitch) contribute. This sphere is represented in figure 4.2 by the dashed red line, which depicts the intersection of the sphere with the horizontal scattering plane.

The temperature dependence of $\chi(0)$ visualized in figure 4.20 indicates that the transition from the helimagnetic phase to the paramagnetic phase is not second order. The temperature dependence of κ given in figure 4.21 is not conclusive.

The q dependence of the linewidth in figure 4.22 cannot prove the model of itinerant ferromagnetism represented by equations 4.3 to 4.5, the fits are not of good quality. Better results can be obtained by the fits in figure 4.23 where dynamic scaling theory for a second order phase transition was applied. The exponent z gets near to 2.5, which would be expected for a local moment Heisenberg ferromagnet or an itinerant ferromagnet on large length scales. Our values of z are slightly lower than 2.5, which is compatible with a behavior between antiferromagnetism, where $z = 1.5$, and ferromagnetism with $z = 2.5$. This is consistent with the fact that helimagnetism has both ferromagnetic and antiferromagnetic components.

Figure 4.24 and 4.26 prove that our data is consistent with the data of Ishikawa. Roughly, our data and the data from Ishikawa are compatible with the theory, as the data points in these two figures are near to the drawn lines. But when looking at the temperature dependence of our data in figure 4.25, we see a decrease of the linewidth with increasing temperature, in discrepancy to the theory.

Lonzarich and Taillefer [18] developed a model for ferromagnetic materials in which additionally to SCR theory both longitudinal and transversal low energy spin fluctuations are taken into account. The dependence of the linewidth on q derived by this model is

$$\Gamma(q) = \hbar\gamma q(\chi^{-1} + cq^2), \tag{4.11}$$

which is identical to equation 4.5 when $\Gamma_0 = \hbar\gamma c$ and $\kappa^2 = \frac{\chi^{-1}}{c}$. The parameter c represents the spin wave stiffness. Lonzarich and Taillefer inferred values of $\hbar\gamma = 2.6 \cdot (4\pi)\,\mu\text{eV\AA}$ and $c = 2.1/(4\pi) \cdot 10^4\,\text{\AA}^2$ from the measurements of Ishikawa (the factor (4π) comes from the conversion of cgs units used in [18] to SI units). This leads to a value of $\Gamma_0 = 54.6\,\text{meV \AA}^3$, which is compatible with figures 4.24 and 4.26. The values of the parameters γ, c and χ were measured by Bauer *et al.* [109] by measurements of the magnetization and susceptibility, and the values are roughly compatible to the values of Lonzarich and Taillefer and therefore also to the measurements of Ishikawa. As our data is compatible to the data of Ishikawa, this means that our data is roughly consistent with the bulk measurements of Bauer *et*

al..

Although our data extends the data from RESEDA to higher q values, there are discrepancies between the two data sets. This is seen in figures 4.28 and 4.29 and by comparing tables 4.8 and 4.9. The difference of the fit results between the two data sets might be caused by the small systematic error seen by the shoulder in figures 4.28 and 4.29. But also physical reasons can be responsible: The q dependence of the linewidth probably varies between different q ranges. At low q vectors, the helimagnons discovered in [82] or chiral interactions in general might determine the behavior. At large q vectors (i.e. small length scales), the material might be described like an isotropic ferromagnet. However, the systematic error, the insufficient statistics of the data and the small number of data points make precise statements in that respect impossible. We see for example that the RESEDA data can be fitted by the model of itinerant ferromagnetism (figure 4.28) and also by dynamic scaling theory (figure 4.29), thus we cannot determine which of the models is better.

The discrepancies of the data to the model of itinerant ferromagnetism demonstrate that a new theoretical model is needed where the influence of the helimagnons or chiral interactions are included.

4.4.2   Analyzing the data for $Mn_{1-x}Fe_xSi$

All our data on $Mn_{1-x}Fe_xSi$ was measured at a temperature of $20\,K$, i.e. deep in the disordered phase. The inverse Lorentzian amplitude obtained in our experiment is plotted versus q_{red}^2 in figure 4.30. The straight line is a fit according to equation 4.7, with $\chi(0)$ and κ as free fit parameters. The fit yields $\chi(0) = 15.0 \pm 3.2\,a.u.$ and $\kappa = 0.13 \pm 0.04\,\text{Å}^{-1}$.
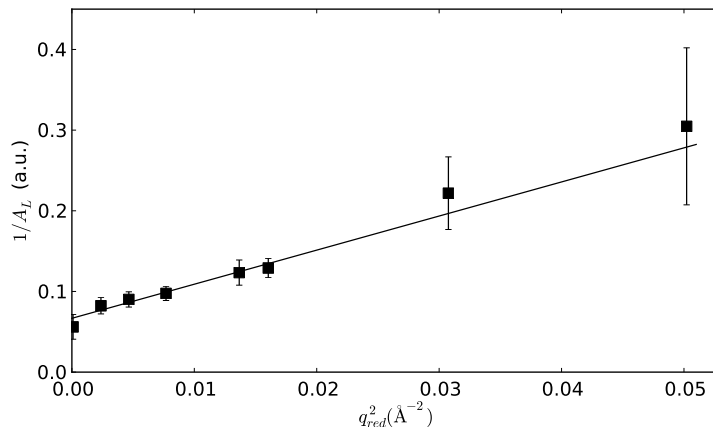
Figure 4.30: Inverse Lorentzian amplitude versus q_{red}^2 and fit according to equation 4.7.

In figure 4.31, the linewidth is plotted versus q_{red}. The circular black symbols represent our data measured at PANDA at $20\,K$. Only the four data points at the lowest q values, which have good statistics, were fitted by equation 4.9, because we suspect that the background subtraction at the low scattering intensities (at large q_{red}) is prone to systematic errors. The value for κ is taken from the fit in figure 4.30. The free fit parameters were Γ_0 and an additional vertical offset $\Gamma(q_{red} = 0)$ not

included in equation 4.9. The resulting fit is represented by the black line. We note a pronounced vertical offset. The red triangular data points represent the data taken on RESEDA by Tischendorf [9] at a temperature of $6.85\,\mathrm{K}$, and the green x shaped data points represent the data taken on RESEDA at $7.33\,\mathrm{K}$. The temperatures at the RESEDA experiments were slightly above the transition temperature of $\mathrm{Mn}_{1-x}\mathrm{Fe}_x\mathrm{Si}$, which is $6.5\,\mathrm{K}$. The red and green lines show the respective fits of the RESEDA data according to equation 4.9, where the fit parameters were Γ_0, κ and an additional vertical offset. We note that the data taken at RESEDA near T_c shows only a very small, almost negligible vertical offset.

The values of Γ_0 and κ obtained in all three fits of figure 4.31 are given in table 4.10 in the second and third column (the κ-value for the PANDA-data at $20\,\mathrm{K}$ was obtained in the fit of figure 4.30). The values of Γ_0 have large uncertainties and are lower than the Γ_0 values of MnSi given in the second column of table 4.8 or 4.9. The values for κ determined by the RESEDA-data have huge uncertainties, which means that they cannot be trusted, i.e., κ cannot be extracted from the fits. The vertical offsets $\Gamma(0)$ are given in table 4.11 in the second column. The offset at $20\,\mathrm{K}$ is considerable, whereas the offsets at the lower temperatures are statistically almost negligible.
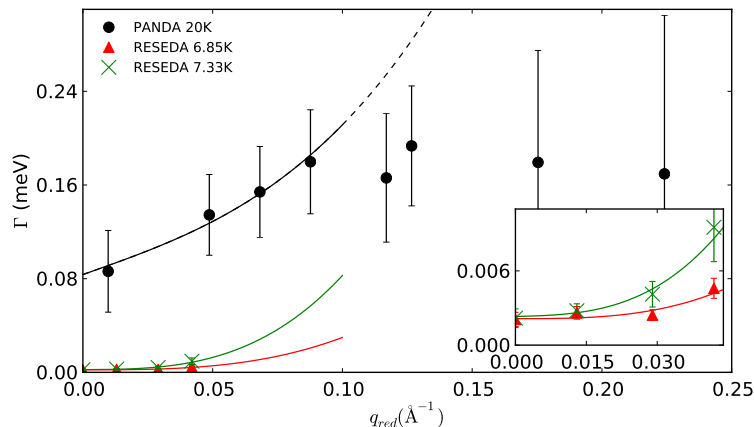
Figure 4.31: Linewidth versus q_{red} and fits according to equation 4.9. For the fit of the PANDA data, the value of κ was fixed.

In figure 4.32, we fitted, as a test, the same data as in figure 4.31 by equation 4.10. The free fit parameters were Γ_0, the exponent z and an additional vertical offset $\Gamma(0)$. The resulting vertical offsets are almost the same as determined in the fits in figure 4.31, as can be seen in the third column of table 4.11. The resulting values of Γ_0 and z are given in table 4.10 in the fourth and fifth column. The values of the exponent for the RESEDA-data are much higher than the value of the PANDA-data. All values of z have huge uncertainties. Moreover, they are unphysical, as the highest possible exponent is the one expected from the model of itinerant ferromagnetism with $z \approx 3$ (see equation 4.5). The values of Γ_0 also have huge uncertainties. This means that we cannot obtain trustworthy information from the fits.
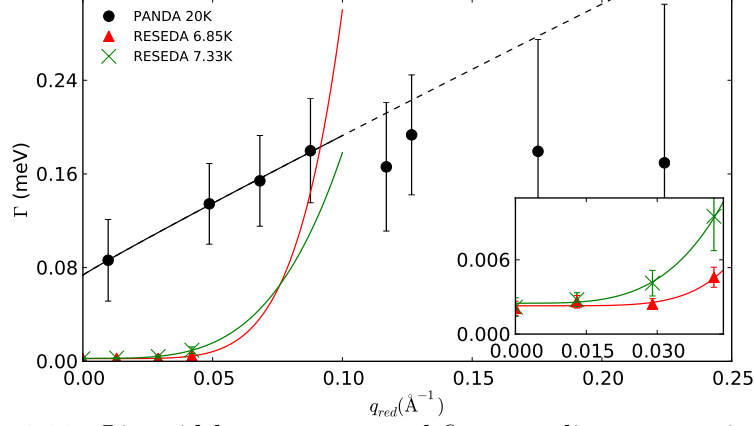
Figure 4.32: Linewidth versus q_{red} and fits according to equation 4.10.

We state that all the fits shown in figure 4.31 and 4.32 are excellent, but no trustworthy information can be obtained from the fits because the statistics is too bad and because the number of data points is very small. Moreover, for the fit of the 20 K-data the data points at higher q values were not taken into account as they have large errors and are thus not considered as trustworthy.

**Table 4.10:** Parameters obtained by fitting equation 4.9 and 4.10.

	$\Gamma_0 \cdot q_{red}(\kappa^2 + q_{red}^2)$		$\Gamma_0 \cdot q_{red}^z$	
	Γ_0(meV Å^3)	κ(Å^{-1})	Γ_0(meV Å^z)	z
RESEDA 6.85 K	27.6±12.0	$1.3 \cdot 10^{-6} \pm 0.9 \cdot 10^{-6}$	$1.3 \cdot 10^5 \pm 2.3 \cdot 10^6$	5.64±5.56
RESEDA 7.33 K	79.4±55.4	0.011±0.084	949.9±6558.8	3.73±2.12
PANDA 20 K	49.6±28.1	0.13±0.04	1.1±4.9	0.96±2.06

Table 4.11: Vertical offsets $\Gamma(0)$ obtained in the fits.

	$\Gamma_0 \cdot q_{red}(\kappa^2 + q_{red}^2)$	$\Gamma_0 \cdot q_{red}^z$
	$\Gamma(0)$(meV)	$\Gamma(0)$(meV)
RESEDA 6.85 K	0.002±0.001	0.002±0.001
RESEDA 7.33 K	0.002±0.001	0.002±0.001
PANDA 20 K	0.084±0.034	0.074±0.086

In figure 4.33, the κ values determined in Mn$_{1-x}$Fe$_x$Si (red symbols) are plotted together with the κ values determined in MnSi (black symbols) versus the normalized temperature T/T_c. The values of κ for MnSi were already displayed in figure 4.21, but as the temperatures at which the Mn$_{1-x}$Fe$_x$Si sample was measured were considerably higher than T_c in Mn$_{1-x}$Fe$_x$Si, the diagram had to be extended compared to figure 4.21 to higher values of T/T_c, and consequently, the data for MnSi appears very close to $T/T_c = 1$ in this scaling. The black line is the curve determined by Ishikawa *et al.* for MnSi (see equation 4.8), which was already shown in figure 4.21. The κ values for Mn$_{1-x}$Fe$_x$Si at higher T/T_c do not lie on the black curve. This does not imply that we expected them to lie on the curve, as the correlation length in the highly disordered compound Mn$_{1-x}$Fe$_x$Si might behave very differently to the one in MnSi. Anyway, it was already pointed out when discussing figure 4.31 that

the κ-values in $Mn_{1-x}Fe_xSi$ (namely for the RESEDA data) could not be obtained with the desired accuracy.
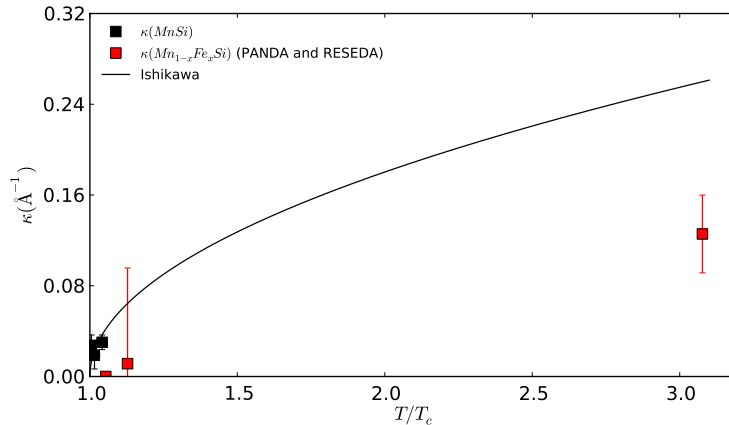
Figure 4.33: κ versus normalized temperature and curve determined by Ishikawa *et al.*. Data for MnSi is shown by the black symbols and data for $Mn_{1-x}Fe_xSi$ by the red symbols.

Conclusion of the measurements of $Mn_{1-x}Fe_xSi$

In summary, we analyzed the Lorentzian amplitudes and the linewidths of $Mn_{1-x}Fe_xSi$ within the same theoretical framework as the data for MnSi.

The inverse Lorentzian amplitudes in figure 4.30 are consistent with the model represented by equations 4.3 to 4.5 because they are on a straight line. However, the analysis of the linewidths revealed that the data is too scarce to allow for precise conclusions. The data at $20\,K$, which was obtained at PANDA, is of particularly poor quality, as the measurements were hampered by the large incoherent scattering in $Mn_{1-x}Fe_xSi$. We obtained reasonable fits in figures 4.31 and 4.32 (but with huge uncertainties of the resulting fit parameters) although we applied two different models, equation 4.9 and 4.10. This means that we were not able to prove the applicability of the theory of itinerant ferromagnets represented by equations 4.3 to 4.5 to the case of $Mn_{1-x}Fe_xSi$.

An interesting peculiarity we were able to detect is the sizable vertical offset at $20\,K$ and the fact that at the low temperatures ($6.85\,K$ and $7.33\,K$) it is virtually zero. This vertical offset might be interpreted as the linewidth at the magnetic satellite position (i.e. at $q_{red} = 0$), but we are not able to clarify its origin. Its temperature dependence might be explained by a still unidentified damping mechanism that increases with temperature. It was proposed already for MnSi in [37] and [7] that near T_c the material could be in some sort of intermediate, not yet paramagnetic, state involving some kind of skyrmion liquid. In $Mn_{1-x}Fe_xSi$, this intermediate state becomes more pronounced. But by our measurements on $Mn_{1-x}Fe_xSi$ we cannot resolve whether this is in any way linked to the damping mechanism that probably gives rise to the vertical offset.

We pointed out that for MnSi a new theoretical model is required where the influence of chiral interactions is included. The same holds for $Mn_{1-x}Fe_xSi$.

4.5   Measurement of $Mn_{1-x}Fe_xSi$ at TASP

Now, it was intended to measure possible helimagnons in $Mn_{1-x}Fe_xSi$ to compare to the helimagnons measured in pure MnSi [82]. The measurement was carried out at the triple axis spectrometer TASP at PSI.

The wave vector of the scattered neutrons was $k_f = 1.5\,\text{Å}^{-1}$, which corresponds to a neutron energy of $4.66\,\text{meV}$. The measured energy resolution was $0.22\,\text{meV}$.

In the experiment, quasi-elastic spectra were measured at the position of the nuclear (110) Bragg peak at different temperatures. The reason for that is explained by figure 4.34. The horizontal plane is spanned by the crystalline [110] direction and the [001] direction. The vertical axis represents the energy with arbitrary units. The ring shown by the red dashed line represents the intersection of the horizontal scattering plane with the sphere in reciprocal space where the scattering intensity is distributed on. The red points are the intersection of the [110] axis with the ring. When assuming dispersions of the helimagnons with zero point at the sphere (blue lines), then all dispersions from all points of the sphere would add up at the nuclear (110) Bragg peak where they would intersect at the same energy transfer, thus resulting in a large inelastic peak or several peaks, when there are several dispersions, at certain energy transfers [82].
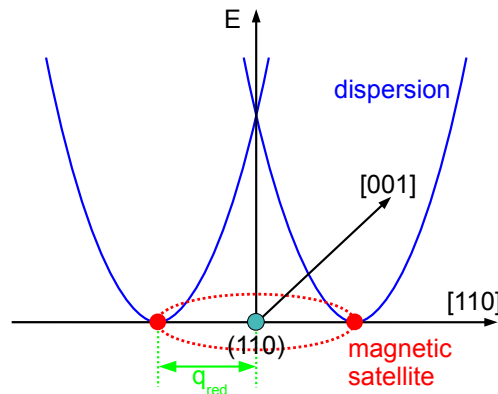
Figure 4.34: Dispersion relations are schematically shown that evolve from the points of the sphere represented by the ring (dashed red line). The dispersions from all points of the sphere would intersect at the position of the nuclear (110) peak at the same energies, thus giving a large inelastic signal. q_{red} is indicated.

Table 4.12 shows q_{nucl}, q_{red} and the temperatures where the measurements were done.

Table 4.12: Reciprocal space positions and temperatures of the measurements.

$q_{nucl}(\text{Å}^{-1})$	$q_{red}(\text{Å}^{-1})$	$T(\text{K})$
0	0.078	1.5
0	0.078	4
0	0.078	7
0	0.078	12
0	0.078	100

Figure 4.35 shows the obtained data at all temperatures. Only the inelastic tails are shown. The peak center at zero energy (the actual nuclear Bragg peak) is omitted. Originally, the high temperature scan at 100 K was intended as the background scan. But it shows the largest inelastic signal of all scans. The transition temperature in Mn$_{1-x}$Fe$_x$Si is $T_c = 6.5$ K. The data measured above T_c was treated like spin fluctuations by fitting equation 4.1. At low temperatures in (a), (b) and (c), we see a spurion at the two lowest energy values. It vanishes above T_c and is not visible in (d) and (e). Thus, it can be considered as of magnetic origin. The scales are the same in all diagrams except for (e), where the intensity-scale was extended because of the larger signal.

In (a) and (b), where we measured at $T < T_c$, inelastic features are recognizable. Initially, we suspected them to be helimagnetic spin wave excitations (helimagnons), which were described for pure MnSi in [82]. We concluded from the comparison of the values of Γ_0 for MnSi in tables 4.8 (second column) and 4.9 (second column) with the values for Mn$_{1-x}$Fe$_x$Si in table 4.10 (second column) that the spin wave stiffness in MnSi is about a factor of 3.8 larger than in Mn$_{1-x}$Fe$_x$Si. With the helical propagation vector in Mn$_{1-x}$Fe$_x$Si by about a factor of 2.2 larger than in MnSi, this would mean according to the calculations in [82] that the helimagnon modes in Mn$_{1-x}$Fe$_x$Si have about 20% higher energy than the corresponding modes in MnSi. According to [82], measurable helimagnon modes at the position of the nuclear peak in Mn$_{1-x}$Fe$_x$Si would have energies less than 0.1 meV, which cannot be resolved with the instrument resolution. Therefore, the inelastic features in figure 4.35 (a) and (b) at energies of about 2 meV cannot be the helimagnons described in [82]. Their origin remains thus unclear.

In table 4.13, the values for A_L and Γ as obtained in the fits in figure 4.35 (c), (d) and (e) are given. When comparing the values of the linewidth Γ in table 4.13 with the values in figure 4.31, we note that the linewidths obtained on TASP are over four times larger than data taken on PANDA at comparable values of q_{red} (the value of q_{red} on TASP was 0.078 Å^{-1}) even though the temperature on PANDA (20 K) was higher than 7 K and 12 K used in two of the measurements on TASP. Furthermore, the linewidth Γ in table 4.13 does not rise monotonically with increasing temperature in discrepancy to the theory represented by equations 4.3 to 4.5. The amplitude A_L decreases with increasing temperature in qualitative accordance to the theory. All these characteristics described above are not understood so far.
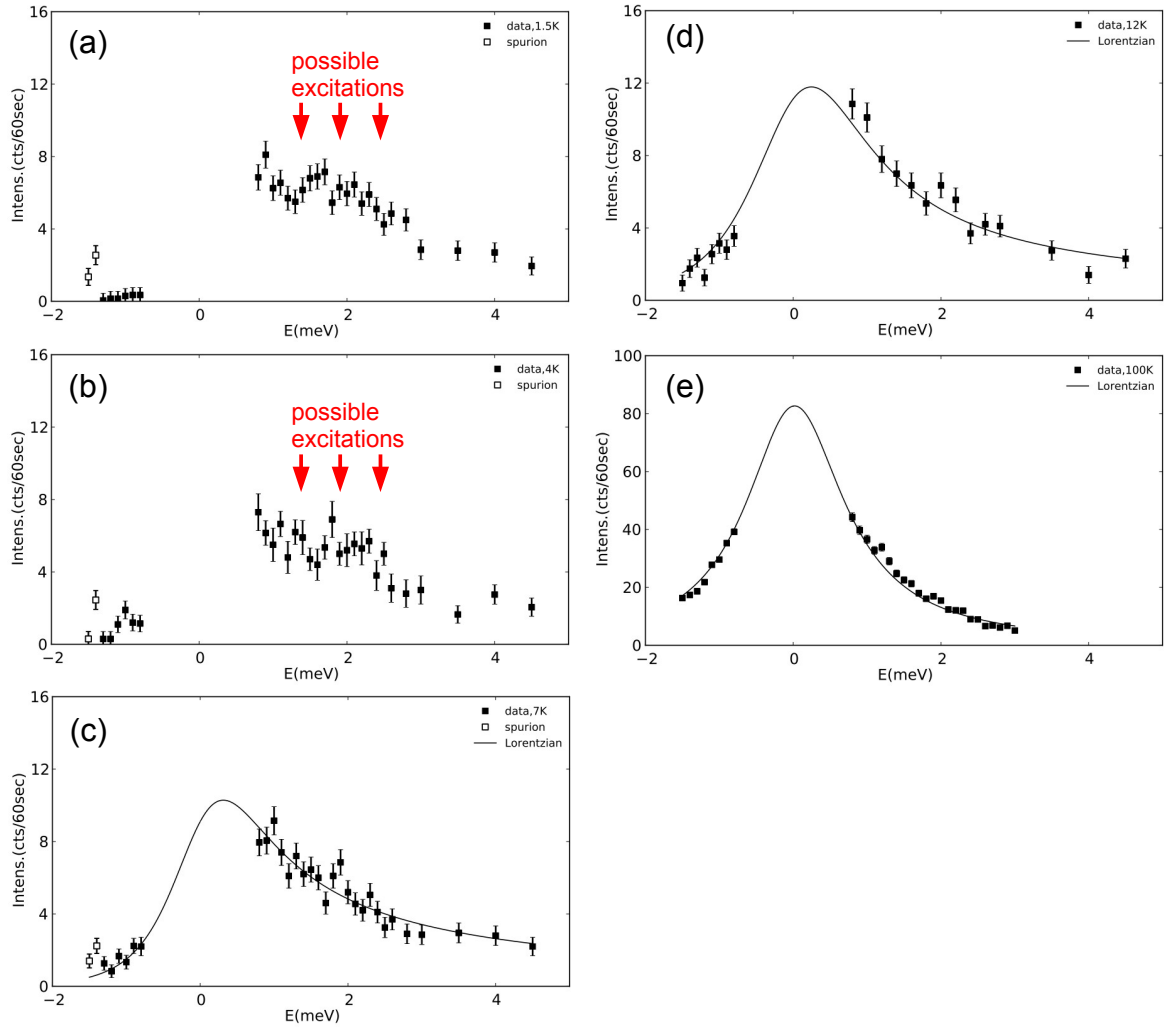
Figure 4.35: All data measured at the position of the nuclear (110) peak. Only the tails are shown. The peak center at zero energy (the actual Bragg peak) is omitted. Data at $T > T_c$ was fitted by equation 4.1. At $T < T_c$, possible excitations are indicated.

Table 4.13: Parameters obtained by fitting equation 4.1 to the data measured at $T > T_c$ in figure 4.35.

	A_L (a.u.)	Γ(meV)
7 K	2.526±0.112	0.854±0.069
12 K	2.110±0.079	1.000±0.082
100 K	1.527±0.021	0.812±0.026

Chapter 5

Concluding Remarks

In the first part of this thesis, we examined spin transfer torque effects in the helimagnetic material system MnSi. The influence of an unpolarized electric current on the helimagnetic structure was studied with neutron diffraction.

During these measurements, the A-phase in MnSi was identified as a skyrmion lattice, as we observed hexagonal scattering patterns [1]. It could be shown that this skyrmion phase is stabilized by thermal fluctuations [1]. The hexagonal alignment of the magnetic vortices, which composes the skyrmion lattice, is reminiscent of the vortices in type II superconductors (Shubnikov phase). Current-induced effects could be detected only in this skyrmion phase. At current flow through the sample and when simultaneously creating a vertical temperature gradient in the sample, a rotation of the hexagonal scattering patterns could be observed. The rotational sense is dependent on the direction of the current, the direction of the applied magnetic field, and the direction of the temperature gradient. We were able to explain this rotational behavior by a very efficient coupling of the spin current to the magnetic vortices and a varying magnetization within the sample, caused by the temperature gradient [4].

The current densities necessary to observe the rotations were 5 to 6 orders of magnitude smaller than the current densities typically applied in studies of spin transfer torque effects. This thesis contributes to the knowledge of spin transfer torques in non trivial topological structures and due to the small current densities required, it could make a contribution to the development of practical applications of the spin transfer torque effect. The next experimental challenge might be the direct observation of the current induced motion of the skyrmion lattice in real space.

In the second part of this thesis, spin fluctuations in the helimagnetic material systems MnSi and $Mn_{1-x}Fe_xSi$ were examined. As pointed out above, fluctuations can explain the stabilization of the skyrmion phase in MnSi [1]. As experimental method we used inelastic neutron scattering on a triple axis spectrometer. The quasi-elastic scattering was analyzed, which is a Lorentzian function in energy (centered at $E = 0$) convoluted with the instrument resolution.

Pure MnSi was examined at first because data on this material was already existent [5] [6] [7] [8] [9]. It had been possible to interpret this data in the framework of

the self-consistent renormalization theory developed by Moriya and Kawabata [5] [6]. With our measurements we wanted to confirm the previous experimental works, or rather demonstrate that our measurement method agrees with these works. We were able to confirm the consistence of our data with the previous measurements. However, we also detected discrepancies of the data to the theory, which treats the material as an isotropic itinerant ferromagnet. Therefore, a new theory is needed in order to account for the chiral interactions in the helimagnet MnSi.

Then, the spin fluctuations in $Mn_{1-x}Fe_xSi$ with a Fe concentration of $x = 0.12$ were examined in the same way. For this material, only few data existed prior to our experiments [9]. We observed a considerable temperature dependent vertical offset of the linewidth at $q_{red} = 0$, which we could only interpret as an unidentified damping mechanism. We state that also for $Mn_{1-x}Fe_xSi$ a new theory has to be developed in which the chiral interactions have to be taken into consideration.

Chapter 6

Acknowledgements

During my work at the E21-group, I received support and help from many people. Here, I want to thank all of them. Especially, I would like to mention the following persons:

- **Prof. Dr. Peter Böni**
  For the original idea of the experiments involving inelastic neutron scattering. He provided excellent general conditions for my work.

- **Prof. Dr. Christian Pfleiderer**
  For the initiative of doing the spin torque experiment and the excellent support and guidance during my work.

- **Dr. Sebastian Mühlbauer**
  During my diploma work, which I also did in this group, he was my inofficial tutor and introduced me to neutron scattering. He participated in a great part of the spin torque experiments and without him, his experience and his practical skills, this work would not have been possible.

- **Arbeitsgruppe Prof. Dr. Achim Rosch** (Institut für theoretische Physik der Universtät zu Köln)
  For providing the theoretical input for my work. I want to mention **Karin Everschor** in particular who did a great deal of the calculations for the interpretation of the spin torque experiments.

- **Dr. Robert Georgii** and **Reinhard Schwikowski**
  For their expertise and helpful assistance during the measurements at MIRA (FRM II).

- **Dr. Astrid Schneidewind, Dr. Enrico Faulhaber, Dirk Etzdorf** and **Dr. Peter Link**
  For granting me measurement time at PANDA and for the competent and cooperative work during those measurements.

- **Dr. Bertrand Roessli**
  For his advice during the measurements at TASP (PSI). The experiment was

greatly aided by his profound knowledge and experience in triple axis spectroscopy.

- **Prof. Dr. Ted Forgan** and his group
  Especially, I want to mention **Dr. Elizabeth Blackburn** and **Dr. Jonathan White**. We did small angle neutron scattering experiments together at the IN15 (ILL). I want to thank them for their cooperation during these experiments, which made my stay in Grenoble quite pleasant.

- **Dr. Wolfang Häußler**
  For his support during the measurements at RESEDA (FRM II).

- **Dr. Giovanna Simeoni** and **Dr. Tobias Unruh**
  For help with the measurements at TOFTOF (FRM II).

- **Dr. Thomas Keller**
  For enabling the measurements at TRISP (FRM II).

- **Dr. Sarah Dunsiger**
  For the advice she gave me concerning neutron scattering on multiple occasions, due to her knowledge and her experience.

- **Andreas Mantwill**
  For executing even last minute orders when some mechanical part had to be manufactured.

- **The central work shop of the department**
  Many of the mechanical parts of the experiments were made by them. The mechanics were always ready to give priority to manufacturing my parts when it was necessary in order to finish them at the desired date.

- **The crystal lab of the department**
  For the competent work in preparing samples and orienting them in the Laue-machine. This was indispensable for my work.

- **The FRM II Net Administrators**
  For keeping the Net intact and for the help I received when requiring it.

- My colleagues, PhD students, Master students and Postdocs **Dr. Andreas Neubauer, Andreas Bauer, Dr. Stefan Legl, Wolfgang Münzer, Alfonso Chacón, Dr. Marc Janoschek, Christian Franz, Alexander Regnat, Matthias Sandhofer, Dr. Saskia Gottlieb-Schönmeyer, Christopher Krey, Dr. Wolfgang Kreuzpaintner, Philipp Schmakat, Tim Adams, Dr. Michael Schulz, Robert Ritz, Tomek Schulz, Alexander Tischendorf, Michael Wagner, Georg Brandl, Ralf Korntner, Felicitas Birkelbach, Katharina Lochner, Stefan Giemsa, Marco Halder, Kilian Mittermüller, Max Hirschberger, Jonas Kindervater, Dorothea Mallinger, Birgit Wiedemann**.
  The atmosphere at the E21 group was very friendly and conducive to my work.

- **Barbara Russ**
  For the daily support in my practical work in the laboratory.

Chapter 7

List of Publications

1. T. Adams, S. Mühlbauer, C. Pfleiderer, F. Jonietz, A. Bauer, A. Neubauer, R. Georgii, P. Böni, U. Keiderling, K. Everschor, M. Garst, and A. Rosch. Long-Range Crystalline Nature of the Skyrmion Lattice in MnSi. *Phys. Rev. Lett.*, in press, 2011.

2. F. Jonietz, S. Mühlbauer, C. Pfleiderer, A. Neubauer, W. Münzer, A. Bauer, T. Adams, R. Georgii, P. Böni, R. A. Duine, K. Everschor, M. Garst, and A. Rosch. Spin Transfer Torques in MnSi at Ultralow Current Densities. *Science*, 330(6011):1648-1651, 2010.

3. W. Münzer, A. Neubauer, T. Adams, S. Mühlbauer, C. Franz, F. Jonietz, R. Georgii, P. Böni, B. Pedersen, M. Schmidt, A. Rosch, and C. Pfleiderer. Skyrmion lattice in the doped semiconductor $Fe_{1-x}Co_xSi$. *Phys. Rev. B*, 81(4):041203, 2010.

4. C. Pfleiderer, T. Adams, A. Bauer, W. Biberacher, B. Binz, F. Birkelbach, P. Böni, C. Franz, R. Georgii, M. Janoschek, F. Jonietz, T. Keller, R. Ritz, S. Mühlbauer, W. Münzer, A. Neubauer, B. Pedersen, and A. Rosch. Skyrmion lattices in metallic and semiconducting B20 transition metal compounds. *Journal of Physics: Condensed Matter*, 22(16):164207, 2010.

5. T. Adams, S. Mühlbauer, A. Neubauer, W. Münzer, F. Jonietz, R. Georgii, B. Pedersen, P. Böni, A. Rosch, and C. Pfleiderer. Skyrmion Lattice Domains in $Fe_{1-x}Co_xSi$. *Journal of Physics: Conference Series*, 200(3):032001, 2010.

6. M. Janoschek, F. Jonietz, P. Link, C. Pfleiderer, and P. Böni. Helimagnons in the Skyrmion Lattice of MnSi. *Journal of Physics: Conference Series*, 200(3):032026, 2010.

7. S. Mühlbauer, B. Binz, F. Jonietz, C. Pfleiderer, A. Rosch, A. Neubauer, R. Georgii, and P. Böni. Skyrmion Lattice in a Chiral Magnet. *Science*, 323(5916):915-919, 2009.

8. C. Pfleiderer, A. Neubauer, S. Mühlbauer, F. Jonietz, M. Janoschek, S. Legl, R. Ritz, W. Münzer, C. Franz, P. G. Niklowitz, T. Keller, R. Georgii, P. Böni, B. Binz, A. Rosch, U. K. Rößler, and A. N. Bogdanov. Quantum order in the chiral magnet MnSi. *Journal of Physics: Condensed Matter*, 21(16):164215, 2009.

Bibliography

[1] S. Mühlbauer, B. Binz, F. Jonietz, C. Pfleiderer, A. Rosch, A. Neubauer, R. Georgii, and P. Böni. Skyrmion Lattice in a Chiral Magnet. *Science*, 323(5916):915–919, 2009.

[2] A. N. Bogdanov and D. A. Yablonskii. *Sov. Phys. JETP*, 68:101, 1989.

[3] U. K. Rößler, A. N. Bogdanov, and C. Pfleiderer. Spontaneous skyrmion ground states in magnetic metals. *Nature*, 442:797–801, 2006.

[4] F. Jonietz, S. Mühlbauer, C. Pfleiderer, A. Neubauer, W. Münzer, A. Bauer, T. Adams, R. Georgii, P. Böni, R. A. Duine, K. Everschor, M. Garst, and A. Rosch. Spin Transfer Torques in MnSi at Ultralow Current Densities. *Science*, 330(6011):1648–1651, 2010.

[5] Y. Ishikawa, Y. Noda, C. Fincher, and G. Shirane. Low-energy paramagnetic spin fluctuations in the weak itinerant ferromagnet MnSi. *Phys. Rev. B*, 25(1):254–263, 1982.

[6] Y. Ishikawa, Y. Noda, Y. J. Uemura, C. F. Majkrzak, and G. Shirane. Paramagnetic spin fluctuations in the weak itinerant-electron ferromagnet MnSi. *Phys. Rev. B*, 31(9):5884–5893, 1985.

[7] C. Pappas, E. Lelièvre-Berna, P. Bentley, P. Falus, P. Fouquet, and B. Farago. Magnetic Fluctuations and Correlations in MnSi - Evidence for a Skyrmion Spin Liquid Phase. arXiv:1103.0574v1, 2011.

[8] S. V. Grigoriev, S. V. Maleyev, E. V. Moskvin, V. A. Dyadkin, P. Fouquet, and H. Eckerlebe. Crossover behavior of critical helix fluctuations in MnSi. *Phys. Rev. B*, 81(14):144413, 2010.

[9] A. Tischendorf. Spin echo measurements of magnetic fluctuations in helical $Mn_{1-x}Fe_xSi$, Diplomarbeit TUM, November 2010.

[10] H. J. Williams, J. H. Wernick, R. C. Sherwood, and G. K. Wertheim. Magnetic Properties of the Monosilicides of Some 3d Transition Elements. *Journal of Applied Physics*, 37(3):1256, 1966.

[11] D. Bloch, J. Voiron, V. Jaccarino, and J. H. Wernick. The high field-high pressure magnetic properties of MnSi. *Physics Letters A*, 51(5):259–261, 1975.

[12] C. Pfleiderer, D. Reznik, L. Pintschovius, and J. Haug. Magnetic Field and Pressure Dependence of Small Angle Neutron Scattering in MnSi. *Phys. Rev. Lett.*, 99(15):156406, 2007.

[13] C. Pfleiderer, P. Böni, T. Keller, U. Rößler, and A. Rosch. Non Fermi Liquid Metal Without Quantum Criticality. *Science*, 316:1871–1874, 2007.

[14] C. Thessieu, C. Pfleiderer, A. N. Stepanov, and J. Flouquet. Field dependence of the magnetic quantum phase transition in MnSi. *Journal of Physics: Condensed Matter*, 9(31):6677, 1997.

[15] T. Moriya. Spin Fluctuations in Itinerant Electron Magnetism. *Springer, Berlin*, 1985.

[16] E. Stoner. Collective Electron Ferromagnetism. *Proceeding of the Royal Society of London, Series A, Mathematical and Physical Sciences*, 165(922):372–414, 1938.

[17] S. Blundell. Magnetism in Condensed Matter. *Oxford University Press Inc., New York*, 2001.

[18] G. G. Lonzarich and L. Taillefer. Effect of spin fluctuations on the magnetic equation of state of ferromagnetic or nearly ferromagnetic metals. *Journal of Physics C: Solid State Physics*, 18(22):4339, 1985.

[19] I. Dzyaloshinsky. A thermodynamic theory of weak ferromagnetism of antiferromagnets. *Journal of Physics and Chemistry of Solids*, 4(4):241–255, 1958.

[20] T. Moriya. Anisotropic Superexchange Interaction and Weak Ferromagnetism. *Phys. Rev.*, 120(1):91–98, 1960.

[21] P. Bak and M. H. Jensen. Theory of helical magnetic structures and phase transitions in MnSi and FeGe. *Journal of Physics C: Solid State Physics*, 13(31):L881, 1980.

[22] M. L. Plumer and M. B. Walker. Wavevector and spin reorientation in MnSi. *Journal of Physics C: Solid State Physics*, 14(31):4689, 1981.

[23] Y. Ishikawa, K. Tajima, D. Bloch, and M. Roth. Helical spin structure in manganese silicide MnSi. *Solid State Communications*, 19(6):525–528, 1976.

[24] O. Nakanishi, A. Yanase, A. Hasegawa, and M. Kataoka. The origin of the helical spin density wave in MnSi. *Solid State Communications*, 35(12):995–998, 1980.

[25] P. A. Hansen. Magnetic Anisotropy and Related Matters Studied by Neutron Diffraction. *Riso Report No.360 (thesis), Riso National Laboratory, Gjellerup, Copenhagen*, page 69, 1977.

[26] Y. Ishikawa, G. Shirane, J. A. Tarvin, and M. Kohgi. Magnetic excitations in the weak itinerant ferromagnet MnSi. *Phys. Rev. B*, 16(11):4956–4970, 1977.

[27] S. V. Grigoriev, S. V. Maleyev, A. I. Okorokov, Yu. O. Chetverikov, P. Böni, R. Georgii, D. Lamago, H. Eckerlebe, and K. Pranzas. Magnetic structure of MnSi under an applied field probed by polarized small-angle neutron scattering. *Phys. Rev. B*, 74(21):214414, 2006.

[28] Y. Ishikawa and M. Arai. Magnetic Phase Diagram of MnSi near Critical Temperature Studied by Neutron Small Angle Scattering. *J. Phys. Soc. Jpn.*, 53:2726–2733, 1984.

[29] P. Harris, B. Lebech, Hae Seop Shim, K. Mortensen, and J. Skov Pedersen. Small-angle neutron-scattering studies of the magnetic phase diagram of MnSi. *Physica B: Condensed Matter*, 213-214:375–377, 1995.

[30] S. V. Grigoriev, S. V. Maleyev, A. I. Okorokov, Yu. O. Chetverikov, and H. Eckerlebe. Field-induced reorientation of the spin helix in MnSi near T_c. *Phys. Rev. B*, 73(22):224440, 2006.

[31] C. Pfleiderer. Experimental studies of weakly magnetic transition metal compounds. *Journal of Magnetism and Magnetic Materials*, 226-230(Part 1):23–29, 2001.

[32] S. M. Stishov, A. E. Petrova, S. Khasanov, G. K. Panova, A. A. Shikov, J. C. Lashley, D. Wu, and T. A. Lograsso. Heat capacity and thermal expansion of the itinerant helimagnet MnSi. *Journal of Physics: Condensed Matter*, 20(23):235222, 2008.

[33] S. V. Grigoriev, S. V. Maleyev, A. I. Okorokov, Yu. O. Chetverikov, R. Georgii, P. Böni, D. Lamago, H. Eckerlebe, and K. Pranzas. Critical fluctuations in MnSi near T_C: A polarized neutron scattering study. *Phys. Rev. B*, 72(13):134420, 2005.

[34] R. Georgii, P. Böni, D. Lamago, S. Stüber, S. V. Grigoriev, S. V. Maleyev, A. I. Okorokov, H. Eckerlebe, P. K. Pranzas, B. Roessli, and W. E. Fischer. Critical small-angle scattering of polarised neutrons in MnSi. *Physica B: Condensed Matter*, 350(1-3):45–47, 2004.

[35] D. Lamago. Critical Magnetic Fluctuations in Localized and Itinerant Magnets studied by Neutron Scattering, PhD thesis TUM. 2006.

[36] M. Janoschek. Investigation of the chiral magnets $NdFe_3(^{11}BO_3)_4$ and MnSi by means of neutron scattering, PhD thesis TUM. 2008.

[37] C. Pappas, E. Lelièvre-Berna, P. Falus, P. M. Bentley, E. Moskvin, S. Grigoriev, P. Fouquet, and B. Farago. Chiral Paramagnetic Skyrmion-like Phase in MnSi. *Phys. Rev. Lett.*, 102(19):197202, 2009.

[38] T. Adams. Skyrmionengitter und partielle Ordnung in B20 Übergangsmetallverbindungen, Diplomarbeit TUM, 2009.

[39] A. E. Petrova, V. N. Krasnorussky, T. A. Lograsso, and S. M. Stishov. High-pressure study of the magnetic phase transition in MnSi. *Phys. Rev. B*, 79(10):100401, 2009.

[40] C. Pfleiderer, S. R. Julian, and G. G. Lonzarich. Non-Fermi-liquid nature of the normal state of itinerant-electron ferromagnets. *Nature*, 414:427–430, 2001.

[41] C. Pfleiderer, D. Reznik, L. Pintschovius, H. v. Löhneysen, M. Garst, and A. Rosch. Partial order in the non-Fermi-liquid phase of MnSi. *Nature*, 427:227–231, 2004.

[42] B. Binz, A. Vishwanath, and V. Aji. Theory of the Helical Spin Crystal: A Candidate for the Partially Ordered State of MnSi. *Phys. Rev. Lett.*, 96(20):207202, 2006.

[43] I. Fischer, N. Shah, and A. Rosch. Crystalline phases in chiral ferromagnets: Destabilization of helical order. *Phys. Rev. B*, 77(2):024415, 2008.

[44] S. Tewari, D. Belitz, and T. R. Kirkpatrick. Blue Quantum Fog: Chiral Condensation in Quantum Helimagnets. *Phys. Rev. Lett.*, 96(4):047207, 2006.

[45] N. Manyala, Y. Sidis, J. F. DiTusa, G. Aeppli, D. P. Young, and Z. Fisk. Magnetoresistance from quantum interference effects in ferromagnets. *Nature*, 404(6778):581–584, 2000.

[46] N. Manyala, Y. Sidis, J. F. DiTusa, G. Aeppli, D. P. Young, and Z. Fisk. Large anomalous Hall effect in a silicon-based magnetic semiconductor. *Nature Materials*, 3(4):255–262, 2004.

[47] A. Bauer. Quantenphasenübergänge und Skyrmion Gitter in $Mn_{1-x}Fe_xSi$ und $Mn_{1-x}Co_xSi$, Diplomarbeit TUM, 2009.

[48] G. Prinz. Magnetoelectronics. *Science*, 282(5394):1660–1663, 1998.

[49] J. Gregg, W. Allen, N. Viart, R. Kirschman, C. Sirisathitkul, J. Schille, M. Gester, S. Thompson, P. Sparks, V. Da Costa, K. Ounadjela, and M. Skvarla. The art of spin electronics. *Journal of Magnetism and Magnetic Materials*, 175(1-2):1–9, 1997.

[50] P. Ball. Meet the spin doctors. *Nature*, 404:918–920, 2000.

[51] M. N. Baibich, J. M. Broto, A. Fert, F. Nguyen Van Dau, F. Petroff, P. Etienne, G. Creuzet, A. Friederich, and J. Chazelas. Giant Magnetoresistance of (001)Fe/(001)Cr Magnetic Superlattices. *Phys. Rev. Lett.*, 61(21):2472–2475, 1988.

[52] G. Binasch, P. Grünberg, F. Saurenbach, and W. Zinn. Enhanced magnetoresistance in layered magnetic structures with antiferromagnetic interlayer exchange. *Phys.Rev.B*, 39(7):4828–4830, 1989.

[53] J. S. Moodera, Lisa R. Kinder, Terrilyn M. Wong, and R. Meservey. Large Magnetoresistance at Room Temperature in Ferromagnetic Thin Film Tunnel Junctions. *Phys. Rev. Lett.*, 74(16):3273–3276, 1995.

[54] T.R. McGuire and R.I. Potter. Anisotropic Magnetoresistance in Ferromagnetic 3d Alloys. *IEEE Transactions on magnetics*, Mag-11(4), 1975.

[55] Jiang Xiao, A. Zangwill, and M. D. Stiles. Spin-transfer torque for continuously variable magnetization. *Phys. Rev. B*, 73(5):054428, 2006.

[56] A. Fert, J. George, R. Mattana, P. Seneor, and H. Jaffres. The new era of spintronics. *Europhysics News*, 34:227–229, 2003.

[57] J. Slonczewski. Current-driven excitation of magnetic multilayers. *Journal of Magnetism and Magnetic Materials*, 159(1-2):L1–L7, 1996.

[58] L. Berger. Emission of spin waves by a magnetic multilayer traversed by a current. *Phys. Rev. B*, 54(13):9353–9358, 1996.

[59] T. Silva. Spintronics: Field-free ringing of nanomagnets. *Nature Physics*, 3:447–448, 2007.

[60] S. I. Kiselev, J. C. Sankey, I. N. Krovorotov, N. C. Emley, R. J. Schoelkopf, R. A. Buhrman, and D. C. Ralph. Microwave oscillations of a nanomagnet driven by a spin-polarized current. *Nature*, 425:380–383, 2003.

[61] V. S. Pribiag, I. N. Krivorotov, G. D. Fuchs, P. M. Braganca, O. Ozatay, J. C. Sankey, D. C. Ralph, and R. A. Buhrman. Magnetic vortex oscillator driven by d.c. spin-polarized current. *Nature Physics*, 3:498–503, 2007.

[62] O. Boulle, V. Cros, J. Grollier, L. G. Pereira, C. Deranlot, F. Petroff, G. Faini, J. Barna, and A. Fert. Shaped angular dependence of the spin-transfer torque and microwave generation without magnetic field. *Nature Physics*, 3:492–497, 2007.

[63] F. B. Mancoff, N. D. Rizzo, B. N. Engel, and S. Tehrani. Phase-locking in double-point-contact spin-transfer devices. *Nature*, 437:393–395, 2005.

[64] I. N. Krivorotov, N. C. Emley, J. C. Sankey, S. I. Kiselev, D. C. Ralph, and R. A. Buhrman. Time-Domain Measurements of Nanomagnet Dynamics Driven by Spin-Transfer Torques. *Science*, 307(5707):228–231, 2005.

[65] H. Kubota, A. Fukushima, K. Yakushiji, T. Nagahama, S. Yuasa, K. Ando, H. Maehara, Y. Nagamine, K. Tsunekawa, D. D. Djayaprawira, N. Watanabe, and Y. Suzuki. Quantitative measurements of voltage dependence of spin-transfer torque in MgO-based magnetic tunnel junctions. *Nature Physics*, 4:37–41, 2008.

[66] M. Tsoi, A. G. M. Jansen, J. Bass, W.-C. Chiang, M. Seck, V. Tsoi, and P. Wyder. Excitation of a Magnetic Multilayer by an Electric Current. *Phys. Rev. Lett.*, 80(19):4281–4284, 1998.

[67] E. B. Myers, D. C. Ralph, J. A. Katine, R. N. Louie, and R. A. Buhrman. Current-Induced Switching of Domains in Magnetic Multilayer Devices. *Science*, 285(5429):867–870, 1999.

[68] A. A. Tulapurkar, Y. Suzuki, A. Fukushima, H. Kubota, H. Maehara, K. Tsunekawa, D. D. Djayaprawira, N. Watanabe, and S. Yuasa. Spin-torque diode effect in magnetic tunnel junctions. *Nature*, 438:339–342, 2005.

[69] M. Yamanouchi, D. Chiba, F. Matsukura, and H. Ohno. Current-induced domain-wall switching in a ferromagnetic semiconductor structure. *Nature*, 428:539–542, 2004.

[70] M. Yamanouchi, D. Chiba, F. Matsukura, T. Dietl, and H. Ohno. Velocity of Domain-Wall Motion Induced by Electrical Current in the Ferromagnetic Semiconductor (Ga,Mn)As. *PRL*, 96(9):096601, 2006.

[71] J. Grollier, P. Boulenc, V. Cros, A. Hamzic, A. Vaures, A. Fert, and G. Faini. Switching a spin valve back and forth by current-induced domain wall motion . *Applied Physics Letters*, 83(3):509, 2003.

[72] M. Tsoi, R. Fontana, and S. Parkin. Magnetic domain wall motion triggered by an electric current . *Applied Physics Letters*, 83(13):2617–2619, 2003.

[73] M. Kläui, C. A. F. Vaz, J. A. C. Bland, W. Wernsdorfer, G. Faini, E. Cambril, L. J. Heyderman, F. Nolting, and U. Rüdiger. Controlled and Reproducible Domain Wall Displacement by Current Pulses Injected into Ferromagnetic Ring Structures. *Phys. Rev. Lett.*, 94(10):106601, 2005.

[74] R. Duine and A. Rosch. Notes on Spin Transfer Torques in Helimagnets. *unpublished*.

[75] F. Jonietz. Experimentelle Untersuchung von Spin-Torque-Effekten in Helimagneten, Diplomarbeit TUM, March 2008.

[76] S. Tixier, P. Böni, Y. Endoh, B. Roessli, and G. Shirane. Polarisation dependence of the magnetic fluctuations in the weak itinerant ferromagnet MnSi below T_C. *Physica B: Condensed Matter*, 241-243:613–615, 1997.

[77] F. Semadeni, P. Böni, Y. Endoh, B. Roessli, and G. Shirane. Direct observation of spin-flip excitations in MnSi. *Physica B: Condensed Matter*, 267-268:248–251, 1999.

[78] G. Shirane, R. Cowley, C. Majkrzak, J. B. Sokoloff, B. Pagonis, C. H. Perry, and Y. Ishikawa. Spiral magnetic correlation in cubic MnSi. *Phys. Rev. B*, 28(11):6251–6255, 1983.

[79] B. Roessli, P. Böni, W. E. Fischer, and Y. Endoh. Chiral Fluctuations in MnSi above the Curie Temperature. *Phys. Rev. Lett.*, 88(23):237204, 2002.

[80] D. Belitz, T. R. Kirkpatrick, and A. Rosch. Theory of helimagnons in itinerant quantum systems. *Phys. Rev. B*, 73(5):054431, 2006.

[81] S. V. Maleyev. Cubic magnets with Dzyaloshinskii-Moriya interaction at low temperature. *Phys. Rev. B*, 73(17):174402, 2006.

[82] M. Janoschek, F. Bernlochner, S. Dunsiger, C. Pfleiderer, P. Böni, B. Roessli, P. Link, and A. Rosch. Helimagnon bands as universal excitations of chiral magnets. *Phys. Rev. B*, 81(21):214436, 2010.

[83] G. G. Lonzarich. The Magnetic Electron. *University of Cambridge*, 1997.

[84] G.L. Squires. Introduction to the theory of thermal neutron scattering. *Dover Publications*, 1978.

[85] S.W. Lovesey. Theory of Neutron Scattering from Condensed Matter Vol I/II. *Oxford Science Publications*, 1984.

[86] G.Shirane, S. Shapiro, and J. Tranquada. Neutron Scattering with a Triple-Axis Spectrometer - Basic Techniques. *Cambridge University Press*, 2002.

[87] S. Mühlbauer. Das Flussgitter in Niob - Messungen mit polarisierten und unpolarisierten Neutronen, Diplomarbeit TUM, May 2005.

[88] M. Janoschek. MuPAD 3D Polarization Analysis in Magnetic Neutron Scattering, Diplomarbeit TUM, September 2004.

[89] S. Mühlbauer. Vortex Lattices in Superconducting Niobium and Skyrmion Lattices in the Chiral Magnet MnSi Investigated by Neutron Scattering, PhD thesis TUM. 2009.

[90] http://www.frm2.tum.de/wissenschaft/diffraktometer/mira/index.html.

[91] M. Janoschek, P. Böni, and M. Braden. Optimization of elliptic neutron guides for triple-axis spectroscopy. *Nuclear Instruments and Methods in Physics Research, Section A*, 613(1):119–126, 2010.

[92] M. J. Cooper and R. Nathans. The resolution function in neutron diffractometry. I. The resolution function of a neutron diffractometer and its application to phonon measurements. *Acta Crystallographica*, 23(3):357–367, 1967.

[93] N. J. Chesser and J. D. Axe. Derivation and experimental verification of the normalized resolution function for inelastic neutron scattering. *Acta Crystallographica Section A*, 29(2):160–169, 1973.

[94] J. M. Tranquada G. Shirane, S. M. Shapiro. Neutron Scattering with a Triple-Axis Spectrometer. *Cambridge University Press*, 2002.

[95] T. Adams, S. Mühlbauer, C. Pfleiderer, F. Jonietz, A. Bauer, A. Neubauer, R. Georgii, P. Böni, U. Keiderling, K. Everschor, M. Garst, and A. Rosch. Long-range crystalline nature of the skyrmion lattice in MnSi. arXiv:1107.0993v1, 2011.

[96] C. Pfleiderer, T. Adams, A. Bauer, W. Biberacher, B. Binz, F. Birkelbach, P. Böni, C. Franz, R. Georgii, M. Janoschek, F. Jonietz, T. Keller, R. Ritz, S. Mühlbauer, W. Münzer, A. Neubauer, B. Pedersen, and A. Rosch. Skyrmion lattices in metallic and semiconducting B20 transition metal compounds. *Journal of Physics: Condensed Matter*, 22(16):164207, 2010.

[97] A. A. Thiele. Steady-State Motion of Magnetic Domains. *Phys. Rev. Lett.*, 30(6):230–233, 1973.

[98] A. Neubauer, C. Pfleiderer, B. Binz, A. Rosch, R. Ritz, P. G. Niklowitz, and P. Böni. Topological Hall Effect in the *A* Phase of MnSi. *Phys. Rev. Lett.*, 102(18):186602, 2009.

[99] C. Pfleiderer and A. Rosch. Condensed-matter physics: Single skyrmions spotted. *Nature*, 465:880–881, 2010.

[100] W. Münzer, A. Neubauer, T. Adams, S. Mühlbauer, C. Franz, F. Jonietz, R. Georgii, P. Böni, B. Pedersen, M. Schmidt, A. Rosch, and C. Pfleiderer. Skyrmion lattice in the doped semiconductor $Fe_{1-x}Co_xSi$. *Phys. Rev. B*, 81(4):041203, 2010.

[101] X. Z. Yu, Y. Onose, N. Kanazawa, J. H. Park, J. H. Han, Y. Matsui, N. Nagaosa, and Y. Tokura. Real-space observation of a two-dimensional skyrmion crystal. *Nature*, 465:901–904, 2010.

[102] C. Schieback, D. Hinzke, M. Kläui, U. Nowak, and P. Nielaba. Temperature dependence of the current-induced domain wall motion from a modified Landau-Lifshitz-Bloch equation. *Phys. Rev. B*, 80(21):214403, 2009.

[103] J. He, Z. Li, and S. Zhang. Current-driven vortex domain wall dynamics by micromagnetic simulations. *Phys. Rev. B*, 73(18):184408, 2006.

[104] J. Ye, Y. B. Kim, A. J. Millis, B. I. Shraiman, P. Majumdar, and Z. Tesanovic. Berry Phase Theory of the Anomalous Hall Effect: Application to Colossal Magnetoresistance Manganites. *Phys. Rev. Lett.*, 83(18):3737–3740, 1999.

[105] G. Tatara, H. Kohno, J. Shibata, Y. Lemaho, and K.-J. Lee. Spin Torque and Force due to Current for General Spin Textures. *Journal of the Physical Society of Japan*, 76(5):054707, 2007.

[106] B. Binz and A. Vishwanath. Chirality induced anomalous-Hall effect in helical spin crystals. *Physica B: Condensed Matter*, 403(5-9):1336–1340, 2008.

[107] M. Lee, W. Kang, Y. Onose, Y. Tokura, and N. P. Ong. Unusual Hall Effect Anomaly in MnSi under Pressure. *Phys. Rev. Lett.*, 102(18):186601, 2009.

[108] G. Blatter, M. V. Feigelman, V. B. Geshkenbein, A. I. Larkin, and V. M. Vinokur. Vortices in high-temperature superconductors. *Rev. Mod. Phys.*, 66(4):1125–1388, 1994.

[109] A. Bauer, A. Neubauer, C. Franz, W. Münzer, M. Garst, and C. Pfleiderer. Quantum phase transitions in single-crystal $Mn_{1-x}Fe_xSi$ and $Mn_{1-x}Co_xSi$: Crystal growth, magnetization, ac susceptibility, and specific heat. *Phys. Rev. B*, 82(6):064404, 2010.

[110] Daniel López, W. K. Kwok, H. Safar, R. J. Olsson, A. M. Petrean, L. Paulius, and G. W. Crabtree. Spatially Resolved Dynamic Correlation in the Vortex State of High Temperature Superconductors. *Phys. Rev. Lett.*, 82(6):1277–1280, 1999.

[111] M. Bode, M. Heide, K. von Bergmann, P. Ferriani, S. Heinze, G. Bihlmayer, A. Kubetzka, O. Pietzsch, S. Blügel, and R. Wiesendanger. Chiral magnetic order at surfaces driven by inversion asymmetry. *Nature*, 447:190–193, 2007.

[112] http://www.neutron.ethz.ch/research/resources/reslib.

[113] P. Böni, J. L. Martínez, and J. M. Tranquada. Longitudinal spin fluctuations in nickel. *Phys. Rev. B*, 43(1):575–584, 1991.

[114] Private communication with Dr. Bertrand Roessli, PSI.